Development of Electroassisted Catalysis Based on Surface Protonics and Alloying

（表面プロトニクスと合金化を駆使した電場触媒反応系の開拓）

ZHANG JIANSHUO

Graduate School of Chemical Sciences and Engineering

Hokkaido University

2023

Contents

Chapter 1

General Introduction

1. General Introduction

1.1 Electro-assisted reactions based on surface protonics mechanism

Modern chemical industry for fuel-refining and chemical production is the bedrock of our modern society. Most catalytic reactions are operated at high temperatures.[1] According to the Arrhenius kinetic low, i.e., $\ln k = \ln A - E_a/RT$, the temperature determined the kinetic constant k if the pre-exponential (frequency) factor A and the apparent activation energy E_a are fixed. For some endothermic reactions such as propane dehydrogenation (PDH), oxidative coupling of methane (OCM), dry reforming (DR), a higher reaction temperature is necessary to gain an appropriate yield due to the limitation of thermodynamics limitation. For example, PDH reaction is a promising technology for producing propylene, which is one of the most important feedstocks to produce plastic products.[2-4] However, owing to its highly endothermic properties, a temperature range of 550°C to 600°C is required to gain sufficient equilibrium yield.[2-4] Therefore, lots of energy is consumed in the required high-temperature system, which requires a high cost for operation. Moreover, under such high temperatures, side reactions and deactivation by coking and metal sintering occur, severely hindering practical utilization.[3-5] Therefore, developing a catalytic system for PDH and other reactions requiring high temperature that works at a lower temperature region is highly attractive.

Using an external-force system, such as photocatalysis, nonthermal plasma (NTP)-assisted catalysis, electrocatalysis, or electroassisted catalysis is a possible and pioneering approach. Among them, photocatalysis and electrocatalysis are promising methods for lowing reaction temperatures and energy saving. Normally, electrons are generated by adsorbed light or external electric field, and able to react with reactants molecules. They are limited by the low reaction rate and production capacity. For NTP-assisted catalysis, NTP can activate stable reactant molecules (e.g., CO_2, CH_4, and N_2) and consequently overcome the thermodynamic limitation or formation of new reaction pathways that cannot be achieved with thermal catalysis.[6] Electroassisted catalysis is also one of the promising approaches for such low-temperature conversion.[7] A direct current of several milliamperes is applied to the catalyst bed with two electrodes: a high-voltage and ground electrode, as shown in Figure 1.1.[1] Compared with the above options, electroassisted catalysis based on surface protonics is a promising methodology

for combining the advantages of thermal catalysis and electrocatalysis.

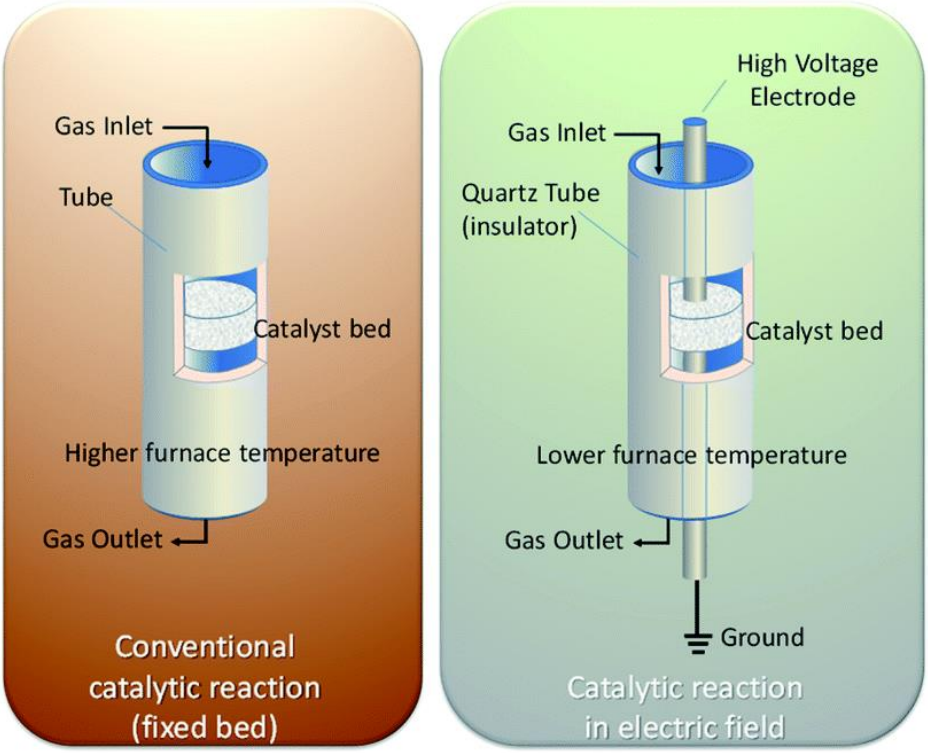

Figure 1.1. Schematic images of a conventional heterogeneous catalytic reaction system (left) and electroassisted catalysis system (right)[1]

In recent years, it had been found that various catalytic reactions can occur in low-temperature with an electric field. Various metal-supported catalysts, including Pd, Pt, Ru, Ni, and Co, supported on a semiconductor support (CeO_2, perovskite, TiO_2, etc.) are useful for these systems.[1] As shown in Table 1.1, conversion of robust reactant molecules is drastically increased by impressing a static electric field even at low external temperature.

Table 1.1. Conversions in various reactions under electric field compared with that under thermal conditions.

Reactions	Catalysts	External temp./°C	Power / W	Conversion / %		Ref.
				E.F.	Thermal	
OCM[a]	(1/200–Sr)-La_2O_3	150	2.7	11.5 (CH_4)	7.4 (@1000°C)	[8]
CO_2–OCM[b]	10 mol%La–ZrO_2	150	3.6	3.0 (CH_4)	0.2 (@800°C)	[9]
SRM[c]	1.0 wt% Pd/CeO_2	150	1.05	7 (CH_4)	≈ 0 (@150°C)	[7]
OCM[a]	$Ce_2(WO_4)_3$/CeO_2	150	2.7	13.6 (CH_4)	0 (@300°C)	[10]
CO_2–OCM[b]	$La_{0.7}Ca_{0.3}AlO_{3-\delta}$	150	7.5	10.4 (CH_4)	0.2 (@800°C)	[11]
DRM[c]	1 wt%Ni/10 mol%La–ZrO_2	150	3.7	22.8 (CH_4)	≈ 0	[12]
SRDME[d]	1.0 wt%Pd/CeO_2	200	0.53	9.9 (DME)	≈ 0	[13]
MCH dehydrogenation[e]	3 wt% Pt/CeO_2	150	0.7	21.6 (MCH)	5.5	[14]

[a]OCM: oxidative coupling of methane; [b]CO_2–OCM: oxidative coupling of methane using carbon dioxide; [c]SRM: steam reforming of methane; [c]DRM: dry reforming of methane; [d]SRDME: steam reforming of dimethyl ether; [e]MCH dehydrogenation: methylcyclohexane dehydrogenation

It was revealed that a steam reforming process showed high activity even at a low temperature of 423 K in an electric field by Sekine's group.[7] Especially, the kinetic analyses demonstrated the synergetic effect between the catalytic reaction and electric field, revealing strengthened water pressure dependence of the reaction rate when applying an electric field. Results of operando-DRIFTS revealed that proton conduction via adsorbed water on the catalyst surface occurred with an electric field, known as Grotthuss mechanism. Furthermore, proton collision occurred at the metal-support interface by hopping proton, resulting in methane activation at a low temperature, which never occurs without electric field.

Generally speaking, the surface protonics phenomenon is divided into two parts, as shown in Scheme 1.1: one is proton hopping on the oxide surface via the Grotthuss mechanism, and the other one is proton collision with the reactant molecules at the metal-support interface. The

Grotthuss mechanism was suggested by Noam Agmon for describing proton mobility on a solid surface.[15] Proton migration was envisioned as a process propelled by hydrogen-bond cleavage, occurring in front of the moving proton, and hydrogen-bond formation in its back. Moreover, the rotation adsorbed water was observed only when the electric field was applied to Pd/CeO_2 at 473 K, showing a strong relation with the Grotthuss mechanism.[7] For proton collision process, it has been reported that NH_4^+ was produced from synthesized NH_3 and proton when the electric field was applied.[16, 17] In the case of steam reforming of methane reaction, a three-atom transition state (i.e., C–H–H) was formed from surface proton colliding with methane.[18, 19] Similarly, the activation of reactant molecules by proton collision was also observed in various reactions, such as methylcyclohexane dehydrogenation,[14] dry reforming of methane,[20, 21] and methane coupling reaction.[22]

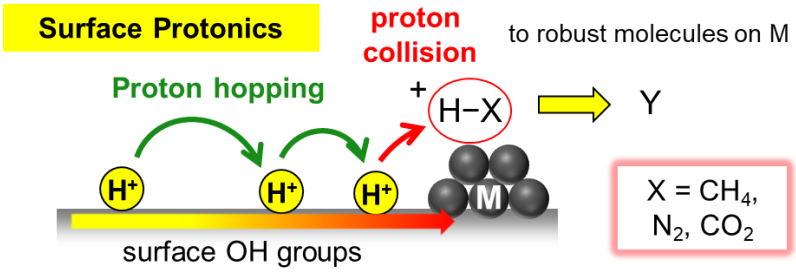

Scheme 1.1. Two parts of the surface protonics phenomenon.

In this reaction system, the overall reaction rate is determined mainly by the following three factors: (a) the number (concentration) of surface protons, (b) the stability of the transition state at proton collision, and (c) the selectivity of product molecules desorption or decomposition. Furthermore, the choices of support material also impact the reactivity. For instance, various semiconductors are selected as support due to the proper resistance that allows electricity to flow and generate a certain range of electric power.

To conclude, the electroassisted reactions are receiving more and more attention and have promising applications in low-temperature conversions.

1.2 Alloy in heterogeneous catalytic reactions

Metallic materials act as effective catalysts for various heterogeneous catalytic reactions and have been widely used in the chemical industry. However, drawbacks such as low selectivity and stability, high cost due to low dispersion restrict the utilization of pure active metal catalysts. Therefore, addition of various metal elements to form alloy has been used as a promising methodology to improve the catalytic performance of metallic materials.

Although there are some restrictions in catalytic chemistry, many alloy catalysts can be prepared by choosing several metallic elements from the periodic table. In terms of their structure, a variety of alloys can be divided into two categories: solid-solution alloys and intermetallic compounds, as shown in Figure 1.2.[23] The former, typically substitutional solid-solution alloys, consist of metals of similar atomic size and electronic character with a crystal structure identical to that of the parent metal with random atomic arrangement (Figure 1.2a). And if the atoms of one element are sufficiently small to fit within the lattice void of the counterpart element, interstitial solid-solution alloys can be formed (Figure 1.2b). Conversely, intermetallic compounds are formed when the component metals have significantly different characteristics and comprise distinct crystal structures with highly ordered atomic arrangements (Figure 1.2c).[24]

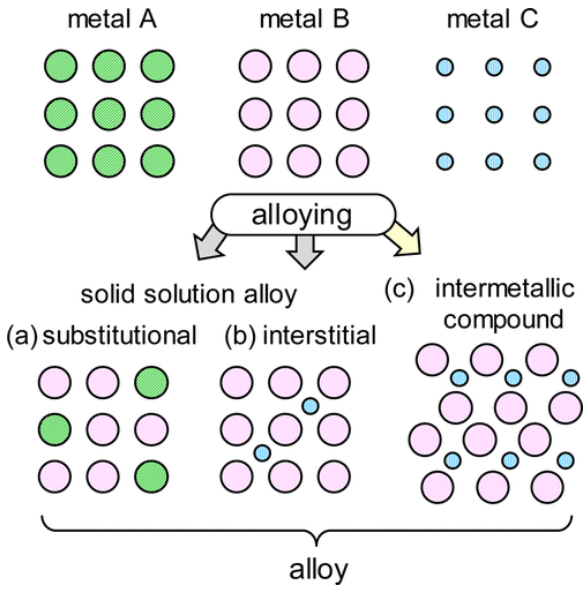

Figure 1.2. Structure of bimetallic alloys: (a) substitutional and (b) interstitial solid-solution alloys and (c) intermetallic compounds.[24]

After mixing of the metals, the electronic and geometric states are drastically changed by the formation of random alloy or intermetallic phase.[24] The effects that intermetallic catalysts provided to enhance catalysis can be divided into several categories such as: (1) electronic effects, (2) geometric effects, (3) steric effects, and (4) ordering effects.[24] Therefore, alloying is one of a promising methodology to improve the catalytic performance.

1.3 Propane dehydrogenation

As we know, propylene is one of the most important feedstocks in producing chemicals and plastic products in the global chemical industry. Conventional propylene production process normally involves fluid catalytic cracking and stem cracking of naphtha and light diesel, deeply relies on the consumption of fossil energy and no longer meets the increasing demands.[2-4] To fill the propylene gap between the world demand and supply, on-purpose propylene production technologies such as propane dehydrogenation (PDH) are of high interest to the petrochemical marketplace.[3] PDH is a process of catalytic conversion of propane into propylene and hydrogen, as illustrated below (Equation (1)):

$$C_3H_8 \leftrightarrow C_3H_6 + H_2 \quad \Delta H^0_{298} = 124.3 \text{ kJ mol}^{-1} \qquad (1)$$

$$C_3H_8 \leftrightarrow CH_4 + C_2H_4 \quad \Delta H^0_{298} = 98.9 \text{ kJ mol}^{-1} \qquad (2)$$

$$C_3H_8 + H_2 \leftrightarrow C_2H_6 + CH_4 \quad \Delta H^0_{298} = -37.7 \text{ kJ mol}^{-1} \qquad (3)$$

$$C_2H_4 + H_2 \leftrightarrow C_2H_6 \quad \Delta H^0_{298} = -136.6 \text{ kJ mol}^{-1} \qquad (4)$$

$$C_3H_8 \leftrightarrow 3C + 4H_2 \quad \Delta H^0_{298} = 119.5 \text{ kJ mol}^{-1} \qquad (5)$$

The reaction is highly endothermic and a temperature range of 500°C to 600°C is required to gain a sufficient equilibrium yield. However, under such high temperatures, side reactions (Equation (2–5)), deactivation by coking and metal sintering, and high energy consumption occur, severely hindering practical usage.[2, 3, 25] In this context, the future development routes include lowering the reaction temperature and designing a PDH catalyst that exhibits high selectivity and stability even at ≥600°C. The former route is very challenging and to be studied. So far, numerous efforts have been made to meet the latter route.

In the past several decades, many heterogeneous catalysts, including metal-based catalysts, metal oxide-based catalysts and non-oxide-based catalysts have been exploited for the direct PDH reaction, as summarized in Figure 1.3.[3]

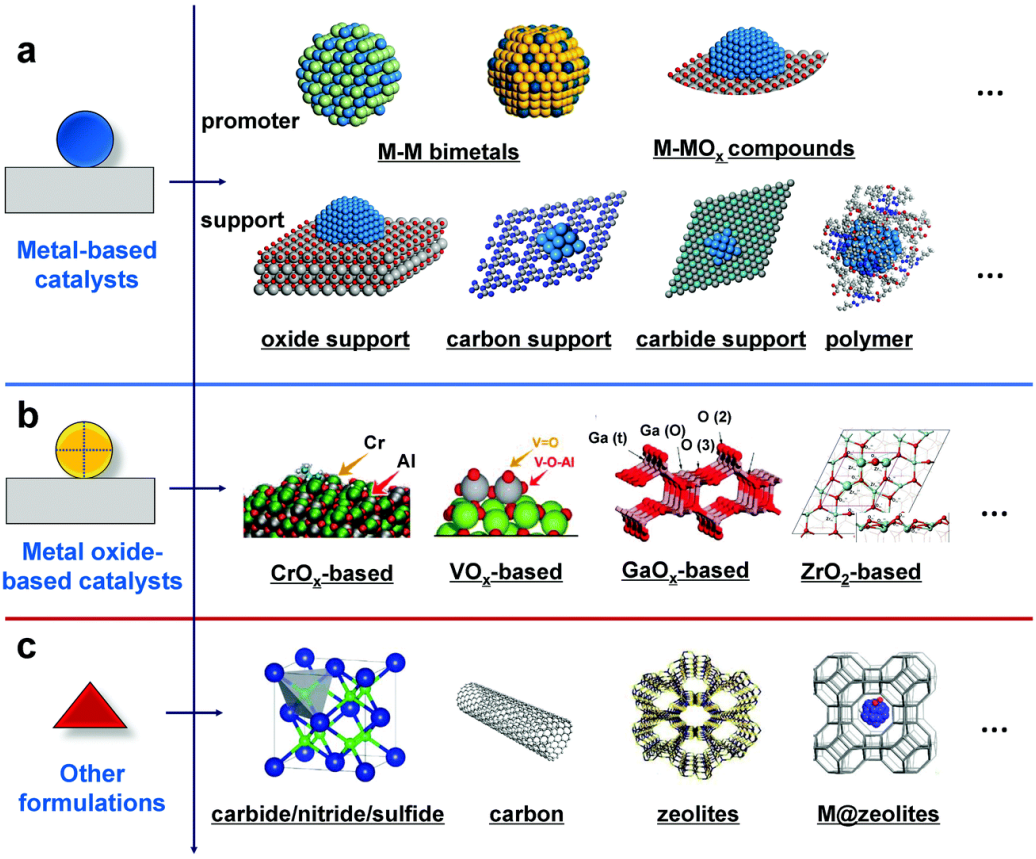

Figure 1.3. Model illustrations of PDH catalysts: (a) metal-based catalysts, (b) metal oxide-based catalysts, and (c) other formulations.[3]

Among them, Pt-based and Cr-based catalysts are the most widely studied and commercially used. As for the most commonly used PDH catalysts so far, the Pt-based catalysts show several advantages compared with others, for instance, higher activity, higher selectivity to propylene, higher stability for longer working periods before regeneration, and better environmental-friendliness.[2, 4] However, deactivation due to poisoning and metal sintering occurs during the reaction under harsh conditions and at high temperatures.[2, 4] Furthermore, Pt-based catalysts cause high cost. Compared with Pt-based catalysts, Cr-based catalysts are much cheaper and also can achieve high reactivity and selectivity. While, chromium oxide is more complex compared with Pt, and it is difficult to explain the reaction and deactivation mechanism.[3] Not mentioning the high toxicity of CrO_x also requires a high cost to dispose the waste catalyst.[2]

To conclude, developing a novel catalytic system for PDH that works at a much lower temperature region is challenging but highly attractive.

1.4 Oxidative coupling of methane using carbon dioxide

Greenhouse gases elimination is an important subject for humankind to avoid global warming, which is already an urgent disaster. Methane and carbon dioxide are greenhouse gases and the main components of natural gas. The valorization of methane to more valuable chemicals and fuels is a promising technology and has gained wide attention.[26] However, it requires a high temperature to activate methane molecules due to its strong C–H bond (434 kJ mol^{-1}). Various routes to activate methane can be classified into three types[27, 28]: (1) reforming of methane to produce syngas, which is converted to chemicals by Fischer–Tropsch process; (2) oxidative coupling of methane (OCM); and (3) conversion to oxygenates such as methanol. Among these, OCM is more promising owing to the direct production of higher value hydrocarbons, especially ethane and ethylene, which are important base chemicals in the global chemical industry. However, a drawback of OCM is the overoxidation of $CH_3\cdot$ radicals by oxygen resulting low C2 hydrocarbons selectivity.[8, 29, 30]

It was firstly found that the combination of CO_2 can promote the OCM reaction by Aika and Nishiyama in 1988.[31] And it was attributed to the decrease of free energy by conversion of CO_2 to CO at 800°C.[31] Moreover, unlike O_2, CO_2 is much milder and will not induce gas-phase radical reactions. Therefore, CO_2 is chosen to replace O_2 in OCM (Equation (6 and 7)) to prevent the sequential reaction of the C2 product in the gas phase.[29, 30, 32]

$$2CH_4 + CO_2 \leftrightarrow C_2H_6 + CO + H_2O \quad \Delta H^0_{298} = 106 \text{ kJ mol}^{-1} \qquad (6)$$

$$2CH_4 + 2CO_2 \leftrightarrow C_2H_4 + 2CO + 2H_2O \quad \Delta H^0_{298} = 284 \text{ kJ mol}^{-1} \qquad (7)$$

CO_2 also is a stable molecule due to its strong C–O bond strength (532 kJ mol^{-1}). Therefore, CO_2–OCM is not thermodynamically favorable even at temperature higher than 900°C.[31] Additionally, the dry reforming of methane (Equation (8)) is a competitive reaction at such high temperature region and lower the hydrocarbons selectivity.

$$CH_4 + CO_2 \leftrightarrow 2CO + 2H_2 \quad \Delta H^0_{298} = 106 \text{ kJ mol}^{-1} \qquad (8)$$

To solve the contradiction of large activity and selectivity, one way is to introduce the solid co-reactants that undergo solid-phase transformations during CO_2–OCM.[27] And another way is to develop various non-conventional catalytic systems such as plasma,[33, 34] discharge,[35] and electric field[9, 11, 36] to achieve low-temperature CO_2–OCM.

For the former way, it has been reported that the lattice oxygen of catalysts participates in the conversion of methane, and then the reduced catalyst needs to be re-oxidized to maintain the activity of the catalyst.[27] Furthermore, CO_2 chemisorption requires suitable basic sites to form active oxygen species for recovering the reduced sites and activating methane. Considering of that, a series of binary oxide systems were developed, consisting of basic oxide and redox-active oxide components, such as CaO–Cr_2O_3, CaO–CeO_2, CaO–ZnO, and Sr–Mn. The proposed mechanism is depicted in Figure 1.4.[37]

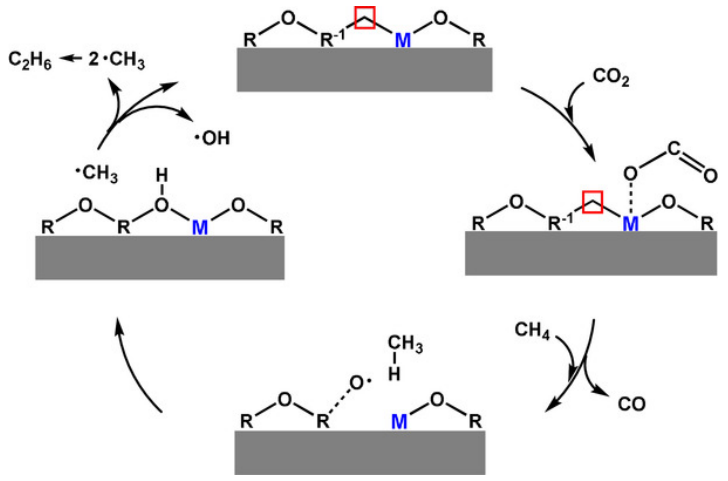

Figure 1.4. Proposed mechanism of CO_2–OCM over binary oxides, where R represents the redox active metal and M represents the basic metal.[37]

To increase the conversion of methane and decrease the reaction temperature, the external-force such as plasma, light, or electricity were introduced into CO_2–OCM. Nonthermal plasma (NTP) is considerably superior in activating thermodynamically stable molecules (e.g., CO_2, CH_4). Larkin et al. achieved low-temperature CO_2–OCM using a plasma reactor in the absence of catalysts.[33] Although methane molecules were activated by plasma, side products such as formaldehyde and syngas were produced inevitably.[33] Compared with that, light is a much milder power source. However, the efficiency of photocatalytic CO_2–OCM is quite low due to

its feasibility only for UV light. Using the electric field is a promising method for low-temperature CO_2–OCM. It was reported that 11% of methane conversion was achieved by imposing 7 mA of direct current on La–ZrO_2 catalyst even at the low external temperature of 423 K.[9]

In summary, CO_2–OCM is a promising reaction to achieve elimination of greenhouse gases and valorization of methane. However, CO_2 and CH_4 both require high energy to dissociate. And the produced higher hydrocarbons are too fragile to retain high selectivity. Therefore, future research is necessary to design and synthesize highly efficient catalysts, which must possess the unique ability to activate the C–H bond of methane without breaking the weak C–H bond of hydrocarbon products.

1.5 Dry reforming of benzene

Compared with fossil fuel, biomass is gaining more and more attention as a source of power, fuel, and other chemical products due to its renewability. When biomass was heated at temperatures above 500°C with a gasifying agent, the produced gas that contains a mixture of hydrogen, carbon monoxide, carbon dioxide, water, nitrogen, and other byproducts was transformed. It can be used to produce hydrocarbons, methanol, and various value-added chemicals, as well as directly used as power source in gas engines, turbines, furnaces et al.[38] However, large amounts of organic impurities, generally referred to as tars are also produced during biomass gasification, which include a significant fraction of aromatics, as shown in Figure 1.5.[39]

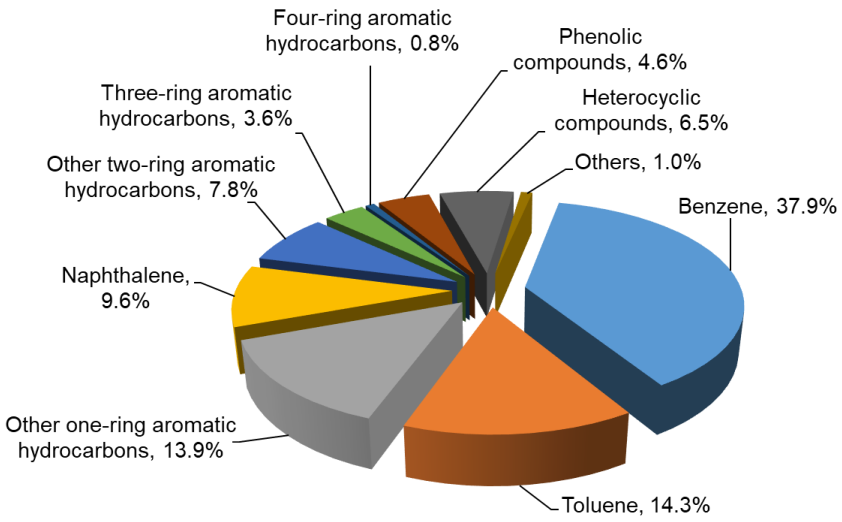

Figure 1.5. Typical composition of biomass gasification tars (wt%).[39]

Therefore, it is crucial to remove the problematic tars at the downstream of the gasifier. The various methods can be physical or chemical. Especially, by using chemical method, the conversion of tars into syngas can increase the value of biomass utilization.[40] The chemical methods to decompose tars include steam reforming, dry reforming, thermal cracking and water-gas shift reaction. Among them, dry reforming is a promising method to achieve complete elimination of tars and simultaneously utilization of carbon dioxide, which is a greenhouse gas.[41] Benzene was selected as a model molecule in various tar components due to its thermal

stability and relatively high weight percentage (Figure 1.5). As shown in Equation (9), 1-mol of benzene can reduce 6-mol of carbon dioxide and produce carbon monoxide.

$$C_6H_6 + 6CO_2 \leftrightarrow 12CO + 3H_2 \quad \Delta H^0_{298} = 948 \text{ kJ mol}^{-1} \qquad (9)$$

The current catalysts in tars elimination can be divided as two classes: minerals and synthetic catalysts. The former exits in nature and can be used directly or with some physical treatment (such as heating), but without chemical treatment. Generally speaking, mineral catalysts are relatively cheap but their catalytic activity is low. Compared with that, synthetic catalysts are chemically produced and relatively more expensive and can complete eliminate tar compounds. Notably, nickel-based catalysts are considered as good catalysts for the dry reforming of methane and hydrocarbons.[42] The main advantages of Ni-based catalysts are their ability to attain complete tar elimination at a temperature of around 900°C[43] and to increase the yield of CO and H_2.

Besides the conventional thermal catalytic decomposition of tars, novel catalytic systems such as non-thermal plasma-,[44] and microwave-assisted[45] reactions decreased the reaction temperature then accordingly save operational cost.

1.6 Aim of this thesis

In my thesis, I focused on an electroassisted catalytic system to achieve low temperature conversions of various robust reactant molecules. There are key factors in electroassisted catalytic system based on surface protonics methodology: (a) Proton hopping on the metal oxide support and proton collision with reactant molecules on the metal-support interface sites. (b) Active sites modification to achieve high activity synergistically with the electric field and improve product high selectivity under strong proton collisions. Therefore, I purposely designed a catalytic system based on the above frameworks:

1) Enrichment of surface protons via surface doping to boost electroassisted catalysis.
   - ✓ Design of Sm surface doped TiO_2 support to increase surface proton density by charge density
2) Development active metal sites to promote catalytic activity and improve product selectivity
   - ✓ Design of Pt_3In intermetallic compound as PDH catalyst;
   - ✓ Design of Pt_3Sn and Pt_3Bi alloy as CO_2–OCM catalysts;
   - ✓ Design of $Ni_{1.5}Co_{1.5}Ge/CeO_2$ catalyst for DRB.

1.6.1 Development of Pt_3In/TiO_2 catalyst for framework 2

As we know, propylene as an important base chemical, the on-purpose propylene production technology such as propane dehydrogenation is of great interest to fill the gradually increasing "propylene gap" between the world demand and supply.[2-4] However, the PDH reaction requires a temperature range of 550°C to 600°C to gain sufficient propylene yield due to its highly endothermic property. Therefore, a novel electroassisted catalytic system based on surface protonics was developed for low-temperature PDH.

The catalytic performance of Pt-based alloy catalysts under electric field was investigated. Furthermore, to inhibit the further decomposition of propylene, Pt was alloyed with In to alter its electronic structure.

1.6.2 Development of Sm surface doped TiO_2 as support for framework 1

Based on the previous, applying electric field catalysis is a promising way to break the thermodynamic equilibrium limitation of propane dehydrogenation at low temperature. In this

reaction system, the overall reaction rate of propylene formation is mainly determined by three factors: (1) the number (concentration) of surface protons, (2) the transition state stability at proton collision, and (3) the selectivity to propylene desorption or decomposition. First, the number of surface protons, which is the density of surface hydroxyl groups, is the key factor that directly determines overall reaction rate. Surface hydroxyl groups can be enriched by doping a hetero-cation on the support oxide surface region by charge compensation. For other factors, we demonstrated that alloying Pt with In to form intermetallic Pt_3In effectively satisfies requirements (2) and (3). As a result, the combination of the two modifications is expected to boost the potential ability for electroassisted PDH at low temperatures, as shown in Scheme 1.2.

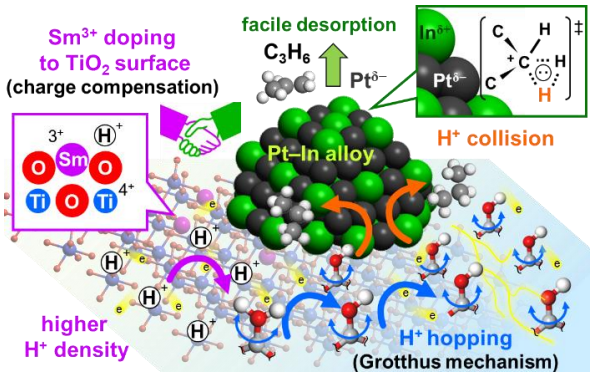

Scheme 1.2. The catalyst design for enhancing electroassisted PDH at low temperatures. Sm^{3+} is doped into TiO_2 surface to increase the number of surface protons by charge compensation. Pt–In alloy is used for selective formation of propylene and to enhance the proton collision with propane.

1.6.3 Development of Pt-based binary alloy loaded on CeO_2 catalyst for framework 2

Valorization of methane to valuable chemicals via methane coupling reaction is a promising technology and gained wide attention. Oxidative coupling of methane using carbon dioxide (CO_2–OCM) is able to directly produce C2 and C3 hydrocarbons and eliminate greenhouse gases i.e., methane and carbon dioxide. High reaction temperatures and side reactions such as dry reforming is inevitable under thermal conditions due to the strong C–H and C–O bonds. Therefore, a novel electroassisted catalytic system based on surface protonics is a promising methodology to achieve low-temperature conversion of methane and carbon dioxide. Besides, the design of Pt-based bimetallic alloy loaded on CeO_2 catalyst is beneficial for high catalytic activity and selectivity.

1.6.4 Development of Ni-based ternary alloy loaded on CeO_2 catalyst for framework 2

Biomass is an important source of power in the future due to its renewability and environmental properties. Furthermore, the chemical conversion of problematic tars compounds derived biomass gasification process is able to protect production equipment and increase value of biomass utilization. Dry reforming of benzene as a model compound in tars is a promising method to achieve complete elimination of tars and simultaneously utilization of carbon dioxide which is a greenhouse gas. However, due to its strong endothermicity, dry reforming of benzene (DRB) requires high temperatures, resulting carbon deposition and metal sintering. Therefore, electroassisted catalysis based on surface protonics methodology is highly attractive.

1.7 Outline of thesis

This thesis focuses on the usage and modification of electroassisted catalytic system in various reactions: (a) propane dehydrogenation, (b) oxidative methane coupling using carbon dioxide, (c) dry reforming of benzene. The delicate design of the surface protonics methodology and active sites facilitates high catalytic activity and selectivity.

Chapter 2 presents the combination of a surface protonics methodology with intermetallic active sites to achieve propane dehydrogenation reaction at low temperature. First, the propylene yield increased monotonously with an increase in the supplied electric power, showing a significant dependence on the electric power. The highest propylene yield of 10.2% was achieved using 3.2 W of electric power, far beyond the thermodynamic equilibrium limitation (0.15%) at such low external temperature (250°C). The propylene yield and selectivity were remarkably improved by alloying of In. A detailed reaction mechanism was determined from kinetic analysis including kinetic isotope test, Eyring plots, and quasi-stationary approximation. Under an electric field, H^+ hopping is facilitated by the Grotthuss mechanism and H^+ collisions with propane allow its activation via a three-center transition state to generate $C_3H_7^+$ and H_2. Here, alloying of Pt with In promotes this process, probably because the electron-enriched Pt stabilizes the cationic transition state and $C_3H_7^+$ intermediate. The $C_3H_7^+$ intermediate is then converted to C_3H_6 and recovers H^+. The electron-enriched Pt can also enhance propylene desorption because of the weaker adsorption, which decreases the probability of propylene decomposition and increases its selectivity. Thus, Pt–In/TiO_2 works as an efficient catalyst for electro-assisted PDH at low temperatures.

Chapter 3 proposes a catalyst design concept for more efficient electroassisted PDH at low temperature. Sm was doped into the anatase TiO_2 surface to increase the surface proton density by charge compensation. Electric field catalysis using surface proton conduction, in which proton hopping and collision on the reactant are promoted by external electricity, is a promising approach to break the thermodynamic equilibrium limitation in endothermic propane dehydrogenation (PDH). Pt–In alloy was deposited on the Sm-doped TiO_2 for more favorable proton collision and selective propylene formation. The catalytic activity in electroassisted PDH drastically increased by doping an appropriate amount of Sm (1mol % to Ti) where the

highest propylene yield of 19.3% was obtained at 300°C where the thermodynamic equilibrium yield was only 0.5%. The results show that surface proton enrichment boosts alkane dehydrogenation at low temperature.

Chapter 4 presents the development of an electroassisted catalytic system for low-temperature oxidative coupling of methane using carbon dioxide (CO_2–OCM) over Pt-based bimetallic alloy loaded on a CeO_2 support. The highest C2 hydrocarbon yield of 4.06% was achieved over Pt_3Sn/CeO_2 catalyst using 2.73 W of electric power even at a low external temperature of 300°C. Notably, the yield of C3 hydrocarbons (0.34%) was also remarkably increased by electricity compared with the thermodynamic equilibrium yield (virtually zero).

Chapter 5 proposes a novel catalytic system for electroassisted dry reforming of benzene. By imposing 2.7 W of electric power, 28% of CO yield was achieved over $Ni_{1.5}Co_{1.5}Ge/CeO_2$ catalyst at a low external temperature (200°C) while the thermodynamic equilibrium yield is only 7.7%. From the results of XAFS, Ni, Co, and Ge formed alloy on CeO_2 support. The alloying of Ni with Co and Ge synergistically promoted the consumption of benzene and carbon dioxide. Although this work is still under-research, it shows a promising methodology for low temperature conversion of tars.

1.8 Concluding remarks

I have developed the usage of electric field in various reactions to achieve the low-temperature conversions. The delicate design of surface protonics methodology and active sites remarkably improved the electroassisted catalytic performance. This present study provides a novel catalytic system for low-temperature reactions.

References

1. Sekine, Y.; Manabe, R., Reaction mechanism of low-temperature catalysis by surface protonics in an electric field. *Faraday Discuss.* **2021,** *229*, 341–358.

2. Wang, G.; Zhu, X.; Li, C., Recent Progress in Commercial and Novel Catalysts for Catalytic Dehydrogenation of Light Alkanes. *Chem. Rec.* **2020,** *20*, 604–616.

3. Chen, S.; Chang, X.; Sun, G.; Zhang, T.; Xu, Y.; Wang, Y.; Pei, C.; Gong, J., Propane dehydrogenation: catalyst development, new chemistry, and emerging technologies. *Chem. Soc. Rev.* **2021,** *50*, 3315–3354.

4. Dai, Y.; Gao, X.; Wang, Q.; Wan, X.; Zhou, C.; Yang, Y., Recent progress in heterogeneous metal and metal oxide catalysts for direct dehydrogenation of ethane and propane. *Chem. Soc. Rev.* **2021,** *50*, 5590–5630.

5. Nakaya, Y.; Xing, F.; Ham, H.; Shimizu, K.-i.; Furukawa, S., Doubly Decorated Platinum-Gallium Intermetallics as Stable Catalysts for Propane Dehydrogenation. *Angew. Chem. Int. Ed.* **2021,** *60*, 19715–19719.

6. Kim, D.-Y.; Ham, H.; Chen, X.; Liu, S.; Xu, H.; Lu, B.; Furukawa, S.; Kim, H.-H.; Takakusagi, S.; Sasaki, K.; Nozaki, T., Cooperative Catalysis of Vibrationally Excited CO_2 and Alloy Catalyst Breaks the Thermodynamic Equilibrium Limitation. *J. Am. Chem. Soc.* **2022,** *144*, 14140–14149.

7. Manabe, R.; Okada, S.; Inagaki, R.; Oshima, K.; Ogo, S.; Sekine, Y., Surface Protonics Promotes Catalysis. *Sci. Rep.* **2016,** *6*, 1–7.

8. Tanaka, K.; Sekine, Y.; Oshima, K.; Tanaka, Y.; Matsukata, M.; Kikuchi, E., Catalytic Oxidative Coupling of Methane Assisted by Electric Power over a Semiconductor Catalyst. *Chem. Lett.* **2012,** *41*, 351–353.

9. Oshima, K.; Tanaka, K.; Yabe, T.; Kikuchi, E.; Sekine, Y., Oxidative coupling of methane using carbon dioxide in an electric field over La–ZrO_2 catalyst at low external temperature. *Fuel* **2013,** *107*, 879–881.

10. Sugiura, K.; Ogo, S.; Iwasaki, K.; Yabe, T.; Sekine, Y., Low-temperature catalytic oxidative coupling of methane in an electric field over a Ce–W–O catalyst system. *Sci. Rep.* **2016,** *6*, 1–9.

11. Yabe, T.; Kamite, Y.; Sugiura, K.; Ogo, S.; Sekine, Y., Low-temperature oxidative coupling of methane in an electric field using carbon dioxide over Ca-doped $LaAlO_3$ perovskite oxide catalysts. *J. CO_2 Util.* **2017,** *20*, 156–162.

12. Yabe, T.; Mitarai, K.; Oshima, K.; Ogo, S.; Sekine, Y., Low-temperature dry reforming of methane to produce syngas in an electric field over La-doped Ni/ZrO_2 catalysts. *Fuel Process. Technol.* **2017,** *158*, 96–103.

13. Inagaki, R.; Manabe, R.; Hisai, Y.; Kamite, Y.; Yabe, T.; Ogo, S.; Sekine, Y., Steam reforming of dimethyl ether promoted by surface protonics in an electric field. *Int. J. Hydrog. Energy* **2018,** *43*, 14310–14318.

14. Takise, K.; Sato, A.; Murakami, K.; Ogo, S.; Seo, J. G.; Imagawa, K.-i.; Kado, S.; Sekine, Y., Irreversible catalytic methylcyclohexane dehydrogenation by surface protonics at low temperature. *RSC Adv.* **2019,** *9*, 5918–5924.

15. Agmon, N., The grotthuss mechanism. *Chem. Phys. Lett.* **1995,** *244*, 456–462.

16. Manabe, R.; Nakatsubo, H.; Gondo, A.; Murakami, K.; Ogo, S.; Tsuneki, H.; Ikeda, M.; Ishikawa, A.; Nakai, H.; Sekine, Y., Electrocatalytic synthesis of ammonia by surface proton hopping. *Chem. Sci.* **2017,** *8*, 5434–5439.

17. Murakami, K.; Manabe, R.; Nakatsubo, H.; Yabe, T.; Ogo, S.; Sekine, Y., Elucidation of the role of electric field on low temperature ammonia synthesis using isotopes. *Catalysis Today* **2018,** *303*, 271–275.

18. Okada, S.; Manabe, R.; Inagaki, R.; Ogo, S.; Sekine, Y., Methane dissociative adsorption in catalytic steam reforming of methane over Pd/CeO_2 in an electric field. *Catal. Today* **2018,** *307*, 272–276.

19. Torimoto, M.; Ogo, S.; Harjowinoto, D.; Higo, T.; Seo, J. G.; Furukawa, S.; Sekine, Y., Enhanced methane activation on diluted metal-metal ensembles under an electric field: breakthrough in alloy catalysis. *Chem. Commun.* **2019,** *55*, 6693–6695.

20. Yabe, T.; Yamada, K.; Murakami, K.; Toko, K.; Ito, K.; Higo, T.; Ogo, S.; Sekine, Y., Role of Electric Field and Surface Protonics on Low-Temperature Catalytic Dry Reforming of Methane. *ACS Sustain. Chem. Eng.* **2019,** *7*, 5690–5697.

21. Nakano, N.; Torimoto, M.; Sampei, H.; Yamashita, R.; Yamano, R.; Saegusa, K.; Motomura, A.; Nagakawa, K.; Tsuneki, H.; Ogo, S.; Sekine, Y., Elucidation of the

reaction mechanism on dry reforming of methane in an electric field by in situ DRIFTs. *RSC Adv.* **2022,** *12*, 9036–9043.

22. Han, Q.; Tanaka, A.; Matsumoto, M.; Endo, A.; Kubota, Y.; Inagaki, S., Conversion of methane to C2 and C3 hydrocarbons over TiO_2/ZSM-5 core–shell particles in an electric field. *RSC Adv.* **2019**, *9*, 34793-34803.

23. Nakaya, Y.; Furukawa, S., Catalysis of Alloys: Classification, Principles, and Design for a Variety of Materials and Reactions. *Chem. Rev.* **2022** (DOI: 10.1021/acs.chemrev.2c00356).

24. Furukawa, S.; Komatsu, T., Intermetallic Compounds: Promising Inorganic Materials for Well-Structured and Electronically Modified Reaction Environments for Efficient Catalysis. *ACS Cat.* **2016,** *7*, 735–765.

25. Sattler, J. J.; Ruiz-Martinez, J.; Santillan-Jimenez, E.; Weckhuysen, B. M., Catalytic dehydrogenation of light alkanes on metals and metal oxides. *Chem. Rev.* **2014,** *114*, 10613–53.

26. Olivos-Suarez, A. I.; Szécsényi, À.; Hensen, E. J. M.; Ruiz-Martinez, J.; Pidko, E. A.; Gascon, J., Strategies for the Direct Catalytic Valorization of Methane Using Heterogeneous Catalysis: Challenges and Opportunities. *ACS Cat.* **2016,** *6*, 2965–2981.

27. Cai, X.; Hu, Y. H., Advances in catalytic conversion of methane and carbon dioxide to highly valuable products. *Energy Sci. & Eng.* **2019,** *7*, 4–29.

28. Chen, Y.; Mu, X.; Luo, X.; Shi, K.; Yang, G.; Wu, T., Catalytic Conversion of Methane at Low Temperatures: A Critical Review. *Energy Technol.* **2019,** *8,* 1–12.

29. Amariglio, A.; Paréja, P.; Amariglio, H., Does C–C Bonding Proceed during Exposure of Adequate Metal Surfaces to CH_4? Reply to "Comment by Z. Hlavathy, Z. Paál, and P. Tétényi". *J. Catal.* **1997,** *166*, 121–123.

30. Asami, K.; Fujita, T.; Kusakabe, K.-i.; Nishiyama, Y.; Ohtsuka, Y., Conversion of methane with carbon dioxide into C2 hydrocarbons over metal oxides. *Appl. Catal. A: Gen.* **1995,** *126*, 245–255.

31. Aika, K.-i.; Nishiyama, T., Utilisation of CO_2 in the oxidative coupling of methane over PbO–MgO and PbO–CaO. *J. of the Chem. Soc., Chem. Commun.* **1988,** 70–71.

32. Istadi; Amin, N. A. S., Synergistic effect of catalyst basicity and reducibility on performance of ternary CeO_2-based catalyst for CO_2 OCM to C2 hydrocarbons. *J. of Mol. Catal. A: Chem.* **2006,** *259*, 61–66.

33. Larkin, D. W.; Caldwell, T. A.; Lobban, L. L.; Mallinson, R. G., Oxygen Pathways and Carbon Dioxide Utilization in Methane Partial Oxidation in Ambient Temperature Electric Discharges. *Energy & Fuels* **1998,** *12*, 740–744.

34. Zhang, X.; Dai, B.; Zhu, A.; Gong, W.; Liu, C., The simultaneous activation of methane and carbon dioxide to C2 hydrocarbons under pulse corona plasma over La_2O_3/γ-Al_2O_3 catalyst. *Catal. Today* **2002,** *72*, 223–227.

35. Eliasson, B.; Liu, C.-j.; Kogelschatz, U., Direct Conversion of Methane and Carbon Dioxide to Higher Hydrocarbons Using Catalytic Dielectric-Barrier Discharges with Zeolites. *Ind. Eng. Chem. Res.* **2000,** *39*, 1221–1227.

36. Oshima, K.; Shinagawa, T.; Sekine, Y., Methane Conversion Assisted by Plasma or Electric Field. *J. Japan Pet. Inst.* **2013,** *56*, 11–21.

37. Arinaga, A. M.; Ziegelski, M. C.; Marks, T. J., Alternative Oxidants for the Catalytic Oxidative Coupling of Methane. *Angew Chem. Int. Ed. Engl.* **2021,** *60*, 10502–10515.

38. Gusta, E.; Dalai, A. K.; Uddin, M. A.; Sasaoka, E., Catalytic Decomposition of Biomass Tars with Dolomites. *Energy & Fuels* **2009,** *23*, 2264–2272.

39. Coll, R.; Salvadó, J.; Farriol, X.; Montané, D., Steam reforming model compounds of biomass gasification tars: conversion at different operating conditions and tendency towards coke formation. *Fuel Process. Technol.* **2001,** *74*, 19–31.

40. Torres, W.; Pansare, S. S.; Goodwin, J. G., Hot Gas Removal of Tars, Ammonia, and Hydrogen Sulfide from Biomass Gasification Gas. *Cata. Rev.* **2007,** *49*, 407–456.

41. Simell, P. A.; Hakala, N. A. K.; Haario, H. E.; Krause, A. O. I., Catalytic Decomposition of Gasification Gas Tar with Benzene as the Model Compound. *Ind. Eng. Chem. Res.* **1997,** *36*, 42–51.

42. Aziz, M. A. A.; Jalil, A. A.; Wongsakulphasatch, S.; Vo, D. V. N., Understanding the role of surface basic sites of catalysts in CO_2 activation in dry reforming of methane: a short review. *Catal. Sci. & Technol.* **2020,** *10*., 35–45.

43. Aznar, M. P.; Corella, J.; Delgado, J.; Lahoz, J., Improved steam gasification of lignocellulosic residues in a fluidized bed with commercial steam reforming catalysts. *Ind. Eng. Chem. Res.* **1993,** *32*, 1–10.

44. Saleem, F.; Zhang, K.; Harvey, A. P., Decomposition of benzene as a tar analogue in CO_2

and H_2 carrier gases, using a non-thermal plasma. *Chem. Eng. J.* **2019,** *360*, 714–720.

45. Chun, Y. N.; Song, H. G., Microwave-induced cracking and reforming of benzene on activated carbon. *Chem. Eng. Process.* **2019,** *135*, 148–155.

Chapter 2

Electro-Assisted Propane Dehydrogenation at Low Temperatures

2. Electro-Assisted Propane Dehydrogenation at Low Temperatures

2.1 Introduction

Propylene is one of the most important base chemicals in the industry for the production of polymers, resins, solvents, and other fine chemicals.[1-3] However, the traditional supply of propylene by refinery and steam crackers can no longer meet the increasing world demand. So, developing on-purpose technique for propylene production is highly demanded.[1-3] In past few years, the large-scale exploitation of shale gas brought a blowout of propane yield. Therefore, catalytic propane dehydrogenation (PDH) is a promising way to fill the "propylene gap." It has been a topical theme in pure and applied chemistry; the increased number of papers and reviews on this topic illustrates this.[1-3] Owing to its endothermicity, PDH requires temperatures higher than 600°C to obtain sufficiently high propane conversion. However, undesirable side reactions, such as over dehydrogenation, C–C cracking, and coking, typically occur at such high temperatures, resulting in catalyst deactivation after a short period due to coke accumulation.[1-3] The recent research trend aims to design a catalyst with long-term stability, even at high temperatures.[1-3] On the other hand, such high-temperature processes are highly energy consuming and require a high cost for operation.

Another possible and pioneering approach is the development of a novel catalytic system that can produce propylene at low temperatures. Using an external-force system, such as photo-, electro-, or plasma-assisted catalysis, the low equilibrium conversion of propane can be boosted due to the large gain of free energy. Electroassisted catalysis using "surface protonics" is a promising methodology for such low-temperature conversion.[4, 5] By imposing an electric field to a catalyst, proton hopping via surface hydroxyl groups known as the Grotthuss mechanism can be facilitated,[4, 5] enabling strong proton collisions with reactant molecules. Robust molecules, such as N_2, CH_4,[6] or CO_2[7, 8], can be activated by surface protonics and transformed to value-added chemicals, even at low temperatures (NH_3, H_2, or CO at 150°C–300°C). Although this methodology is also valid for low-temperature PDH, there is another problem: the propylene product is more reactive than the reactant propane. Therefore, the undesirable decomposition of propylene can be triggered by strong proton collisions. Hence, retaining high propylene selectivity is a challenge in electro-assisted PDH compared to conventional thermal

PDH.

This paper reports that a combination of a surface protonics methodology with intermetallic active sites could overcome this challenge. The alloying of Pt with In significantly improved the propylene selectivity and greatly enhanced the catalytic activity. In this process, two orders of magnitude higher propylene yield (10.2%) than at thermodynamic equilibrium (0.1% at 250°C) was achieved. This paper reports this novel and efficient catalytic system for PDH that works efficiently at low temperatures.

2.2 Experimental section

2.2.1 Catalyst preparation

For electro-assisted catalysis, a reducible oxide support that has surface hydroxyl groups should be used because conductivity and surface protons are necessary for surface protonics. In this study, the Degussa P25 TiO_2 was used as the catalyst support. Pt/TiO_2 and $Pt–In/TiO_2$ catalysts were prepared by an (co-)impregnation method using an excess amount of water (ca. 25 mL of ion-exchanged water per g of support). The TiO_2 support was added to a vigorously stirred aqueous solution containing $Pt(NH_3)_2(NO_3)_2$ (Furuya Metal Co. Ltd., purchased as an aqueous solution with 4.96 wt% of Pt) and/or $In(NO_3)_3{\cdot}8.8{\cdot}H_2O$ (Kanto, 99%), followed by stirring for 3 h. The mixture was dried under a reduced pressure at 50℃, followed by reduction under flowing H_2 (50 $mL{\cdot}min^{-1}$) at 500℃ for 1 h. The loading amounts of Pt was adjusted to 3.0 wt% and Pt/In ratio was fixed to 1.

2.2.2 Characterization

HAADF-STEM analysis was carried out using a JEOL JEM-ARM200 M microscope equipped with an energy dispersive X-ray (EDX) analyzer (EX24221M1G5T) at an accelerating voltage of 200 kV. To prepare the TEM specimen, all samples were sonicated in ethanol and then dispersed on a Mo grid supported by an ultrathin carbon film.

CO pulse chemisorption was performed for all the prepared catalysts using BELCAT II (Microtrac BEL) to estimate the dispersion of noble metals (Pd and Pt). Prior to chemisorption, the catalyst was pretreated under a 5% H_2/Ar flow (40 $mL{\cdot}min^{-1}$) at 400 ℃ for 0.5 h. After the reduction pretreatment, Helium was introduced at the same temperature for 10 min to remove the chemisorbed hydrogen, followed by cooling to room temperature. A 10% CO/He pulse was introduced into the reactor, and the supplied CO flow was quantified downstream by a thermal conductivity detector. Metal dispersion was calculated as a fraction (%) of exposed Pt to those in the catalyst assuming 1:1 adsorption stoichiometry.

XAFS measurements of the $Pt–In/TiO_2$ catalyst and reference foils were performed at BL14B2 beamline of SPring-8, Japan Synchrotron Radiation Research Institute. A Si(111) double-crystal was used as a monochromator. The spectra were recorded at the Pt L_{III}- and In K-edges in transmission modes at room temperature. First, the catalyst was pressed into a pellet

(diameter: 7 mm) and reduced under flowing H_2 at 500 °C for 0.5 h. Then, the reduced sample was then transferred into an Ar glove box (O_2: < 0.001 ppm) without exposing to air and sealed in a plastic bag (Barrier Nylon) with an ISO A500-HS oxygen absorber (Fe powder). The measurements for foil samples were done in air. The obtained XAFS spectra were analyzed using Athena and Artemis software ver. 0.9.25 included in the Demeter package.[9] The k^3-weighted EXAFS oscillation was Fourier-transformed in the k range of 3−12 $Å^{-1}$ for all samples. Curve-fitting was performed using the back Fourier-transforms of the coordination peaks ranging between 1.5−3.0 Å and 1.5−3.7 Å for Pt L_{III}- and In K-edges, respectively. The back-scattering amplitude and phase shift functions were calculated by FEFF8.[10]

2.2.3 Catalytic reaction

Thermal and electro-assisted PDH was carried out using a continuous flow fixed-bed quartz reactor with 6 mm internal diameter. The detailed setup of the reactor is shown in Figure 2.1. The Pt/TiO_2 or Pt–In/TiO_2 catalyst (100.0 mg, Pt: 3 wt%, powder) was placed on a pies of glass wool in the quartz tube reactor. Two stainless steel rods (φ: 2mm) were inserted into the reactor as electrodes and contacted with the top and bottom of the catalyst bed. A K-type thermocouple covered with a glass capillary tube (for insulation protection) was also contacted with the catalyst bed to bed to measure the catalyst bed temperature separately from the furnace temperature.

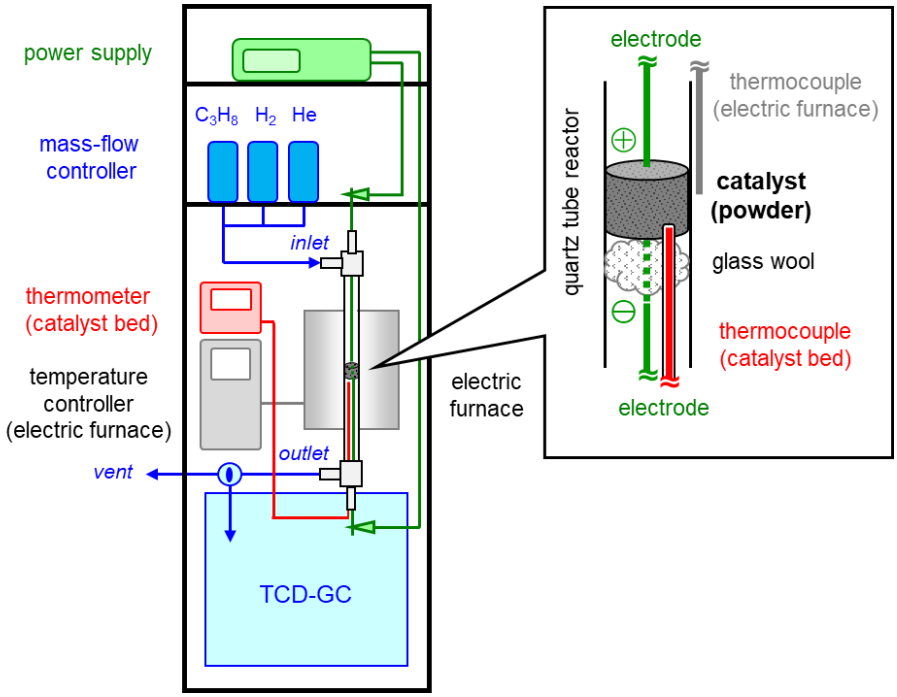

Figure 2.1. The detailed setup of the reactor for electro-assisted PDH. The thermocouple for the catalyst bed was covered with a capillary glass tube for insulation protection. Thermal PDH was also performed using this reactor without imposing direct current.

Prior to the catalytic reaction, the catalyst was pretreated under flowing H_2/He (5/10 mL·min^{-1}) at 300°C for 0.5 h, followed by purging under flowing He (10 mL·min^{-1}) at the reaction temperature. A constant direct current (5–60mA) was imposed to the catalyst bed using a high voltage DC power supply (Tektronix Keithley SMU 2657A). Activity tests were conducted under a reaction gas flow (C_3H_8/He = 10/10 mL·min^{-1}) at specific temperatures (250–330°C for electro-assisted PDH and 450–480°C for thermal PDH, respectively). Product gas was analyzed using a thermal conductivity detection gas chromatograph (Shimadzu GC-8A, column: Unipak S). The C_3H_8 conversion, C_3H_6 selectivity, C_3H_6 yield, and carbon balance were defined as follows:

$$\mathrm{C_3H_8\ conversion:}\ X_{\mathrm{C_3H_8}}\ (\%) = \frac{[\mathrm{C_3H_8}]_{\mathrm{in}} - [\mathrm{C_3H_8}]_{\mathrm{out}}}{[\mathrm{C_3H_8}]_{\mathrm{in}}} \times 100$$

$$\mathrm{C_3H_6\ selectivity:}\ S_{\mathrm{C_3H_6}}\ (\%) = \frac{[\mathrm{C_3H_6}]_{\mathrm{out}} \times 100}{[\mathrm{C_3H_6}]_{\mathrm{out}} + \frac{2}{3}[\mathrm{C_2H_6}]_{\mathrm{out}} + \frac{2}{3}[\mathrm{C_2H_4}]_{\mathrm{out}} + \frac{1}{3}[\mathrm{CH_4}]_{\mathrm{out}}}$$

C_3H_6 yield: $Y_{C_3H_6}$ (%) $= \frac{X_{C_3H_8} \cdot S_{C_3H_6}}{100}$

Carbon balance: C_b(%)

$$= \frac{[C_3H_8]_{out} + [C_3H_6]_{out} + \frac{2}{3}[C_2H_6]_{out} + \frac{2}{3}[C_2H_4]_{out} + \frac{1}{3}[CH_4]_{out}}{[C_3H_8]_{in}}$$

2.2.4 Kinetic analysis

We conducted kinetic analysis using a quasi-stationary approximation, which estimates the possible ranges of reaction orders and can be verified by the experimental values. We considered the following Langmuir-Hinshelwood type mechanism for electro-assisted PDH:

$H^+ \cdot \sigma_0 \overset{E_p}{\underset{E_p}{\leftrightharpoons}} H^+ \cdot \sigma_i$ (1) proton hopping

$C_3H_8 + \sigma_m \rightleftharpoons C_3H_8 \cdot \sigma_m$ (2) propane physisorption

$C_3H_8 \cdot \sigma_m + H^+ \cdot \sigma_i \overset{E_p}{\rightarrow} {C_3H_7}^+ \cdot \sigma_m + H_2 + \sigma_i$ (3) proton collision (RDS)

${C_3H_7}^+ \cdot \sigma_m + \sigma_i \overset{E_p}{\leftrightharpoons} C_3H_6 \cdot \sigma_m + H^+ \cdot \sigma_i$ (4) deprotonation

$C_3H_6 \cdot \sigma_m \rightleftharpoons C_3H_6 + \sigma_m$ (5) propylene desorption

where, σ_0, σ_i, and σ_m indicate proton acceptor on TiO_2 surface (excess), proton acceptor at metal-support interface, and metallic adsorption site, respectively. For elementary steps other than the RDS, the forward and reverse reactions can be regarded as being at equilibrium; therefore, equilibrium constants K_i are defined as follows:

$$K_1 = \frac{\theta_{H^+}}{C_0}$$

$$K_2 = \frac{\theta_{C_3H_8}}{P_{C_3H_8}(1-\theta)_m}$$

$$K_4 = \frac{\theta_{C_3H_6}\theta_{H^+}}{\theta_{C_3H_7^+}(1-\theta)_p E_p}$$
$$K_5 = \frac{P_{C_3H_6}(1-\theta)_m}{\theta_{C_3H_6}}$$

where, θ_{H^+}, $\theta_{C_3H_x}$, C_0, and E_p are H^+ coverage at perimeter sites, C_3H_x coverage at metallic adsorption sites, surface proton density (regarded as constant), and electric power supplied to the system, respectively. $(1-\theta)_p$ and $(1-\theta)_m$ indicate the vacancy of σ_p and σ_m, respectively, and can be expressed using θ_x according to as follows:

$$(1-\theta)_p = 1 - \theta_{H^+}$$
$$(1-\theta)_m = 1 - \theta_{C_3H_8} - \theta_{C_3H_7^+} - \theta_{C_3H_6}$$

Here, the overall reaction rate can be described using the rate equation of the RDS (step 3) as follows:

$$r = k_3\theta_{C_3H_8}\theta_{H^+}E_p$$

Note that the contribution of the reverse reaction was ignored because of the differential condition (low conversion). This equation is converted to the following form using the equations of K_1 and K_2:

$$r = k_3K_1K_2C_0P_{C_3H_8}E_p(1-\theta)_m$$

Then, the site conservation equation is solved for $(1-\theta)_m$ using the equations of K_i:

$$(1-\theta)_m + \theta_{C_3H_8} + \theta_{C_3H_7^+} + \theta_{C_3H_6} = 1$$
$$(1-\theta)_m + K_2P_{C_3H_8}(1-\theta)_m + \frac{K_1C_0}{1-K_1C_0}K_4^{-1}K_5^{-1}P_{C_3H_6}E_p^{-1}(1-\theta)_m + K_5^{-1}P_{C_3H_6}(1-\theta)_m = 1$$
$$\therefore\ (1-\theta)_m = \left(1 + K_2P_{C_3H_8} + K_5^{-1}P_{C_3H_6} + \frac{K_4^{-1}K_5^{-1}P_{C_3H_6}}{(K_1^{-1}C_0^{-1}-1)E_p}\right)^{-1}$$

Thus, we obtain the rate equation as follows:

$$r = \frac{k_3 K_1 K_2 C_0 P_{C_3H_8} E_p}{1 + K_2 P_{C_3H_8} + K_5^{-1} P_{C_3H_6} + \frac{K_4^{-1} K_5^{-1} P_{C_3H_6}}{(K_1^{-1} C_0^{-1} - 1) E_p}}$$

Next, this equation is regarded as a function of the single valuable, $P_{C_3H_8}$ or E_p.

$$r = k {P_{C_3H_8}}^{\alpha} {E_p}^{\beta}$$

Here, two limits of the rate equation are considered such that the order dependence of $P_{C_3H_8}$ becomes the largest and smallest, which provides the possible range of reaction order α.

When $K_2 \gg 1, K_5^{-1} P_{C_3H_6}, \frac{K_4^{-1} K_5^{-1} P_{C_3H_6}}{(K_1^{-1} C_0^{-1} - 1) E_p}$, this equation can be simplified as follows:

$$r = \frac{k_3 K_1 C_0 P_{C_3H_8} E_p}{P_{C_3H_8} + 1/K_2 + K_5^{-1} P_{C_3H_6}/K_2 + \frac{K_4^{-1} K_5^{-1} P_{C_3H_6}}{(K_1^{-1} C_0^{-1} - 1) E_p}/K_2}$$

$$r \approx k_3 K_1 C_0 E_p$$

$$\because \left(1/K_2, K_5^{-1} P_{C_3H_6}/K_2, \frac{K_4^{-1} K_5^{-1} P_{C_3H_6}}{(K_1^{-1} C_0^{-1} - 1) E_p}/K_2 \ll 1\right)$$

On the contrary, when $K_2 \ll 1$, this equation can be simplified as follows:

$$r = \frac{k_3 K_1 K_2 C_0 P_{C_3H_8} E_p}{1 + K_5^{-1} P_{C_3H_6} + \frac{K_4^{-1} K_5^{-1} P_{C_3H_6}}{(K_1^{-1} C_0^{-1} - 1) E_p}}$$

Therefore, the reaction order α can be 0 and 1 at the higher and lower limit and should always fall into this range.

Similarly, the rate equation is regarded as a function of E_p and two limits of this equation are considered such that the order dependence of E_p becomes the largest and smallest, which provides the possible range of reaction order β.

When $\frac{K_4^{-1} K_5^{-1} P_{C_3H_6}}{K_1^{-1} C_0^{-1} - 1} \gg 1, K_2 P_{C_3H_8}, K_5^{-1} P_{C_3H_6}$, this equation can be simplified as follows:

$$r = \frac{k_3 K_1 K_2 C_0 P_{C_3H_8} E_p}{E_p^{-1} + 1/\frac{K_4^{-1} K_5^{-1} P_{C_3H_6}}{K_1^{-1} C_0^{-1} - 1} + K_2 P_{C_3H_8}/\frac{K_4^{-1} K_5^{-1} P_{C_3H_6}}{K_1^{-1} C_0^{-1} - 1} + 1/\frac{K_4^{-1}}{K_1^{-1} C_0^{-1} - 1}}$$

$$r \approx k_3 K_1 K_2 C_0 P_{C_3H_8} {E_p}^2$$

$$\because \left(1/\frac{K_4^{-1}K_5^{-1}P_{C_3H_6}}{K_1^{-1}C_0^{-1}-1}, K_2 P_{C_3H_8}/\frac{K_4^{-1}K_5^{-1}P_{C_3H_6}}{K_1^{-1}C_0^{-1}-1}, 1/\frac{K_4^{-1}}{K_1^{-1}C_0^{-1}-1} \ll 1\right)$$

On the contrary, when $\frac{K_4^{-1}K_5^{-1}P_{C_3H_6}}{K_1^{-1}C_0^{-1}-1} \ll 1$, this equation can be simplified as follows:

$$r = \frac{k_3 K_1 K_2 C_0 P_{C_3H_8} E_p}{1 + K_2 P_{C_3H_8} + K_5^{-1} P_{C_3H_6}}$$

Based on this derivation, the reaction orders for $P_{C_3H_8}$ (α) and E_p (β) on the overall reaction rate should be described as follows: $0 < \alpha < 1,\ 1 < \beta < 2$. This is consistent with the experimental reaction orders (α = 0.75 and β = 1.21 or 1.44), which supports the validity of the proposed reaction mechanism.

2.2.5 Computational Details

Periodic DFT calculations were performed using the CASTEP code[11] with Vanderbilt-type ultrasoft pseudopotentials[12] and the revised version of Perdew−Burke−Ernzerhof exchange−correlation functional based on the generalized gradient approximation.[13] The plane-wave basis set was truncated at a kinetic energy of 360 eV and a Fermi smearing of 0.1 eV was utilized. Dispersion correlations were considered using the Tkatchenko–Scheffler method with a scaling coefficient of s_R = 0.94 and a damping parameter of d = 20.[14] The reciprocal space was sampled using a *k*-point mesh with a spacing of typically 0.04 $Å^{-1}$, as generated by the Monkhorst−Pack scheme.[15] Spin-porlarization was considered with net-zero charge in all the calculation. Geometry optimization was performed on supercell structures using periodic boundary conditions. The surface was modeled based on Pt(111)–(2×2) and Pt_3In(111)–(1×1) slabs that were four atomic layers thick with 13 Å of vacuum spacing. The convergence criteria for structure optimization and energy calculation were set to (a) an SCF tolerance of 1.0×10^{-6} eV per atom, (b) an energy tolerance of 1.0×10^{-5} eV per atom, (c) a maximum force tolerance of 0.05 eV $Å^{-1}$, and (d) a maximum displacement tolerance of 1.0×10^{-3} Å. The adsorption energy (E_{ad}) was defined as follows: $E_{ad} = E_{A\text{-}S} - (E_S + E_A)$, where $E_{A\text{-}S}$ is the energy of the slab together with the adsorbate, E_A is the total energy of the free adsorbate, and E_S is the total energy of the bare slab.

2.3 Results and discussions

2.3.1 Structure characterization of Pt_3In/TiO_2 catalyst

The catalysts were prepared by a conventional impregnation method using TiO_2 as a catalyst support capable of surface protonics (Pt/TiO_2 and $Pt–In/TiO_2$: Pt 3 wt%). Figure 2.2 shows the high-angle annular dark-field scanning transmission electron microscopy (HAADF-STEM) image of $Pt–In/TiO_2$ and the corresponding elemental map of Pt and In (Figure 2.3 for Ti and O). Small 1–2 nm diameter nanoparticles consisting of Pt and In were highly dispersed over the TiO_2 surface. Quantitative analysis of some Pt–In bimetallic nanoparticles showed a Pt/In atomic ratio of approximately 3 (Figure 2.4). The high-resolution image revealed a specific atomic arrangement with the interplanar distances of 2.03 Å and 2.34 Å and a dihedral angle of 54°, which agreed well with those of intermetallic Pt_3In viewed along the [110] direction.[16] The formation of intermetallic Pt_3In was also indicated by extended X-ray absorption fine structure analysis (XAFS), where Pt–In (In–Pt) scattering was observed in both Pt L_{III}- and In K-edges (Figures 2.5-2.7 and Table 2.1). The XAFS analysis also provided additional information on the electronic state of Pt.

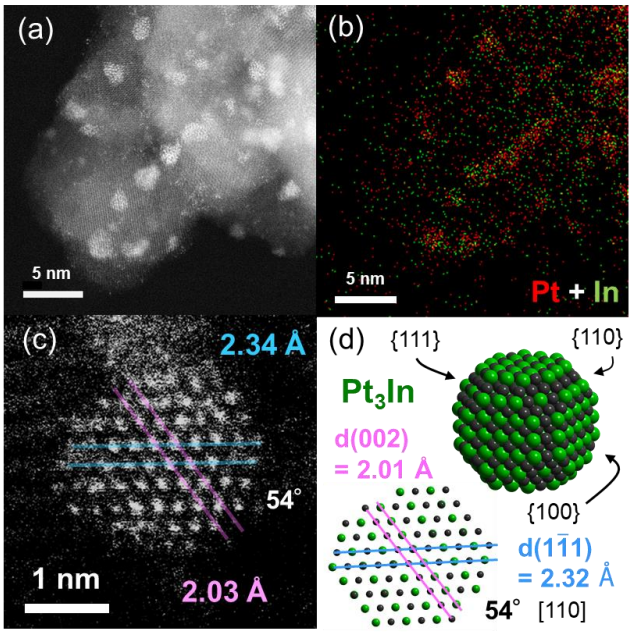

Figure 2.2. (a) HAADF-STEM image of $Pt–In/TiO_2$ and (b) the corresponding elemental map acquired by EDX. (c) High resolution HAADF-STEM image of a single nanoparticle. (d) Model structure of intermetallic Pt_3In viewed along the [110] direction.

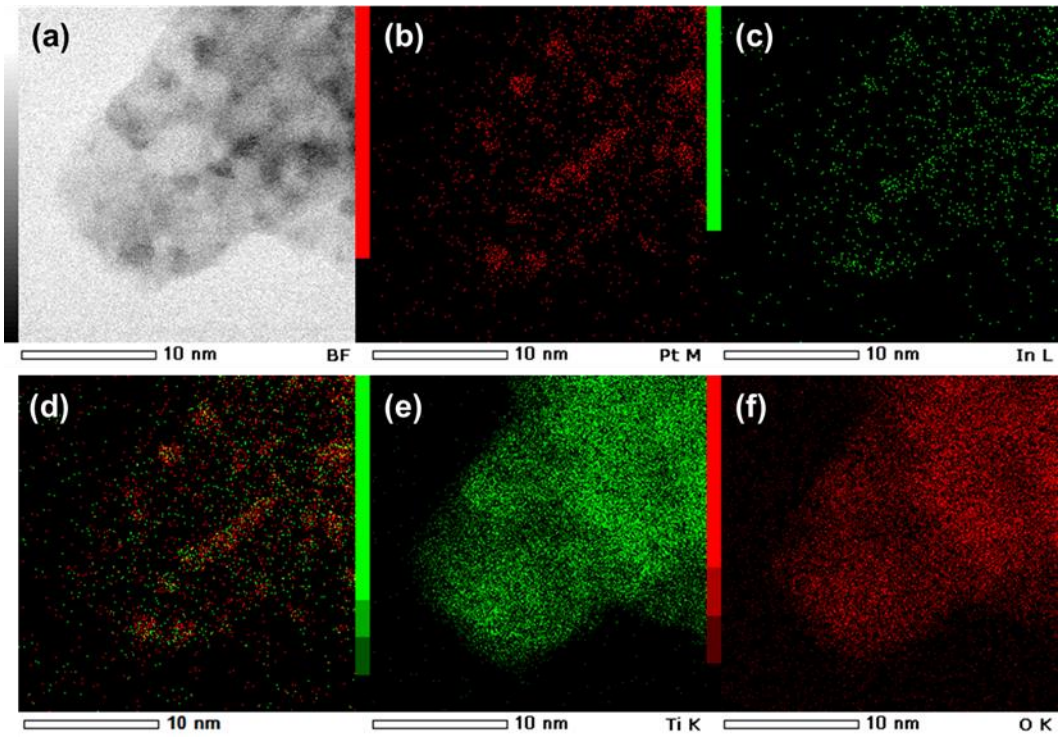

Figure 2.3. (a) ABF-STEM image of Pt–In/TiO_2 and the corresponding element maps of (b) Pt, (c) In, (d) Pt + In overlayer, (e) Ti and (f) O acquired by EDX.

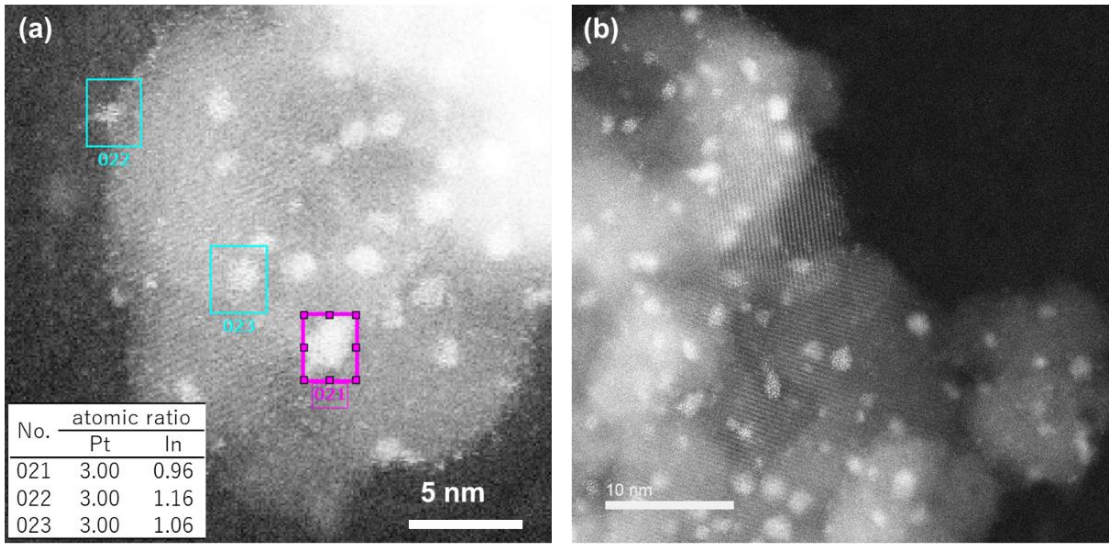

No.	atomic ratio	
	Pt	In
021	3.00	0.96
022	3.00	1.16
023	3.00	1.06

Figure 2.4. (a) Quantitative analysis for the selected nanoparticles. Inset table shows the atomic ratios of Pt and In present in the regions designated by squares. (b) HAADF-STEM image of Pt–In/TiO_2 showing the narrow size distribution (mostly < 2 nm).

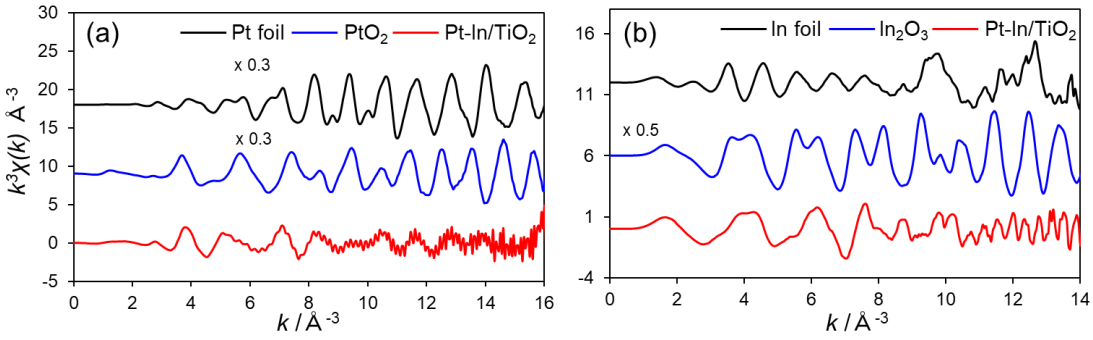

Figure 2.5. (a) Pt L_{III}- and (b) In K-edge EXAFS of Pt–In/TiO_2 and reference compounds.

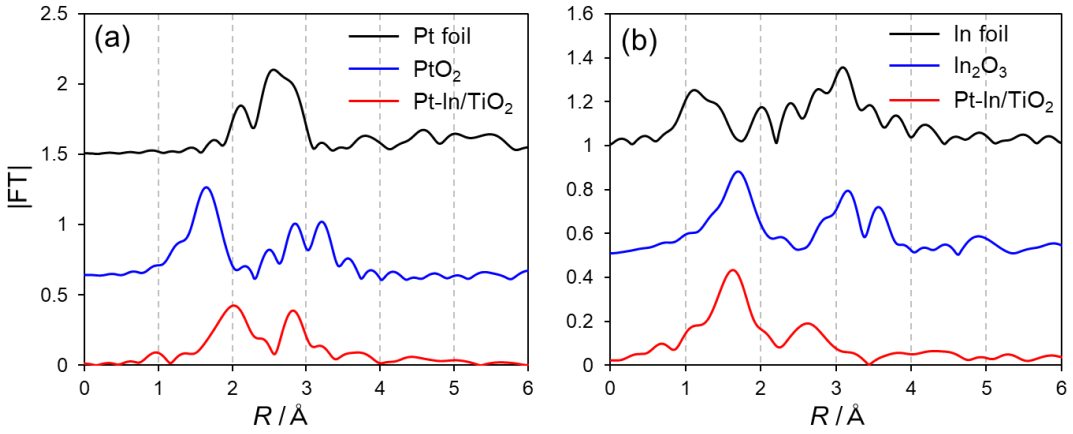

Figure 2.6. (a) Pt L_{III}- and (b) In K-edge FT-EXAFS of Pt–In/TiO_2 and reference compounds.

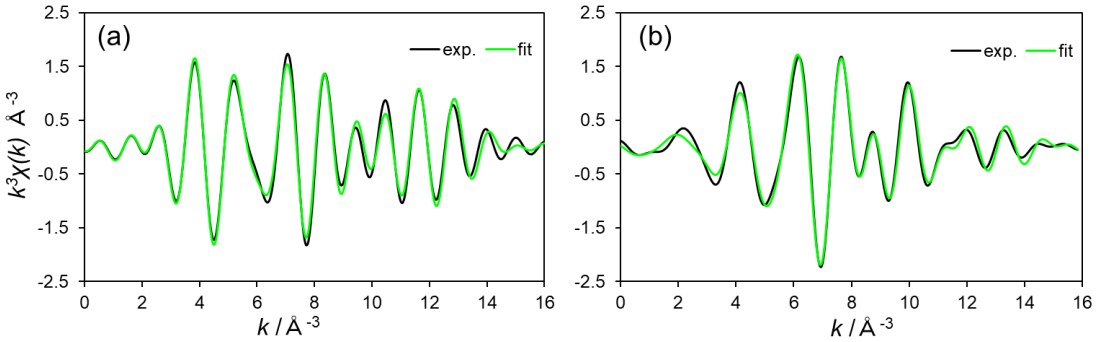

Figure 2.7. Curve-fitting for (a) Pt L_{III}- and (b) In K-edge k^3-weighted EXAFS oscillations of Pt–In/TiO_2.

Table 2.1. Results of EXAFS curve-fitting for Pt–In/TiO_2 and the reference foils

Sample	Edge	Shell	S_o^2 [a]	CN [b]	R (Å) [c]	ΔE_0 (eV) [d]	σ^2 (Å^2) [e]	R-factor
Pt foil	Pt L_{III}	Pt–Pt	0.82	12 (fix)	2.77 ± 0.00	9.0±0.6	0.005	0.002
In foil	In K	In–In	0.86	8 (fix)	3.18 ± 0.01	2.9±0.7	0.024	0.009
		In–In		4 (fix)	3.33 ± 0.04			
Pt–In /TiO_2	Pt L_{III}	Pt–In	0.82 (fix)	2.4 ± 0.5	2.66 ± 0.01	2.0 ± 1.9	0.011	0.020
		Pt–In		0.5 ± 0.4	2.77 ± 0.01		0.011	
		Pt–Pt		6.5 ± 1.3	2.74 ± 0.01		0.011	
		In–O		1.9 ± 0.6	2.06 ± 0.01		0.007	
	In K	In–Pt	0.86 (fix)	3.6 ± 0.8	2.65 ± 0.01	-7.2 ± 2.0	0.011	0.029
		In–Pt		1.1 ± 0.2	2.77 ± 0.01		0.005	

[a] Amplitude factor. [b] Coordination number. [c] Distance between absorber and backscattering atoms. [d] Correction term in the absorption edge. [e] Debye-Waller factor.

As observed in the Pt L_{III} X-ray absorption near edge structure (Figure 2.8), the white line intensity decreased after alloying with In. This suggests that the occupation of the d orbital (electron density of Pt) was increased by In, which is consistent with the trend reported elsewhere.[17] CO pulse chemisorption showed that the Pt dispersion of Pt–In/TiO_2 was 22.7%, which is consistent with that predicted from a cuboctahedron model of a 2–3 nm Pt_3In nanoparticle (23.2%, Figure 2.9).

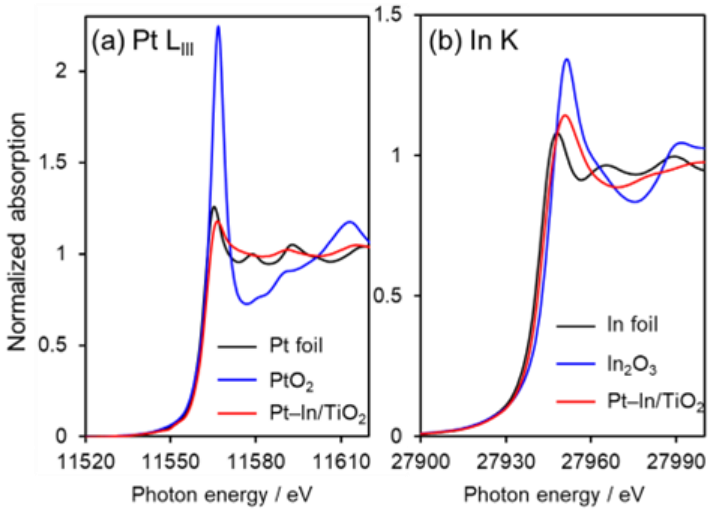

Figure 2.8. (a) Pt L_{III}- and (b) In K-edge XANES spectra of Pt–In/TiO_2 and reference compounds.

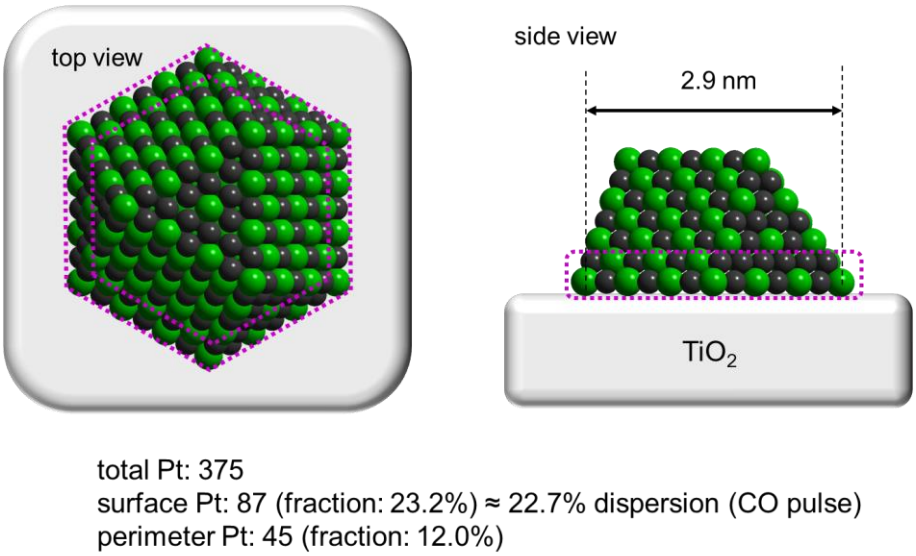

Figure 2.9. A half cuboctahedron model of an intermetallic Pt_3In nanoparticle with (111) and (100) termination. The predicted Pt dispersion of 23.2% is consisted with the experimental Pt TOF measured by CO pulse chemisorption (22.7%).

2.3.2 Electroassisted catalytic PDH performance of Pt_3In/TiO_2

The prepared catalysts were tested in PDH using a fixed-bed continuous flow reactor. Two stainless steel rods as electrodes were placed in contact with the top and bottom of the catalyst bed to impose a direct current to the catalyst (Figure 2.10a, see also Figure 2.1 for details). Before the reaction, the catalyst was pretreated with flowing H_2 at 300°C, so the metal nanoparticles and TiO_2 were reduced. Partial reduction of the TiO_2 support is necessary to pass an electric current to the catalyst bed. Figure 2.10b represents the dependence of the propylene yield on the electric power supplied to the system.

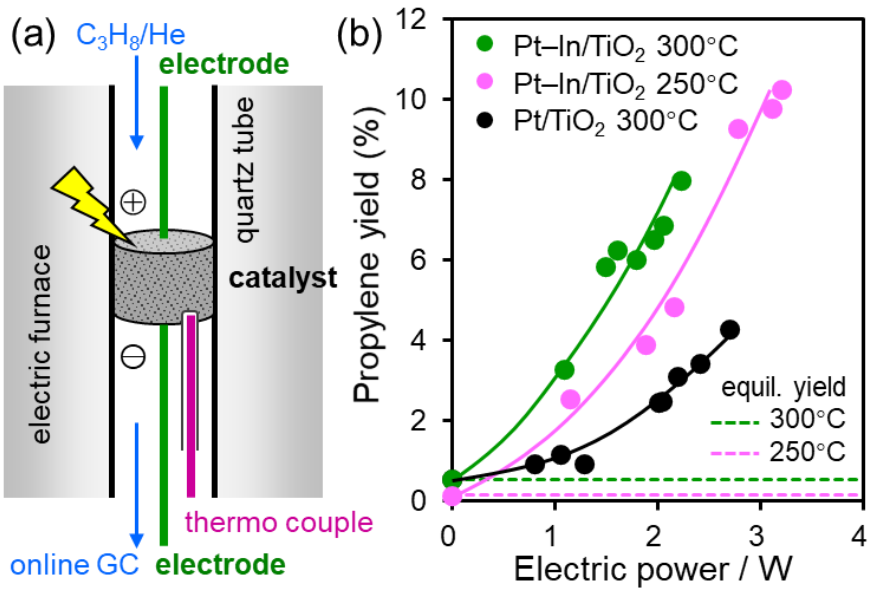

Figure 2.10. (a) Illustration of the reactor setup for electro-assisted PDH. (b) Dependence of propylene yield on the electric power supplied to the catalytic system. Furnace temperature was set to 250°C or 300°C.

The propylene yield was virtually zero when no electricity was supplied due to thermodynamic limitations (0.15% and 0.55% at 250°C and 300°C, respectively; Figure 2.11). The propylene yields increased monotonously with an increase in the supplied electric power, showing a significant dependence on the electric power (carbon balances were mostly 0.95–1.00, Figure 2.12). Interestingly, Pt–In/TiO_2 exhibited remarkably higher propylene yield than Pt/TiO_2 (ca. three times the higher yield per Watt, at 300°C). The reaction still proceeded even at 250°C (voltage and current are shown in Figure 2.13), where the highest propylene yield of 10.2% was achieved using 3.2 W of electric power. The catalyst bed temperature did not increase significantly during energization (typically +2°C–+5°C at a furnace temperature of 250°C, Figure 2.14), indicating that Joule heating made a negligible contribution to catalysis. Thus, two orders of magnitude higher propylene yield than the thermodynamic equilibrium limitation (0.15%) was achieved. To the best of our knowledge, propylene was obtained successfully via PDH at this temperature region for the first time. Moreover, the propylene selectivity was improved: although Pt/TiO_2 showed low selectivity due to the formation of C1 and C2 by-products (59%–79%), Pt–In/TiO_2 gave good selectivity (typically, 84%–99%, Figure 2.15). Thus, the both activity and selectivity were enhanced drastically by alloying Pt with In,

affording an efficient catalyst for low-temperature PDH. In addition, no catalyst deactivation was observed after 120 min of electro-assisted PDH (Figure 2.16).

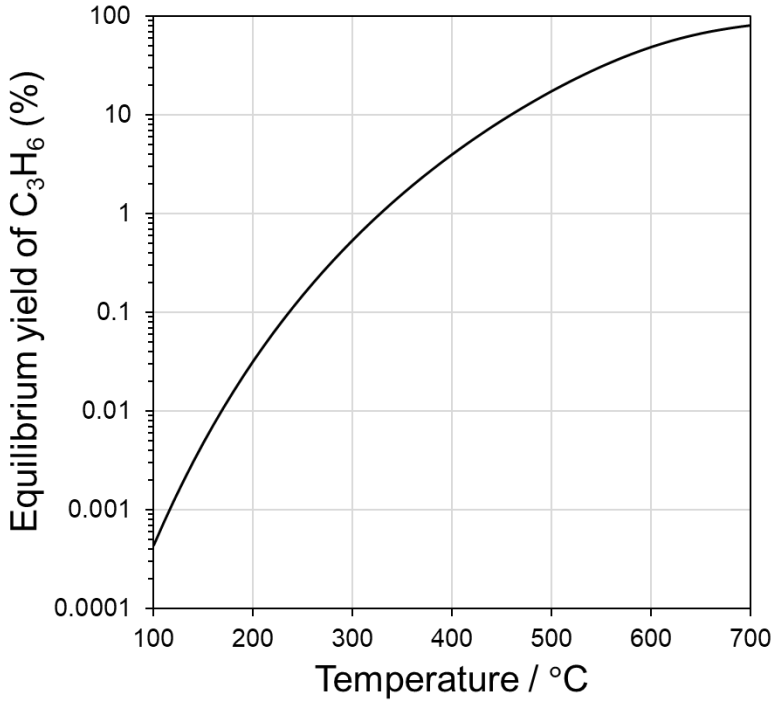

T / °C	yield (%)
200	0.03
250	0.15
300	0.55
350	1.6
400	4.0
450	8.9
460	10.3
500	17.6
550	31.3
600	49.4

Figure 2.11. Temperature dependence of the equilibrium yield of propylene in thermal PDH (C_3H_8:He = 1:1). Calculation was done using HSC Chemistry 8 software.

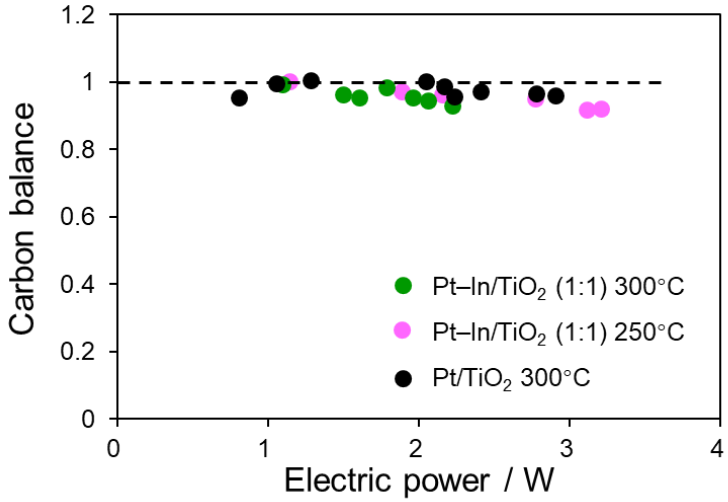

Figure 2.12. Carbon balances for the electro-assisted PDH. Each data point corresponds to that in Figure 2.10b.

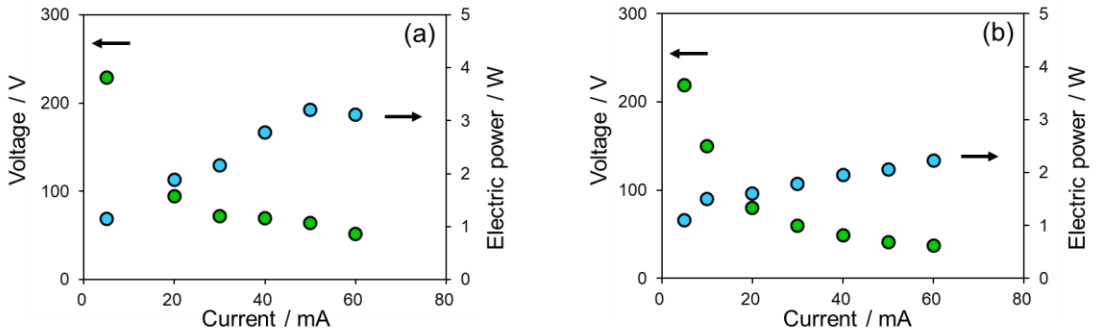

Figure 2.13. The relationship between voltage, current, and electric power for electro-assisted PDH over Pt–In/TiO_2 at (a) 250°C and (b) 300°C.

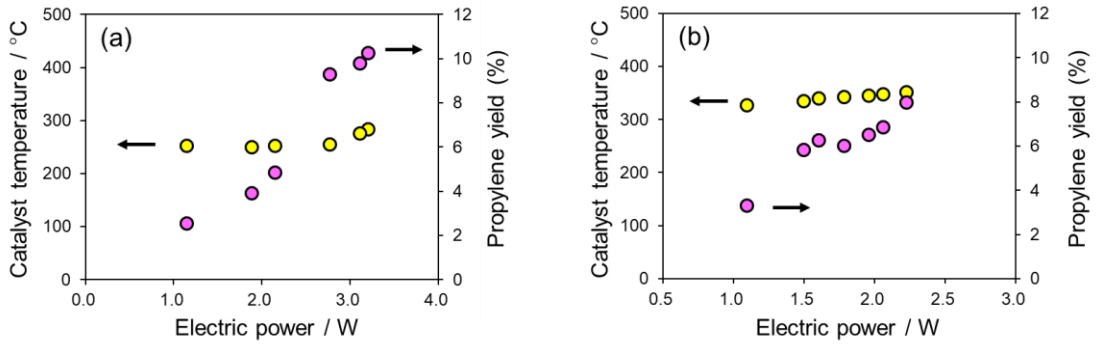

Figure 2.14. Catalyst bed temperature and propylene yield in electro-assisted PDH over Pt–In/TiO_2 at (a) 250°C and (b) 300°C.

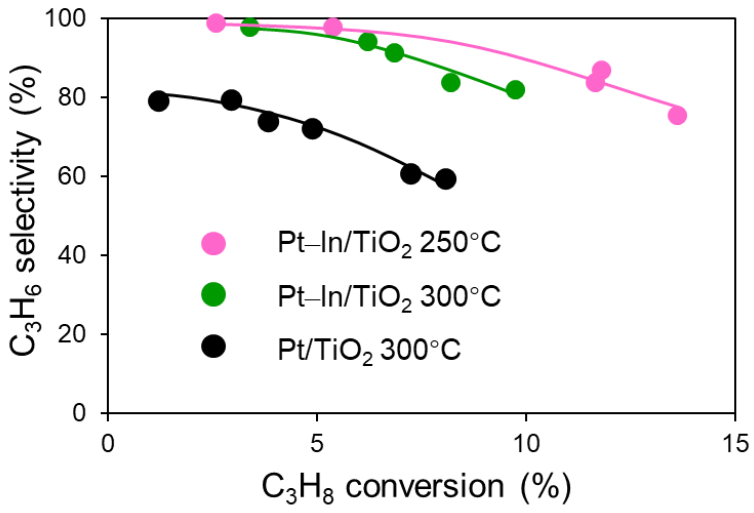

Figure 2.15. Conversion–selectivity curves for electro-assisted PDH over Pt–In/TiO_2 and Pt/TiO_2.

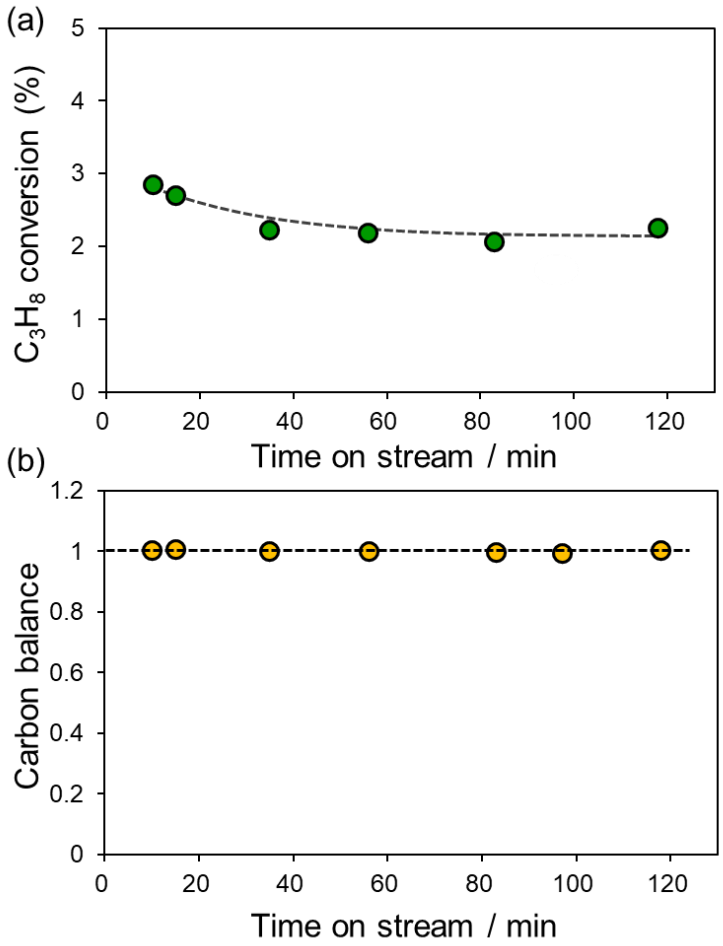

Figure 2.16. Time course of (a) C_3H_8 conversion and (b) carbon balance in electro-assisted PDH over Pt–In/TiO_2 (T = 300°C, I = 20 mA).

2.3.3 Kinetic analysis and proposed reaction mechanism

Next, kinetic studies were performed to understand the reaction mechanism of electro-assisted PDH on Pt–In/TiO_2. The dependency of the reaction rate on the partial pressure of propane ($P_{C_3H_8}$) and electric power (E_p) at 300°C were 0.75 and 1.21, respectively (Figure 2.17). The dependency on E_p increased to 1.44 at 250°C. The reaction order for E_p was higher than unity, suggesting that more than one elementary step is promoted by electricity. Figure 2.18 shows the Eyring plots of thermal and electro-assisted PDH using Pt–In/TiO_2.

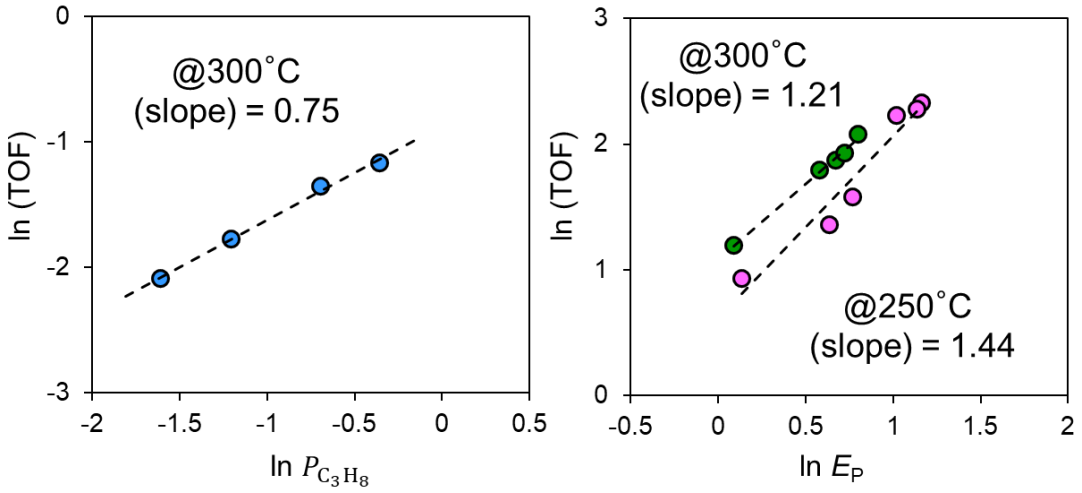

Figure 2.17. Reaction orders of $P_{C_3H_8}$ (T = 300°C, I = 20 mA) and E_P (T = 250°C or 300°C, I = 5–60 mA) in electro-assisted PDH over Pt–In/TiO_2.

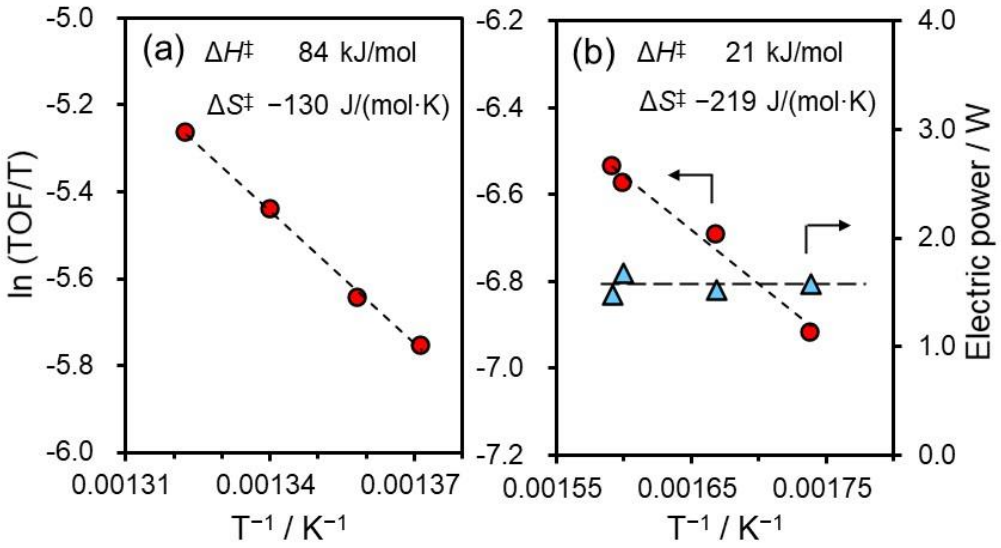

Figure 2.18. Eyring plots for (a) thermal and (b) electro-assisted PDH over Pt–In/TiO_2.

In the absence of electricity, the obtained $\Delta H^{\ddagger}$ and $\Delta S^{\ddagger}$ were similar to those obtained for in thermal PDH using Pt-based catalysts.[18, 19] On the other hand, both $\Delta H^{\ddagger}$ and $\Delta S^{\ddagger}$ decreased drastically when a current was applied. Here, the electric power was adjusted to be almost constant at each temperature to exclude its effects on the reaction rate. The significant decrease in $\Delta S^{\ddagger}$ suggests that the rate-determining step (RDS) was changed to a less entropic pathway. Considering that proton hopping is a crucial step of surface protonics, changing from C–H scission of propane (dissociative, generally the RDS of PDH) to proton collision to propane

(associative) is most likely. The quite low $\Delta H^{\ddagger}$ value (21 kJ mol^{-1}) indicates that the proton hopping/collision process is electrically biased by the external electric field (Figure 2.19). Similar low values of apparent activation energies were also reported in electrochemistry[20, 21] and other electro-assisted catalysis.[22-24] Thus, electro-assisted PDH provides a novel reaction pathway with much lower activation barrier. The electrically biased proton also provides free energy gain to the initial state of the PDH, which decreases the overall ΔG and increase the equilibrium propane conversion (Figure 2.19). The kinetic isotope effect (KIE) was next examined to obtain further information on the reaction mechanism. For thermal PDH, a normal KIE (k_H/k_D = 1.95) was observed when fully deuterated propane (C_3D_8) was used as the reactant, demonstrating that the C–H scission of propane is the RDS. Surprisingly, inverse KIE values were reproducibly obtained when a current was applied (k_H/k_D = 0.69–0.81, Table 2.2), indicating that the C–H scission is not the RDS. A possible interpretation of the inverse KIE is the involvement of a nonlinear three-center transition state, in which new bond formation occurs simultaneously with the old bond scission.[25] This is because a three-center transition state has a larger coupling constant of vibration than the initial physisorbed state;[26, 27] therefore, the zero-pint energy (ZPE) difference between H and D species becomes larger (Figure 2.20) at the transition state than at the initial state. Here, the ZPE at the initial and transition states are described by eqs. (1) and (2), respectively.[27]

$$E_0{}^{\mathrm{H(D)}} = \frac{h}{4\pi}\sqrt{\frac{k_0}{\mu_{\mathrm{H(D)}}}} \qquad (1)$$

$$E^{\ddagger\mathrm{H(D)}} = \frac{h}{4\pi}\sqrt{\frac{k^{\ddagger}}{\mu_{\mathrm{H(D)}}}} \qquad (2)$$

where, h, k, and μ indicate the Planck constant, coupling constant of vibration, and reduced mass, respectively. The ZPE difference between H and D species for the initial and transition states can be expressed by eqs. (3) and (4), respectively:

$$\Delta {E_0}^{\mathrm{H-D}} = {E_0}^{\mathrm{H}} - {E_0}^{\mathrm{D}} = \frac{h}{4\pi}\left(\sqrt{\frac{1}{\mu_{\mathrm{H}}}} - \sqrt{\frac{1}{\mu_{\mathrm{D}}}}\right)\sqrt{k_0} \qquad (3)$$

$$\Delta {E^{\ddagger}}^{\mathrm{H-D}} = {E^{\ddagger}}^{\mathrm{H}} - {E^{\ddagger}}^{\mathrm{D}} = \frac{h}{4\pi}\left(\sqrt{\frac{1}{\mu_{\mathrm{H}}}} - \sqrt{\frac{1}{\mu_{\mathrm{D}}}}\right)\sqrt{k^{\ddagger}} \qquad (4)$$

Considering that the coupling constant of vibration of a three-center transition state is larger than that of the initial physisorbed state, the following relationship is obtained (eq. 5):

$$\Delta {E^{\ddagger}}^{\mathrm{H-D}} > \Delta {E_0}^{\mathrm{H-D}} \qquad (\sqrt{k^{\ddagger}} > \sqrt{k_0}) \qquad (5)$$

Therefore, the energy barrier of D collision should be lower than that of H collision as follows (eq. 6):

$${E_{\mathrm{a}}}^{\mathrm{H}} - {E_{\mathrm{a}}}^{\mathrm{D}} = {E^{\ddagger}}^{\mathrm{H}} - {E_0}^{\mathrm{H}} - \left({E^{\ddagger}}^{\mathrm{D}} - {E_0}^{\mathrm{D}}\right) = \Delta {E^{\ddagger}}^{\mathrm{H-D}} - \Delta {E_0}^{\mathrm{H-D}} > 0 \qquad (6)$$

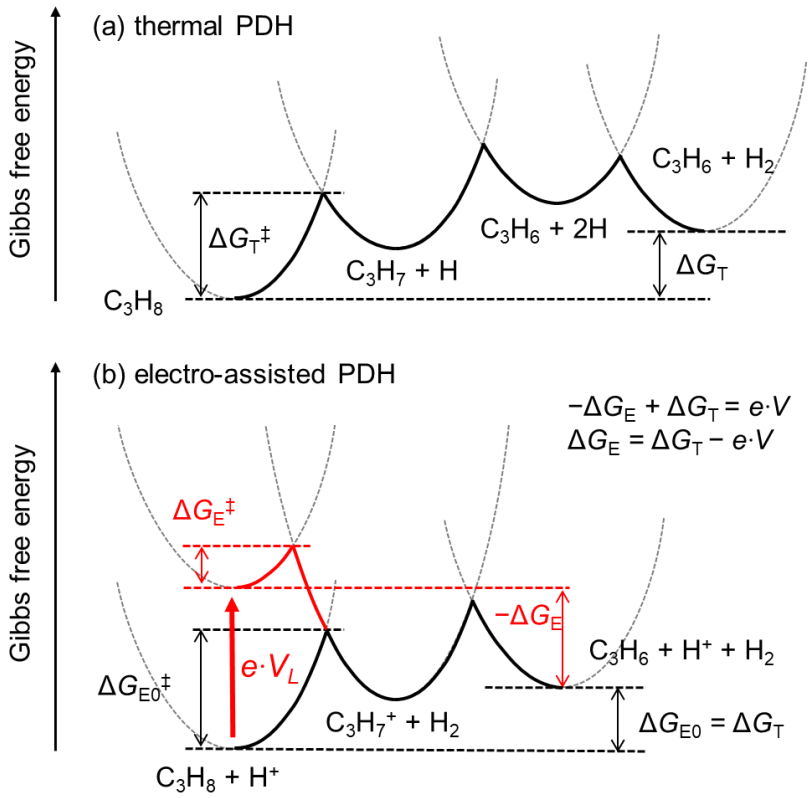

Figure 2.19. Schematic illustration of the free energy diagrams of (a) thermal and (b) electro-assisted PDH. Subscript T, E0, and E indicate the reaction pathways of thermal PDH via C–H scission, thermal PDH via proton collision, and electro-assisted PDH via proton collision, respectively. V_L, e, and their product indicate the local electric field gradient, elemental charge, and free energy gain by the external electric field, respectively. The equilibrium constant and propane conversion become much larger due to the decrease in ΔG.

Table 2.2. Kinetic isotope effects on propane dehydrogenation with and without electric filed.

electric power / W	reactant	T / °C	r / $\mu mols^{-1}g_{cat}^{-1}$	k_H/k_D
0 (thermal)	C_3H_8	447	1.88	1.95
0 (thermal)	C_3D_8	449	0.96	
2.00	C_3H_8	312	2.21	0.69
2.02	C_3D_8	313	3.21	
1.96	C_3H_8	302	1.60	0.79
1.95	C_3D_8	310	2.03	
1.66	C_3H_8	315	2.19	0.81
1.40	C_3D_8	319	2.69	

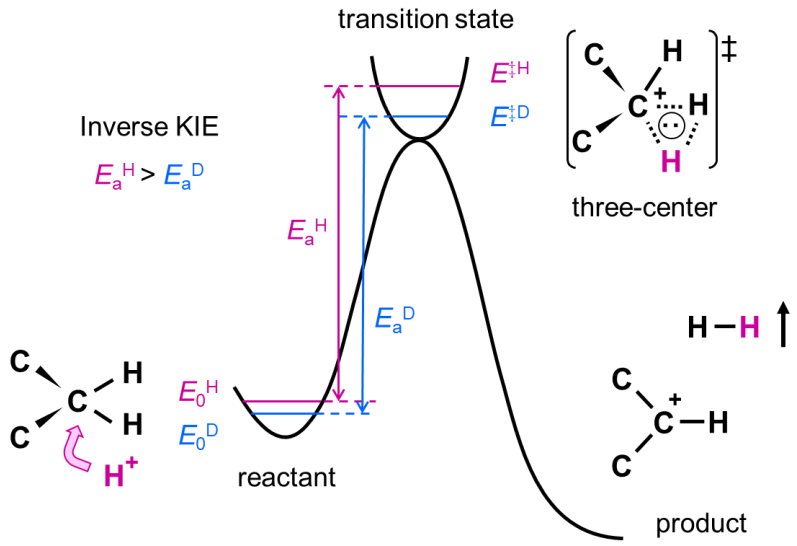

Figure 2.20. Possible interpretation for the potential energy profiles yielding inverse KIE.

Thus, the three-center transition state mechanism can explain the inverse KIE and is consistent with the proton collision pathway. Indeed, a previous study on quantum chemical analysis for H^+ attack on C_3H_8 reported inverse KIE values.[22-28] Based on these results, it is believed that proton collision to propane that involves a three-center transition state is the RDS of the electro-assisted PDH over Pt–In/TiO_2. Kinetic analysis was also conducted using the experimental reaction orders and the following reaction scheme of the electro-assisted PDH:

$$H^+ \cdot \sigma_0 \rightleftharpoons H^+ \cdot \sigma_i \quad (7)$$

$$C_3H_8 + \sigma_m \rightleftharpoons C_3H_8 \cdot \sigma_m \quad (8)$$

$$C_3H_8 \cdot \sigma_m + H^+ \cdot \sigma_i \rightarrow {C_3H_7}^+ \cdot \sigma_m + H_2 + \sigma_i \quad (9)$$

$${C_3H_7}^+ \cdot \sigma_m + \sigma_i \rightleftharpoons C_3H_6 \cdot \sigma_m + H^+ \cdot \sigma_i \quad (10)$$

$$C_3H_6 \cdot \sigma_m \rightleftharpoons C_3H_6 + \sigma_m \quad (11)$$

where, σ_0, σ_i, and σ_m indicate a proton acceptor on the surface (excess), proton acceptor at the metal-support interface, and metallic adsorption site, respectively. These equations represent the following: (7) proton hopping, (8) propane physisorption, (9) proton collision to propane, (10) propylene formation (deprotonation), and (11) propylene desorption, respectively. In step (9), a three-center transition state, such as C···H_2, is assumed (Figure 2.20). Here, steps

(7), (9), and (10) could be facilitated by an electric field because cationic species are involved. We solved the rate equation of step (9) as the RDS by applying quasi-stationary approximation and site conservation condition as follows (see Section 2.2.4 for details):

$$r = \frac{k_3 K_1 K_2 C_0 P_{C_3H_8} E_p}{1 + K_2 P_{C_3H_8} + K_5^{-1} P_{C_3H_6} + \frac{K_4^{-1} K_5^{-1} P_{C_3H_6}}{(K_1^{-1} C_0^{-1} - 1) E_p}} \qquad (12)$$

where, k_i, K_i, and C_0 are the rate and equilibrium constants of step i, and surface proton density, respectively. This rate equation can be simplified into the following form using some approximations:

$$r = k P_{C_3H_8}{}^{\alpha} E_p{}^{\beta} \qquad (13)$$

where, the lower/higher limits of α and β are 0/1 and 1/2, respectively (see Section 2.2.4 for derivation). Thus, the possible reaction order ranges can be obtained as follows:

$$\therefore \quad 0 < \alpha < 1\,,\ 1 < \beta < 2 \qquad (14)$$

which are fully consistent with the experimental orders (α = 0.75 and β = 1.21 or 1.44). The good agreement between the theoretical and experimental reaction orders supports the validity of the proposed reaction mechanism. Figure 2.21 presents a summary of the reaction mechanism.

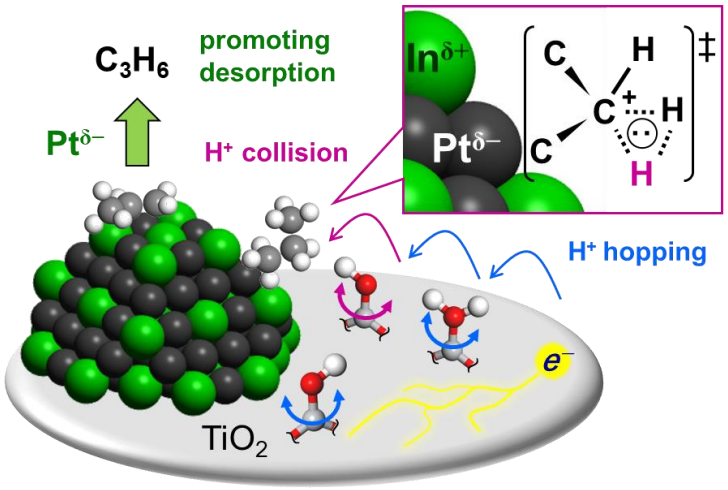

Figure 2.21. Proposed reaction mechanism of electro-assisted PDH over Pt–In/TiO_2.

Under an electric field, H^+ hopping is facilitated by the Grotthuss mechanism and H^+ collisions with propane allow its activation via a three-center transition state to generate $C_3H_7^+$ and H_2. Here, alloying of Pt with In promotes this process, probably because the electron-enriched Pt stabilizes the cationic transition state and $C_3H_7^+$ intermediate. The $C_3H_7^+$ intermediate is then converted to C_3H_6 and recover H^+. The electron-enriched Pt can also enhance propylene desorption because of the weaker adsorption, which decreases the probability of propylene decomposition and increases its selectivity. Indeed, our DFT calculation revealed that the adsorption energy of C_3H_6 on Pt(111) and Pt_3In(111) were −102.0 kJ mol^{-1} and −58.1 kJ mol^{-1}, respectively (Figure 2.22), which strongly supports the enhanced desorption of propylene on Pt–In/TiO_2. In this context, the propylene selectivity might be further improved by using more In-rich intermetallic phases to promote propylene desorption. Thus, Pt–In/TiO_2 works as an efficient catalyst for electro-assisted PDH at low temperatures.

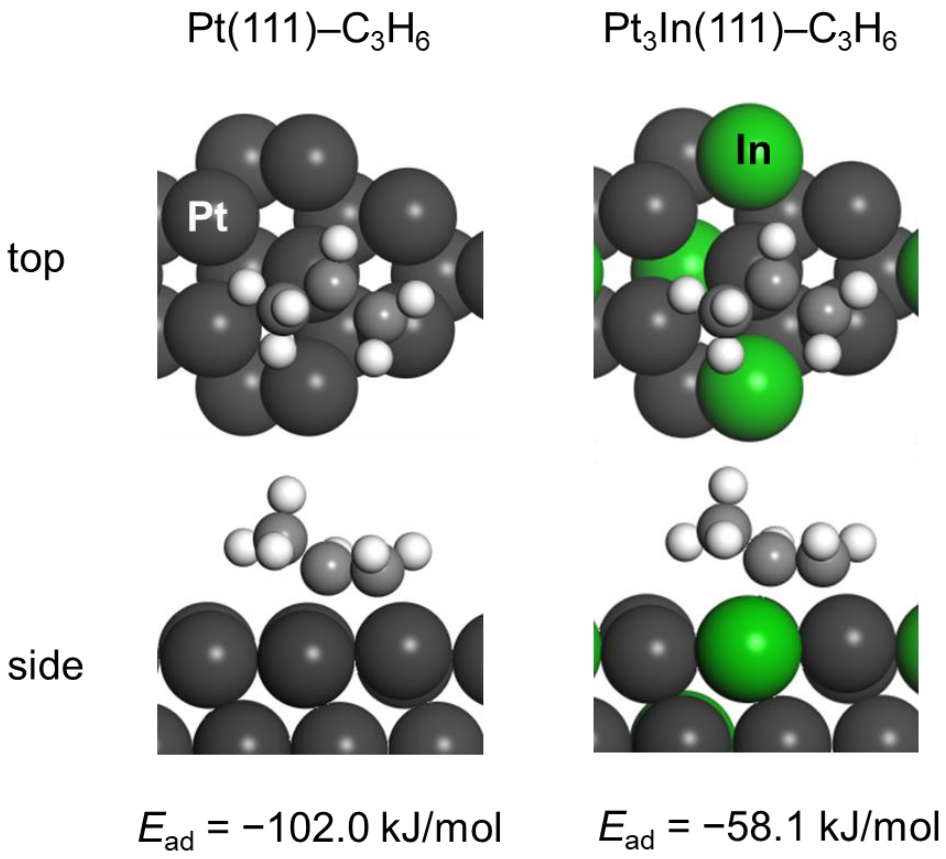

Figure 2.22. Optimized structures and adsorption energy (E_{ad}) of C_3H_6 adsorbed on Pt(111) and $Pt_3In(111)$ surfaces with di-σ configuration.

2.3.4 Energy efficiency of electroassisted PDH

Finally, the energy efficiency of this catalytic system was evaluated and compared with that of the thermal reaction. For a propylene yield of 10.2% at 250°C, the estimated enthalpy gain from the endothermic propylene production (ΔH = +127.5 kJ mol^{-1}) was 0.090 J s^{-1} (W), which corresponds to a 2.8% energy efficiency for the supplied electric power of 3.2 W. Although there is room for improvement, this efficiency may be much greater than that in thermal reactions because a much higher temperature is needed to obtain comparable propylene yields (e.g., 460°C for a 10.3% yield). For example, in the present case, 22 W of additional energy is required to heat the electric furnace from 250°C to 460°C (Figure 2.23). Although this is a specific case and the efficiency differs according to the individual experimental setup, these results suggest that the electro-assisted PDH has much greater energy efficiency than the thermal reactions.

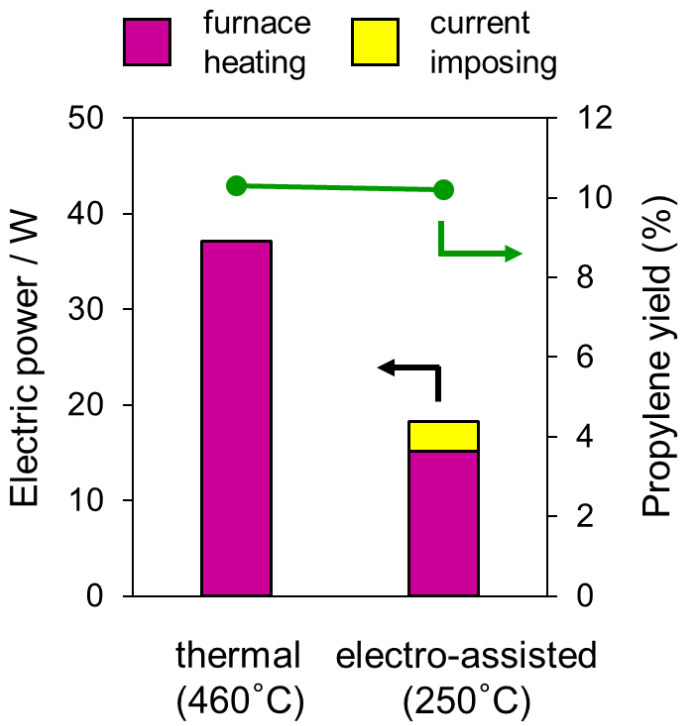

Figure 2.23. Total electric power needed to obtain ~10% yield of propylene in thermal and electro-assisted PDH over Pt–In/TiO_2. An electric tubular furnace (ARF-16KC; Asahi Rika Co. Ltd., electric capacity: 300 W) was used for heating.

2.4 Conclusion

In summary, a novel type of catalytic system was developed for PDH by a combination of a surface protonics methodology and active site modification based on intermetallics. With the aid of 3.2 W electric power, Pt–In/TiO_2 afforded a 10.2% propylene yield at 250°C for the first time, where the thermodynamic equilibrium yield was only 0.15%. Alloying of Pt with In drastically modified the electronic state of Pt, which enhanced both the catalytic activity and selectivity. Overall, this study opens a new horizon for the catalysis of PDH.

References

1. Wang, G.; Zhu, X.; Li, C., Recent Progress in Commercial and Novel Catalysts for Catalytic Dehydrogenation of Light Alkanes. *Chem. Rec.* **2020,** *20*, 604-616.

2. Chen, S.; Chang, X.; Sun, G.; Zhang, T.; Xu, Y.; Wang, Y.; Pei, C.; Gong, J., Propane dehydrogenation: catalyst development, new chemistry, and emerging technologies. *Chem. Soc. Rev.* **2021,** *50*, 3315-3354.

3. Sattler, J. J.; Ruiz-Martinez, J.; Santillan-Jimenez, E.; Weckhuysen, B. M., Catalytic dehydrogenation of light alkanes on metals and metal oxides. *Chem. Rev.* **2014,** *114*, 10613-53.

4. Torimoto, M.; Murakami, K.; Sekine, Y., Low-Temperature Heterogeneous Catalytic Reaction by Surface Protonics. *Bull. Chem. Soc. Jpn.* **2019,** *92*, 1785-1792.

5. Manabe, R.; Okada, S.; Inagaki, R.; Oshima, K.; Ogo, S.; Sekine, Y., Surface Protonics Promotes Catalysis. *Sci. Rep.* **2016,** *6*, 1-7.

6. Oshima, K.; Shinagawa, T.; Sekine, Y., Methane Conversion Assisted by Plasma or Electric Field. *J. Jpn. Pet. Inst.* **2013**, *56*, 11-21.

7. Yabe, T.; Yamada, K.; Murakami, K.; Toko, K.; Ito, K.; Higo, T.; Ogo, S.; Sekine, Y., Role of Electric Field and Surface Protonics on Low-Temperature Catalytic Dry Reforming of Methane. *ACS Sustainable Chem. Eng.* **2019,** *7*, 5690-5697.

8. Yabe, T.; Mitarai, K.; Oshima, K.; Ogo, S.; Sekine, Y., Low-temperature dry reforming of methane to produce syngas in an electric field over La-doped Ni/ZrO_2 catalysts. *Fuel Process. Technol.* **2017,** *158*, 96-103.

9. Ravel, B.; Newville, M., ATHENA, ARTEMIS, HEPHAESTUS: data analysis for X-ray absorption spectroscopy using IFEFFIT. *J. Synchrotron Radiat.* **2005,** *12*, 537-41.

10. Ankudinov, A. L.; Ravel, B.; Rehr, J. J.; Conradson, S. D., Real-space multiple-scattering calculation and interpretation of x-ray-absorption near-edge structure. *Phys. Rev. B: Condens. Matter* **1998,** *58*, 7565-7576.

11. Segall, M. D.; Philip, J. D. L.; Probert, M. J.; Pickard, C. J.; Hasnip, P. J.; Clark, S. J.; Payne, M. C., First-principles simulation: ideas, illustrations and the CASTEP code. *J. Phys.: Condens. Matter* **2002,** *14*, 2717-2744.

12. Vanderbilt, D., Soft self-consistent pseudopotentials in a generalized eigenvalue formalism.

Phys. Rev. B **1990,** *41*, 7892.

13. Perdew, J. P.; Burke, K.; Ernzerhof, M., Generalized Gradient Approximation Made Simple. *Phys. Rev. Lett.* **1996,** *77*, 3865-3868.

14. Tkatchenko, A.; Scheffler, M., Accurate molecular van der Waals interactions from ground-state electron density and free-atom reference data. *Phys. Rev. Lett.* **2009,** *102*, 1-4.

15. Monkhorst, H. J.; Pack, J. D., Special points for Brillouin-zone integrations. *Phys. Rev. B* **1976,** *13*, 5188-5192.

16. Lin, C. F.; Mohney, S. E.; Chang, Y. A., Phase-Equilibria in the Pt-in-P System. *J. Appl. Phys.* **1993,** *74*, 4398-4402.

17. Zakharova, E. Y.; Andreeva, N. A.; Kazakov, S. M.; Kuznetsov, A. N., Ternary arsenides based on platinum-indium and palladium-indium fragments of the Cu_3Au-type: Crystal structures and chemical bonding. *J. Alloys Compd.* **2015,** *621*, 307-313.

18. Zhang, W.; Wang, H. Z.; Jiang, J. W.; Sui, Z. J.; Zhu, Y. A.; Chen, D.; Zhou, X. G., Size Dependence of Pt Catalysts for Propane Dehydrogenation: from Atomically Dispersed to Nanoparticles. *ACS Catal.* **2020,** *10*, 12932-12942.

19. Escorcia, N. J.; LiBretto, N. J.; Miller, J. T.; Li, C. W., Colloidal Synthesis of Well-Defined Bimetallic Nanoparticles for Nonoxidative Alkane Dehydrogenation. *ACS Catal.* **2020,** *10*, 9813-9823.

20. Zhou, M.; Weng, Q.; Zhang, X.; Wang, X.; Xue, Y.; Zeng, X.; Bando, Y.; Golberg, D., In situ electrochemical formation of core–shell nickel–iron disulfide and oxyhydroxide heterostructured catalysts for a stable oxygen evolution reaction and the associated mechanisms. *J. Mater. Chem. A* **2017,** *5*, 4335-4342.

21. Madram, A. R.; Asadi, S., Kinetics of the hydrogen evolution reaction on a highly porous three-dimensional Ni catalyst in the presence of a Mo ion activator in alkaline solution. *New J. Chem.* **2017,** *41*, 3344-3351.

22. Gondo, A.; Manabe, R.; Sakai, R.; Murakami, K.; Yabe, T.; Ogo, S.; Ikeda, M.; Tsuneki, H.; Sekine, Y., Ammonia Synthesis Over Co Catalyst in an Electric Field. *Catal. Lett.* **2018,** *148*, 1929-1938.

23. Takise, K.; Sato, A.; Murakami, K.; Ogo, S.; Seo, J. G.; Imagawa, K.-i.; Kado, S.; Sekine, Y., Irreversible catalytic methylcyclohexane dehydrogenation by surface protonics

at low temperature. *RSC Adv.* **2019,** *9*, 5918-5924.

24. Takise, K.; Sato, A.; Muraguchi, K.; Ogo, S.; Sekine, Y., Steam reforming of aromatic hydrocarbon at low temperature in electric field. *Appl. Catal., A* **2019,** *573*, 56-63.

25. Wiberg, K. B., The deuterium isotope effect. *Chem. Rev.* **1955,** *55*, 713-743.

26. Kurylo, M. J.; Hollinden, G. A.; Timmons, R. B., ESR Study of the Kinetic Isotope Effect in the Reaction of H and D Atoms with CH_4. *The J. of Chem. Phy.* **1970,** *52*, 1773-1781.

27. Okada, S.; Manabe, R.; Inagaki, R.; Ogo, S.; Sekine, Y., Methane dissociative adsorption in catalytic steam reforming of methane over Pd/CeO_2 in an electric field. *Catal. Today* **2018,** *307*, 272-276.

28. Kerkeni, B.; Clary, D. C., Quantum reactive scattering of H^+ hydrocarbon reactions. *Phys. Chem. Chem. Phys.* **2006,** *8*, 917-925.

Chapter 3

Surface Engineering of Titania Boosts Electroassisted Propane Dehydrogenation at Low Temperature

3. Surface Engineering of Titania Boosts Electroassisted Propane Dehydrogenation at Low Temperature

3.1 Introduction

Propylene is one of the most important feedstocks to produce chemicals and plastic products in the global chemical industry, and the propylene gap between the world demand and supply is gradually increasing.[1-3] Therefore, on-purpose propylene production technologies such as propane dehydrogenation (PDH) are of great interest to the petrochemical marketplace.[1] Owing to the highly endothermic properties of PDH reactions, a temperature range of 550°C to 600°C is required to gain sufficient equilibrium yield. However, the required high-temperature system for sufficient propane conversion is expensive and energy consuming. Moreover, under such high temperatures, side reactions and deactivation by coking and metal sintering occur, severely hindering practical utilization.[1-3] Therefore, developing a catalytic system for PDH that works at a lower temperature region is highly attractive.

One of the promising approaches for such low-temperature conversion is electroassisted catalysis based on surface protonics. Imposing a direct current to a catalyst allows high conversion at low temperatures by gaining external free energy electricity.[4] In this system, surface protons migrate on the oxide support by the Grotthuss mechanism and attack the reactant molecule at the metal-support interface which allows the convertion of robust molecules such as methane (CH_4),[5-7] nitrogen (N_2),[8-10] and carbon dioxide (CO_2)[11] at low temperatures. Applying electric field catalysis can also be a promising way to break the thermodynamic equilibrium limitation of propane conversion at low temperatures. In this reaction system, the overall reaction rate of propylene formation is mainly determined by three factors: (1) the number (concentration) of surface protons, (2) the transition state stability at proton collision, and (3) the selectivity to propylene desorption or decomposition. First, the number of surface protons, which is the density of surface hydroxyl groups, is the key factor that directly determines overall reaction rate. Surface hydroxyl groups can be enriched by doping a heterocation on the support oxide surface region by charge compensation (Scheme 3.1).[12-14] For other factors, electron-enriched active sites are able to stabilize the cationic transition state formed by proton collision while diluting the active metal ensemble by alloying

with an inert metal to increase selectivity to propylene.[15-17] Indeed, we recently demonstrated that alloying Pt with In to form intermetallic Pt_3In effectively satisfies requirements (2) and (3) (Scheme 3.1).[15, 18] As a result, the combination of the two modifications is expected to boost the potential ability for electroassisted PDH at low temperatures.

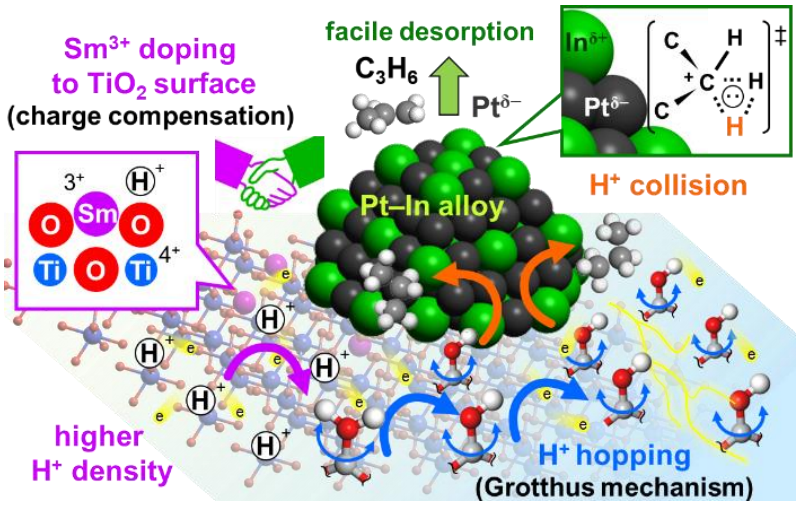

Scheme 3.1. The catalyst design for enhancing electroassisted PDH at low temperatures. Sm^{3+} is doped into TiO_2 surface to increase the number of surface protons by charge compensation. Pt–In alloy is used for selective formation of propylene and to enhance the proton collision with propane.

In this study, we discovered that doping Sm^{3+} into the surface of anatase TiO_2, which is a common oxide support suitable for surface protonics,[5, 19] successfully increased the concentration of surface hydroxyl groups of TiO_2 by charge compensation. Moreover, the promotional effect of this surface engineering of TiO_2 and the active site modification based on Pt–In alloying could be synergized to combine factors (1) – (3) (Scheme 3.1), thereby enabling a drastic enhancement in the catalytic activity in electroassisted propane dehydrogenation at 300°C. The hybrid catalyst, Pt–In/Sm–TiO_2, afforded the highest propylene yield of 19.3% at 300°C of furnace temperatrue, where the thermodynamic equilibrium yield is only 0.5%. Herein, we report not only a highly efficient propylene production system working at low temperatures, but also an advanced and universal strategy for improving the catalytic performance of electric field catalysis.

3.2 Experimental section

3.2.1 Catalysts preparation

Sm-doped TiO_2 (Sm–TiO_2) was prepared by a hydrothermal (TH) method using anatase TiO_2 as a core. First, 3.0 g of TiO_2 powder (JRC-TIO-7, Sakai Chemical Industry Co. Ltd., anatase, SBET = 120 m^2g^{-1}) was dispersed in 30 mL of ethanol. Then, 144 mg of HNO_3 (Fujifilm Wako Pure Chemical, 69 wt%) was added to the mixture, followed by adding of an appropriate amount of $Ti[OCH(CH_3)_2]_4$ (Sigma-Aldrich, ≥ 97%) and $Sm(NO_3)_3 \cdot 6H_2O$ (Fujifilm Wako Pure Chemical, 99.5%) so that the molar ratio of $Sm(NO_3)_3 \cdot 6H_2O$, $Ti[OCH(CH_3)_2]_4$, and TiO_2 was 1.0 : 9.0 : 90. The suspension was sealed by a plastic film and vigorously stirred for 3 hours. Then, 1 mL of ion-exchanged water was added dropwise into the mixture. After stirring for another 30 minutes, the suspension was transferred into an autoclave (50 mL) and maintained at 200°C for 24 hours. The hydrothermally treated mixture was then centrifuged for powder separation, washed several times with ion-exchanged water, and dried overnight at 90°C. Finally, Sm-doped TiO_2 was obtained by calcination at 500°C for 1 hour. For Sm–TiO_2 with different amounts of Sm, the Sm content of the whole Ti was adjusted to 0.5%, 0.75%, 1%, 1.5%, and 2% while keeping the molar ratio of $Ti[OCH(CH_3)_2]_4$ and TiO_2 at 1 : 10.

Sm-loaded TiO_2 (Sm/TiO_2) was prepared by a conventional impregnation method. First, 1.0 g of TiO_2 that was prepared in a similar manner mentioned above without $Sm(NO_3)_3 \cdot 6H_2O$ was added to a vigorously stirred aqueous solution (50 mL) containing $Sm(NO_3)_3 \cdot 6H_2O$ (the atomic ratio of Sm/Ti was 1.0 %) followed by stirring for 3 hours. The mixture was dried under reduced pressure at 50°C, followed by calcination at 500°C for 1 hour.

The Pt–In/TiO_2, Pt–In/Sm–TiO_2 and Pt–In/Sm/TiO_2 catalysts were prepared by a co-impregnation method using an excess amount of water (ca. 50 mL of ion-exchanged water per gram support) while the support was prepared using the HT method. For Pt–In/TiO_2, the prepared TiO_2 support using the HT method without $Sm(NO_3)_3 \cdot 6H_2O$ was used. The support was added to a vigorously stirred aqueous solution containing $Pt(NH_3)_2(NO_3)_2$ (Furuya Metal Co. Ltd., Pt: 4.96 wt %) and $In(NO_3)_3 \cdot 8.8H_2O$ (Kanto, 99%) followed by stirring for 3 hours. The mixture was dried under reduced pressure at 50°C followed by reduction under flowing H_2 (50 $mL \cdot min^{-1}$) at 500°C for 1 hour. The loading amount of Pt and Pt/In atomic ratio were fixed

at 3.0 wt% and 1.0, respectively.

3.2.2 Characterization

X-ray absorption fine structure (XAFS) spectra were collected at the BL01B1 and BL14B2 beamlines of SPring-8, Japan Synchrotron Radiation Research Institute (JASRI) using Si (111) double-crystals as monochromator at room temperature. Pt–In loaded samples were pelletized and pretreated with H_2 at 500°C for 30 minutes in a quartz tube to prepare the XAFS specimen. These were then transferred to an Argon glove box (O_2 < 0.01 ppm) without exposure to air after cooling to room temperature with N_2 purge. The pellet was sealed in a plastic film bag (Barrier Nylon) together with an oxygen absorber (ISO A500-HS: Fe powder) to maintain an inert atmosphere. Sm–TiO_2, Sm/TiO_2, and reference samples were measured in air. The obtained XAFS spectra were fitted by Athena and Artemis software ver. 0.9.25 implemented in the Demeter package. FEFF8 was applied to the back-scattering amplitude calculation and phase shift functions.[20] R-factor (R^2) for curve fitting was defined as:

$$R^2 = \sum_i \left\{K^3 \chi_i^{exp}(k) - k^3 \chi_i^{fit}(k)\right\}^2 / \sum_i \left\{k^3 \chi_i^{exp}(k)\right\}^2.$$

The Fourier-transformed infrared (FT-IR) spectra of the prepared catalyst was obtained using a JASCO FT-IR-4200 spectrometer equipped with an MCT detector in transmission mode. The samples (50 mg) were prepared as self-supporting wafers (2.0 cm diameter, <0.5 mm thickness) and placed inside an in-situ IR cell with CaF_2 windows. A custom glass manifold was connected to the cell to control the gas for pretreatment and flowing He. The cell was first purged with He, and the sample was reduced under flowing hydrogen (50 mL·min^{-1}) at 500°C for 30 minutes. After reduction, the wafer was cooled to 100°C under flowing He. After stabilizing for 3 hours, the sample was heated by 2°C/min up to 800°C simultaneously and recorded FT-IR spectra.

The density of surface hydroxyl groups was measured by an MS–TPD technique using a BELCAT II (Microtrac BEL) instrument. First, an appropriate amount of sample placed in a quartz tube was treated at 500°C for 30 minutes under a flow of H_2 (30 mL·min^{-1}). Afterwards, it was cooled down to a stabilization temperature (T_s = 300°C for Sm-doped samples; T_s = 450°C for others) under a flow of H_2 (30 mL·min^{-1}) for a few hours until the MS baseline was

stable. Subsequently, the sample was heated up by 2°C/min from 300°C to 800°C and maintained at 800°C for 2 hours. A mass spectrometer was used to track the signal of H_2O (m/z = 18) during the temperature program.

CO pulse adsorption was performed to estimate the Pt dispersion using the BELCAT II (Microtrac BEL) instrument. Prior to measurement, the catalyst was pretreated at 500°C for 30 minutes under a flow of H_2 (30 mL·min^{-1}). After cooling down to room temperature under He purge, the sample tube was further cooled to −120 °C using a liquid N_2 cooler to promote CO adsorption on Pt sites. A pulse of CO was repeatedly supplied to the catalyst bed until adsorption reached saturation. The number of active sites (perimeter Pt at metal-support interface) was estimated using the Pt dispersion measured by CO adsorption and the nanoparticle size determined by STEM observation (see Figure 3.21 for details) and used for TOF calculation.

3.2.3 Catalytic reaction

Thermal and electroassisted PDH were carried out using a continuous flow fixed-bed quartz reactor with a 6 mm internal diameter. The detailed setup of the reactor is shown in Figure 3.1. The catalyst was placed on a piece of glass wool in the quartz tube reactor. The catalyst powder (100.0 mg) was diluted with sea sand (100.0 mg, Miyazaki Chemical, SiO_2 >99%) for smooth gas flow. Two stainless steel rods (φ 2 mm) were inserted into the reactor as electrodes with contact at the top and bottom of the catalyst bed. A K-type thermocouple covered with a quartz capillary tube (for insulation protection) was also contacted by the catalyst bed to measure the catalyst bed temperature separately from the furnace temperature. Prior to the catalytic reaction, the catalyst was pretreated under flowing H_2/He (10/10 mL·min^{-1}) at 500°C for 30 minutes, followed by purging under flowing He (10 mL·min^{-1}) at 300°C. A constant direct current (3−50 mA) was imposed on the catalyst bed using a high-voltage DC power supply (Tektronix Keithley SMU 2657A). Activity tests were conducted under a reaction gas flow (C_3H_8/He = 10/10 mL·min^{-1}) at 300°C. The product gas was analyzed using a thermal conductivity detection gas chromatograph (Shimadzu GC-8A, column: Unipak S). The C_3H_8 conversion, C_3H_6 selectivity, C_3H_6 yield, and carbon balance are defined as follows:

C_3H_8 conversion: $X_{C_3H_8}\ (\%) = \dfrac{[C_3H_8]_{in} - [C_3H_8]_{out}}{[C_3H_8]_{in}} \times 100$

C_3H_6 selectivity: $S_{C_3H_6}\ (\%) = \dfrac{[C_3H_6]_{out} \times 100}{[C_3H_6]_{out} + \frac{2}{3}[C_2H_6]_{out} + \frac{2}{3}[C_2H_4]_{out} + \frac{1}{3}[CH_4]_{out}}$

C_3H_6 yield: $Y_{C_3H_6}\ (\%) = \dfrac{X_{C_3H_8} \cdot S_{C_3H_6}}{100}$

Carbon balance: $C_b(\%)$

$$= \frac{[C_3H_8]_{out} + [C_3H_6]_{out} + \frac{2}{3}[C_2H_6]_{out} + \frac{2}{3}[C_2H_4]_{out} + \frac{1}{3}[CH_4]_{out}}{[C_3H_8]_{in}}$$

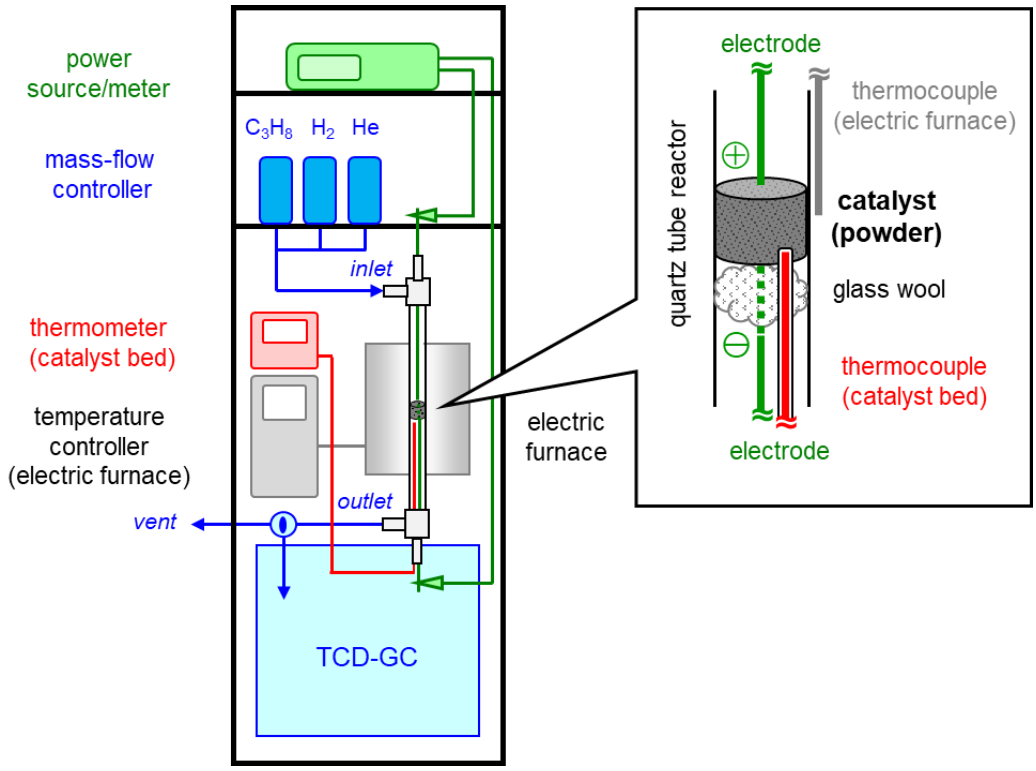

Figure 3.1. The detailed setup of the reactor for electroassisted PDH. The thermocouple for the catalyst bed was covered with a capillary quartz tube for insulation protection. Thermal PDH was also performed using this reactor without imposing a direct current.

3.2.3 Kinetic analysis

We conducted kinetic analysis using a quasi-stationary approximation, which estimates the possible ranges of reaction orders and can be verified by the experimental values. We considered the following Langmuir-Hinshelwood type mechanism for electro-assisted PDH:

$$\mathrm{H^+ \cdot \sigma_0} \underset{E_p}{\overset{E_p}{\leftrightharpoons}} \mathrm{H^+ \cdot \sigma_i} \qquad \text{(1) proton hopping}$$

$$\mathrm{C_3H_8} + \sigma_m \rightleftharpoons \mathrm{C_3H_8 \cdot \sigma_m} \qquad \text{(2) propane physisorption}$$

$$\mathrm{C_3H_8 \cdot \sigma_m + H^+ \cdot \sigma_i} \overset{E_p}{\rightarrow} \mathrm{C_3H_7^+ \cdot \sigma_m + H_2} + \sigma_i \qquad \text{(3) proton collision (RDS)}$$

$$\mathrm{C_3H_7^+ \cdot \sigma_m} + \sigma_i \overset{E_p}{\leftrightharpoons} \mathrm{C_3H_6 \cdot \sigma_m} + H^+ \cdot \sigma_i \qquad \text{(4) deprotonation}$$

$$\mathrm{C_3H_6 \cdot \sigma_m} \rightleftharpoons \mathrm{C_3H_6} + \sigma_m \qquad \text{(5) propylene desorption}$$

where, σ_0, σ_i, and σ_m indicate proton acceptor on TiO_2 surface (excess), proton acceptor at metal-support interface, and metallic adsorption site, respectively. For elementary steps other than the RDS, the forward and reverse reactions can be regarded as being at equilibrium; therefore, equilibrium constants K_i are defined as follows:

$$K_1 = \frac{\theta_{\mathrm{H^+}}}{C_0}$$
$$K_2 = \frac{\theta_{\mathrm{C_3H_8}}}{P_{\mathrm{C_3H_8}}(1-\theta)_m}$$
$$K_4 = \frac{\theta_{\mathrm{C_3H_6}}\theta_{\mathrm{H^+}}}{\theta_{\mathrm{C_3H_7^+}}(1-\theta)_p E}$$
$$K_5 = \frac{P_{\mathrm{C_3H_6}}(1-\theta)_m}{\theta_{\mathrm{C_3H_6}}}$$

where, $\theta_{\mathrm{H^+}}$, $\theta_{\mathrm{C_3H_x}}$, C_0, and E are H^+ coverage at perimeter sites, C_3H_x coverage at metallic adsorption sites, surface proton density (regarded as constant), and electric power supplied to the system, respectively. $(1-\theta)_p$ and $(1-\theta)_m$ indicate the vacancy of σ_p and σ_m, respectively, and can be expressed using θ_x according to as follows:

$$(1-\theta)_p = 1 - \theta_{\mathrm{H^+}}$$
$$(1-\theta)_m = 1 - \theta_{\mathrm{C_3H_8}} - \theta_{\mathrm{C_3H_7^+}} - \theta_{\mathrm{C_3H_6}}$$

Here, the overall reaction rate can be described using the rate equation of the RDS (step 3) as follows:

$$r = k_3 \theta_{C_3H_8} \theta_{H^+} E$$

Note that the contribution of the reverse reaction was ignored because of the differential condition (low conversion). This equation is converted to the following form using the equations of K_1 and K_2:

$$r = k_3 K_1 K_2 C_0 P_{C_3H_8} E (1-\theta)_m$$

Then, the site conservation equation is solved for $(1-\theta)_m$ using the equations of K_i:

$$(1-\theta)_m + \theta_{C_3H_8} + \theta_{C_3H_7^+} + \theta_{C_3H_6} = 1$$

$$(1-\theta)_m + K_2 P_{C_3H_8} (1-\theta)_m + \frac{K_1 C_0}{1 - K_1 C_0} K_4^{-1} K_5^{-1} P_{C_3H_6} E^{-1} (1-\theta)_m + K_5^{-1} P_{C_3H_6} (1-\theta)_m = 1$$

$$\therefore \ (1-\theta)_m = \left(1 + K_2 P_{C_3H_8} + K_5^{-1} P_{C_3H_6} + \frac{K_4^{-1} K_5^{-1} P_{C_3H_6}}{(K_1^{-1} C_0^{-1} - 1) E}\right)^{-1}$$

Thus, we obtain the rate equation as follows:

$$r = \frac{k_3 K_1 K_2 C_0 P_{C_3H_8} E}{1 + K_2 P_{C_3H_8} + K_5^{-1} P_{C_3H_6} + \frac{K_4^{-1} K_5^{-1} P_{C_3H_6}}{(K_1^{-1} C_0^{-1} - 1) E}}$$

Next, this equation is regarded as a function of the single valuable, $P_{C_3H_8}$, C_0, or E.

$$r = k P_{C_3H_8}{}^{\alpha} C_0{}^{\beta} E^{\gamma}$$

Here, two limits of the rate equation are considered such that the order dependence of $P_{C_3H_8}$ becomes the largest and smallest, which provides the possible range of reaction order α.

When $K_2 \gg 1, K_5^{-1}P_{C_3H_6}, \frac{K_4^{-1}K_5^{-1}P_{C_3H_6}}{(K_1^{-1}C_0^{-1}-1)E}$, this equation can be simplified as follows:

$$r = \frac{k_3 K_1 C_0 P_{C_3H_8} E}{P_{C_3H_8} + 1/K_2 + K_5^{-1}P_{C_3H_6}/K_2 + \frac{K_4^{-1}K_5^{-1}P_{C_3H_6}}{(K_1^{-1}C_0^{-1}-1)E}/K_2}$$

$$r \approx k_3 K_1 C_0 E_p$$

$$\because \left(1/K_2, K_5^{-1}P_{C_3H_6}/K_2, \frac{K_4^{-1}K_5^{-1}P_{C_3H_6}}{(K_1^{-1}C_0^{-1}-1)E_p}/K_2 \ll 1\right)$$

On the contrary, when $K_2 \ll 1$, this equation can be simplified as follows:

$$r = \frac{k_3 K_1 K_2 C_0 P_{C_3H_8} E}{1 + K_5^{-1}P_{C_3H_6} + \frac{K_4^{-1}K_5^{-1}P_{C_3H_6}}{(K_1^{-1}C_0^{-1}-1)E}}$$

Therefore, the reaction order α can be 0 and 1 at the higher and lower limit and should always fall into this range.

Similarly, the rate equation is regarded as a function of E and two limits of this equation are considered such that the order dependence of E becomes the largest and smallest, which provides the possible range of reaction order β.

When $\frac{K_4^{-1}K_5^{-1}P_{C_3H_6}}{K_1^{-1}C_0^{-1}-1} \gg 1, K_2P_{C_3H_8}, K_5^{-1}P_{C_3H_6}$, this equation can be simplified as follows:

$$r = \frac{k_3 K_1 K_2 C_0 P_{C_3H_8} E}{E^{-1} + 1/\frac{K_4^{-1}K_5^{-1}P_{C_3H_6}}{K_1^{-1}C_0^{-1}-1} + K_2P_{C_3H_8}/\frac{K_4^{-1}K_5^{-1}P_{C_3H_6}}{K_1^{-1}C_0^{-1}-1} + 1/\frac{K_4^{-1}}{K_1^{-1}C_0^{-1}-1}}$$

$$r \approx k_3 K_1 K_2 C_0 P_{C_3H_8} E^2$$

$$\because \left(1/\frac{K_4^{-1}K_5^{-1}P_{C_3H_6}}{K_1^{-1}C_0^{-1}-1}, K_2P_{C_3H_8}/\frac{K_4^{-1}K_5^{-1}P_{C_3H_6}}{K_1^{-1}C_0^{-1}-1}, 1/\frac{K_4^{-1}}{K_1^{-1}C_0^{-1}-1} \ll 1\right)$$

On the contrary, when $\frac{K_4^{-1}K_5^{-1}P_{C_3H_6}}{K_1^{-1}C_0^{-1}-1} \ll 1$, this equation can be simplified as follows:

$$r = \frac{k_3 K_1 K_2 C_0 P_{C_3H_8} E}{1 + K_2P_{C_3H_8} + K_5^{-1}P_{C_3H_6}}$$

In a similar fashion, the rate equation can be simplified into the following two limitations when it was considered as a sole function of C_0.

$$r = k_3 K_1 K_2 P_{C_3H_8} E$$

$$r = \frac{k_3 K_1 K_2 C_0 P_{C_3H_8} E}{1 + K_2 P_{C_3H_8} + K_5^{-1} P_{C_3H_6} - \frac{P_{C_3H_6}}{K_4 K_5 E}}$$

Based on this derivation, the reaction orders for $P_{C_3H_8}$ (α), C_0 (β), and E (γ) on the overall reaction rate should be described as follows: $0 < \alpha < 1$, $0 < \beta < 1, 1 < \gamma < 2$. This is consistent with the experimental reaction orders (α = 0.22, β = 0.42, and γ = 1.37), which supports the validity of the proposed reaction mechanism.

3.3 Results and discussions

3.3.1 Catalyst synthesis and characterization

First, the dopant cation was selected according to the following criteria: (1) trivalent, to capture a proton by charge compensation, (2) non-reducible and no other oxidation states, and (3) a much larger ionic radius than Ti^{4+} such that bulk region substitution is unfavorable. In this study, Sm^{3+} with an ionic radius (1.086 Å) much larger than that of Ti^{4+} (0.68 Å),[21] was chosen as a dopant for anatase TiO_2 support.[13] Second, Sm should be doped only at the TiO_2 surface region to obtain a higher content of surface hydroxyl groups while retaining the bulk conductivity of TiO_2 support. Therefore, we prepared Sm-doped TiO_2 (Sm–TiO_2) using a hydrothermal method with anatase TiO_2 as a core and Sm-Ti sol for the shell (Figure 3.2a). For the control sample, we also prepared Sm-loaded TiO_2 (Sm/TiO_2) by hydrothermal synthesis of TiO_2 shell on anatase TiO_2 followed by impregnation of Sm^{3+} (Figure 3.3). The X-ray diffraction (XRD) analysis showed that the crystal structure of bulk anatase TiO_2 and the crystallite size changed little upon Sm doping (10–11 nm, Figure 3.4), the latter of which was also consistent with the mean particle size (12.1 nm, Figure 3.5). This indicates that the Sm-containing TiO_2 shell was constructed as a very thin layer on the surface of bare TiO_2. The high-angle annular dark-field scanning transmission electron microscopy (HAADF-STEM) image of Sm–TiO_2 showed bright dots in the TiO_2 crystal (Figure 3.2b), indicating that the doped Sm was highly dispersed in an isolated state. Elemental analysis confirmed that the Sm/Ti ratio (including bare TiO_2) was 0.009 (Figure 3.6) which is consistent with the fed ratio in material synthesis (1 mol %).

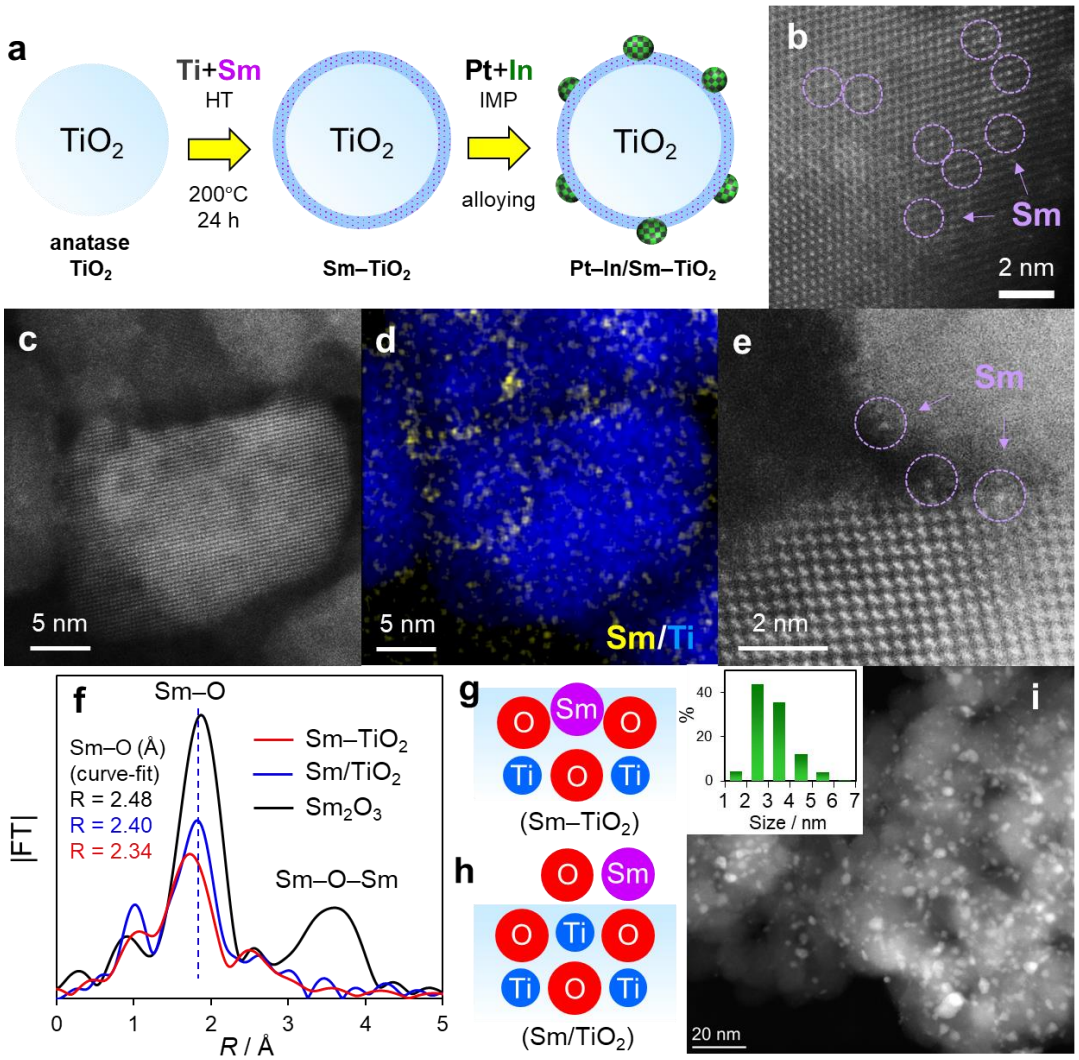

Figure 3.2. (a) Schematic illustration of catalyst preparation: hydrothermal (HT) synthesis of Sm–TiO_2 and the subsequent impregnation and alloying of Pt–In/Sm–TiO_2. (b) HAADF-STEM image and the (c-e) the corresponding cross-sectional analysis of Sm–TiO_2 (Sm: 1 mol%) using FIB etching: (c) HAADF-STEM image, (d) elemental map acquired by EDX, and (e) high-resolution HAADF-STEM image focusing on the surface. (f) Fourier transforms of Sm K-edge EXAFS of Sm-containing samples. Plausible surface structures of (g) Sm-doped and (h) -loaded TiO_2 with ionic radii. (i) HAADF-STEM image of Pt–In/Sm–TiO_2 (Sm: 1 mol%). Inset shows the particle size distribution.

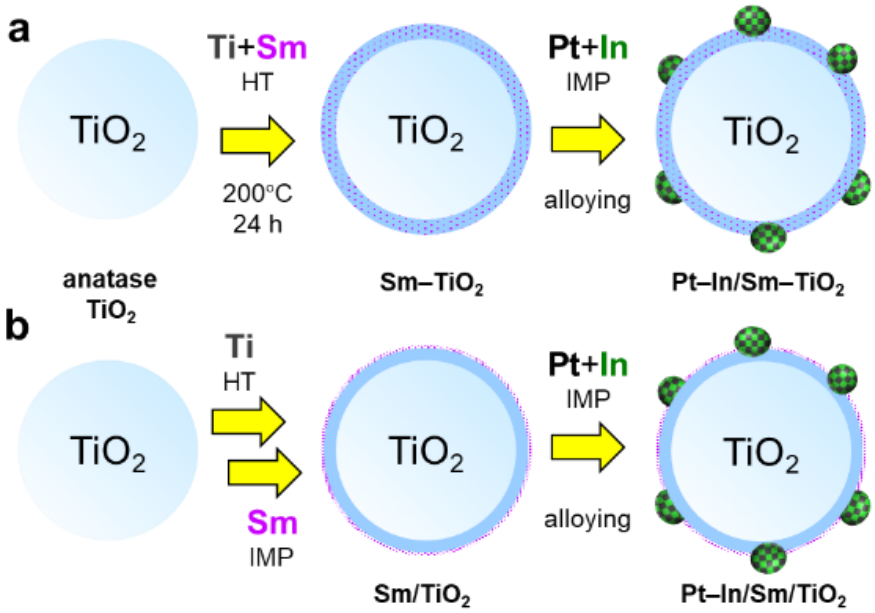

Figure 3.3. Schematic illustration of catalyst preparation: (a) hydrothermal (HT) synthesis for Sm–TiO_2 and the subsequent impregnation (IMP) and alloying for Pt–In/Sm–TiO_2. (b) HT synthesis of Sm-free Ti layer on core anatase TiO_2 and the subsequent Sm-IMP for Sm/TiO_2, followed by Pt+In IMP and alloying for Pt–In/Sm/TiO_2.

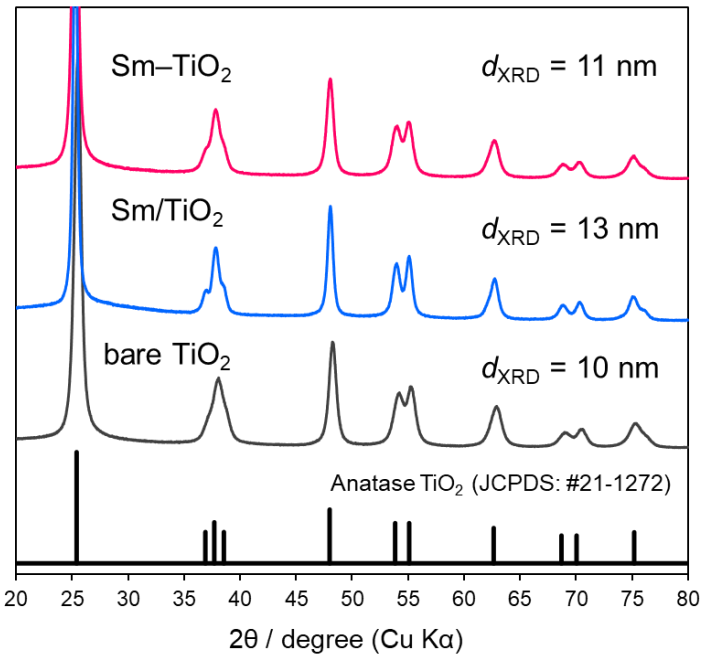

Figure 3.4. XRD patterns of bare TiO_2 (JRC-TIO-7, anatase) and the corresponding Sm-doped (Sm–TiO_2) and -loaded (Sm/TiO_2) samples. Crystallite sizes (d_{XRD}) estimated using Scherrer's equation are shown.

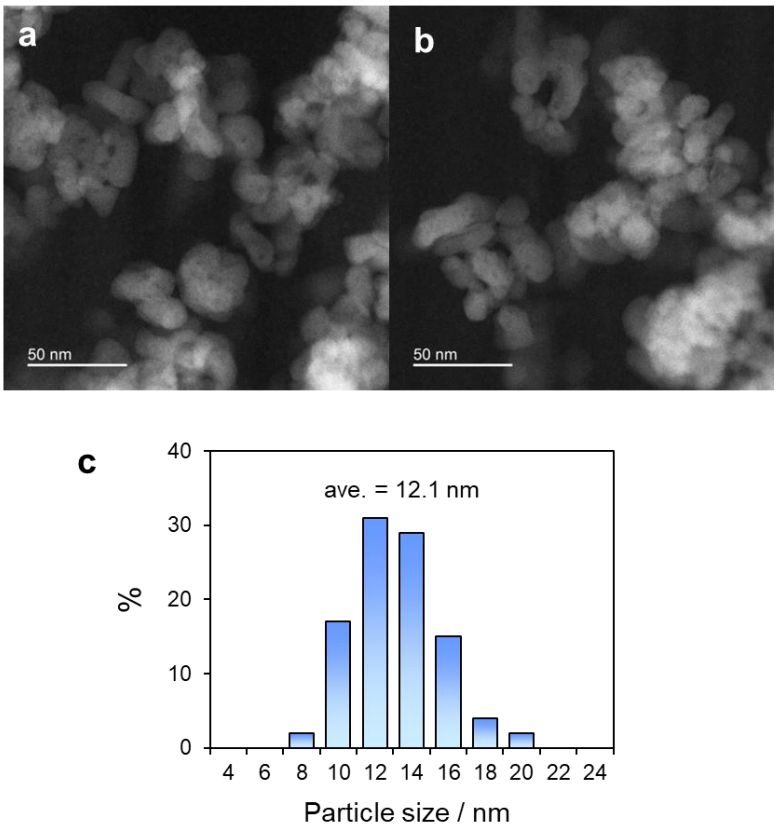

Figure 3.5. (a, b) HAADF-STEM images of Sm–TiO_2 (Sm: 1 mol%) and (c) the corresponding particle size distribution.

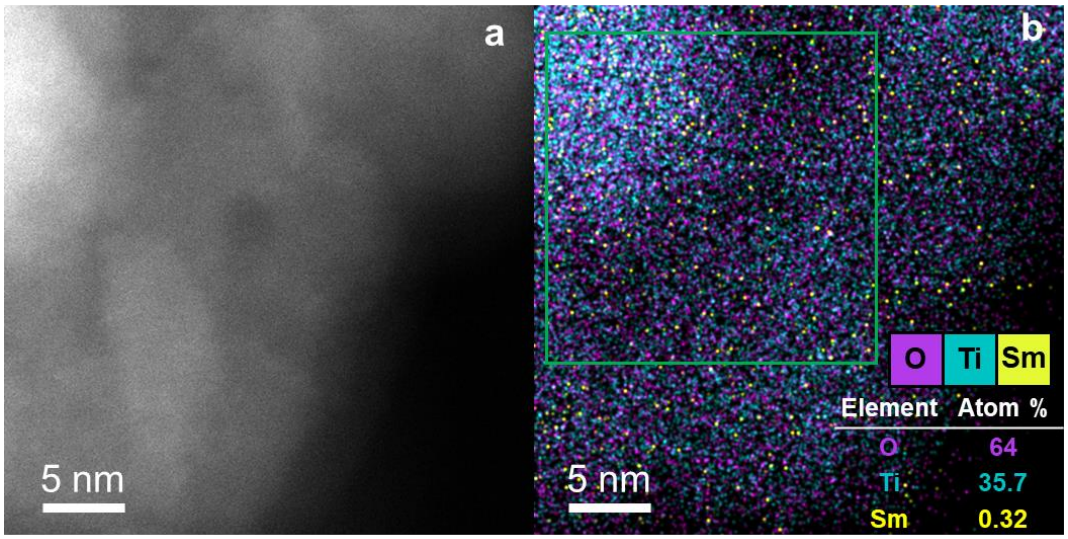

Figure 3.6. (a) HAADF-STEM images of Sm–TiO_2 (Sm: 1 mol%) and (b) the corresponding elemental map acquired by EDX analysis. The Sm/Ti ratio is 0.009, which is consistent with the fed ratio of 1 mol%.

We also performed a cross-sectional analysis of Sm–TiO_2 using fast-ion bombardment (FIB) etching. Cross-sectional HAADF-STEM image revealed that high crystallinity was retained to the outermost surface layers (Figure 3.2c), suggesting that the Sm-containing TiO_2 layer was epitaxially grown on the bare TiO_2. The corresponding elemental map showed that Sm was located mainly on the shell part and grain boundary of the nanocrystals (Figure 3.2d). Although there were some Sm spots overlapping on the bulk part of TiO_2, this may be due to Sm species presenting on the backside surface of TiO_2 nanocrystals. High-resolution HAADF-STEM image showed that Sm actually replaced the surface Ti site (Figure 3.2e), demonstrating that surface doping was successfully performed. X-ray adsorption fine structure (XAFS) analysis was then performed to obtain further structural information. The Sm K-edge X-ray absorption near edge structure (XANES) spectra of Sm–TiO_2 and Sm/TiO_2 showed absorption edge features similar to that of Sm_2O_3, confirming that the Sm species in these samples are in the trivalent state (Figure 3.7). Fourier transforms of the extended XAFS (EXAFS) spectra of Sm–TiO_2 and Sm/TiO_2 showed single coordination peaks assignable to Sm–O without any scattering of the second coordination sphere (Figure 3.2f), which indicates the high dispersion of Sm cations consistent with the results of HAADF-STEM and XRD. Notably, the Sm–O bond

length of Sm–TiO_2 was shorter than those of bulks Sm_2O_3 and Sm/TiO_2 (see Table 3.1 and Figure 3.8 for curve fitting details). This is probably because Sm^{3+} was confined to the surface cation vacancy of TiO_2 (Figure 3.2g), which is narrower than the environment of surface-loaded Sm (Figure 3.2h) and bulk Sm_2O_3.

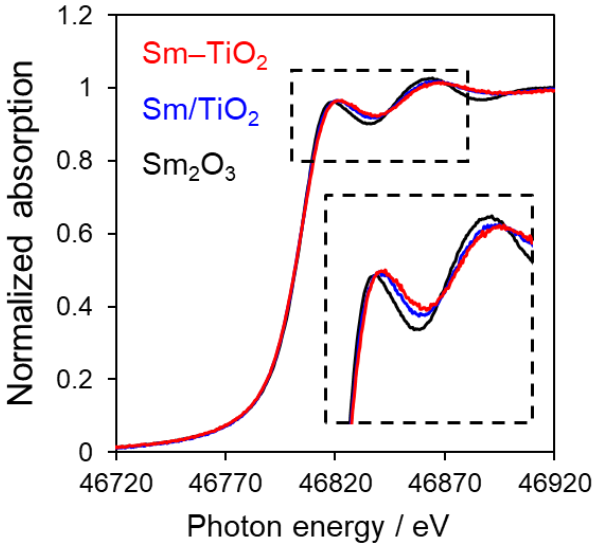

Figure 3.7. Sm K-edge XANES spectra of Sm_2O_3, Sm–TiO_2 (Sm: 1 mol%), and Sm/TiO_2 (Sm: 1 mol%).

Table 3.1. Results of EXAFS curve-fitting for Sm_2O_3, Sm–TiO_2 (Sm: 1 mol%), and Sm/TiO_2 (Sm: 1 mol%).

sample	Shell	S_o^2	CN	r (Å)	ΔE_o (eV)	σ^2 (Å^2)	R-factor
Sm_2O_3	Sm–O Sm–O	1.34	6 (fix) 6 (fix)	2.48 ± 0.01 2.64 ± 0.05	5.2 ± 2.2	0.005 0.014	0.013
Sm–TiO_2	Sm–O	1.34 (fix)	5.4 ± 1.2	2.34 ± 0.02	-6.5 ± 3.0	0.013	0.017
Sm/TiO_2	Sm–O	1.34 (fix)	6.7 ± 0.7	2.40 ± 0.01	-3.3 ± 1.3	0.013	0.004

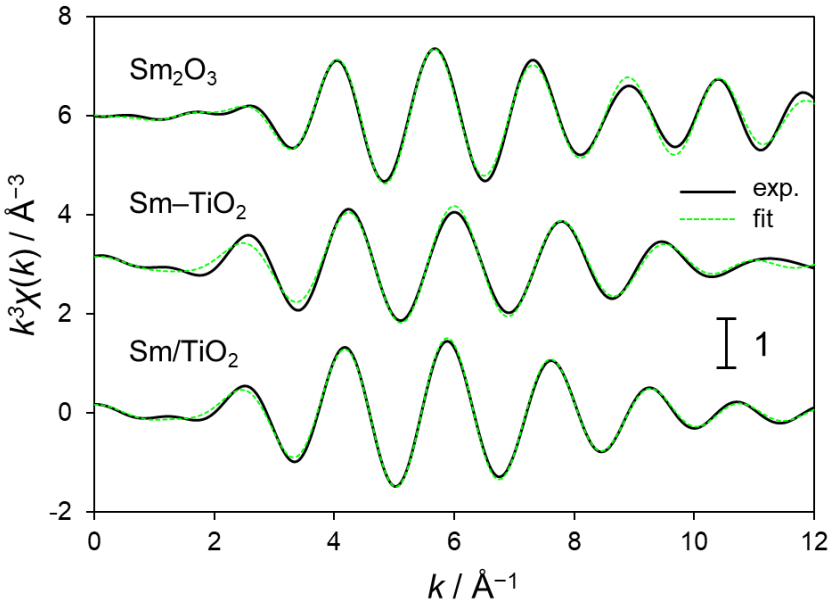

Figure 3.8. EXFAS curve fits for Sm_2O_3, Sm–TiO_2 (Sm: 1 mol%), and Sm/TiO_2 (Sm: 1 mol%).

Then, Pt and In were co-impregnated and alloyed on the Sm-doped and -loaded TiO_2 (Figure 3.2a and 3.3). Figure 3.2i shows the HAADF-STEM image of Pt–In/Sm–TiO_2, wherein the size of Pt–In alloy particles ranges mainly from 2 to 4 nm (average: 2.7 nm). Elemental analysis revealed the Pt:In atomic ratio in the nanoparticle region was 3.00 : 0.97 on average (Figure 3.9). The XAFS analyses revealed that Pt and In were in metallic states (Figure 3.10) and indicated the presence of Pt–Pt and Pt–In scattering with a coordination number ratio close to 2 (5.7/3.1 = 1.84 for Pt–In/Sm–TiO_2, Table 3.2 and Figure 3.11), which is that of the intermetallic Pt_3In phase. These results strongly suggest the formation of intermetallic Pt_3In as small nanoparticles on the Sm-doped TiO_2 surface. Notably, similar XAFS results were obtained for Pt–In/Sm/TiO_2 and Pt–In/TiO_2 (XANES feature and coordination number ratio: 2.0, Table 3.2 and Figure 3.11), indicating that the degree of alloying and electronic state of Pt did not differ depending on the state or presence/absence of Sm.

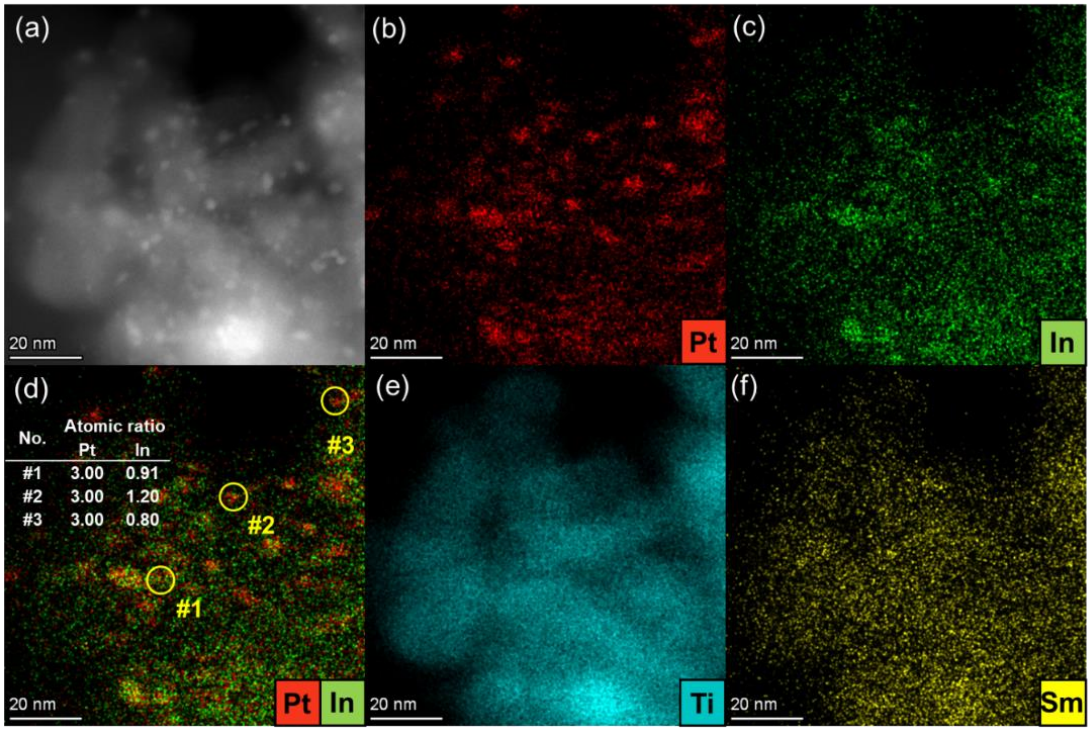

Figure 3.9. (a) HAADF-STEM image of Pt–In/Sm–TiO_2 (Sm: 1 mol%). Corresponding elemental maps of (b) Pt, (c) In, (d) Pt+In, (e) Ti, and (f) Sm, acquired by EDX. Inset in (d) shows the atomic ratio of Pt and In in the regions designated as #1, #2, and #3.

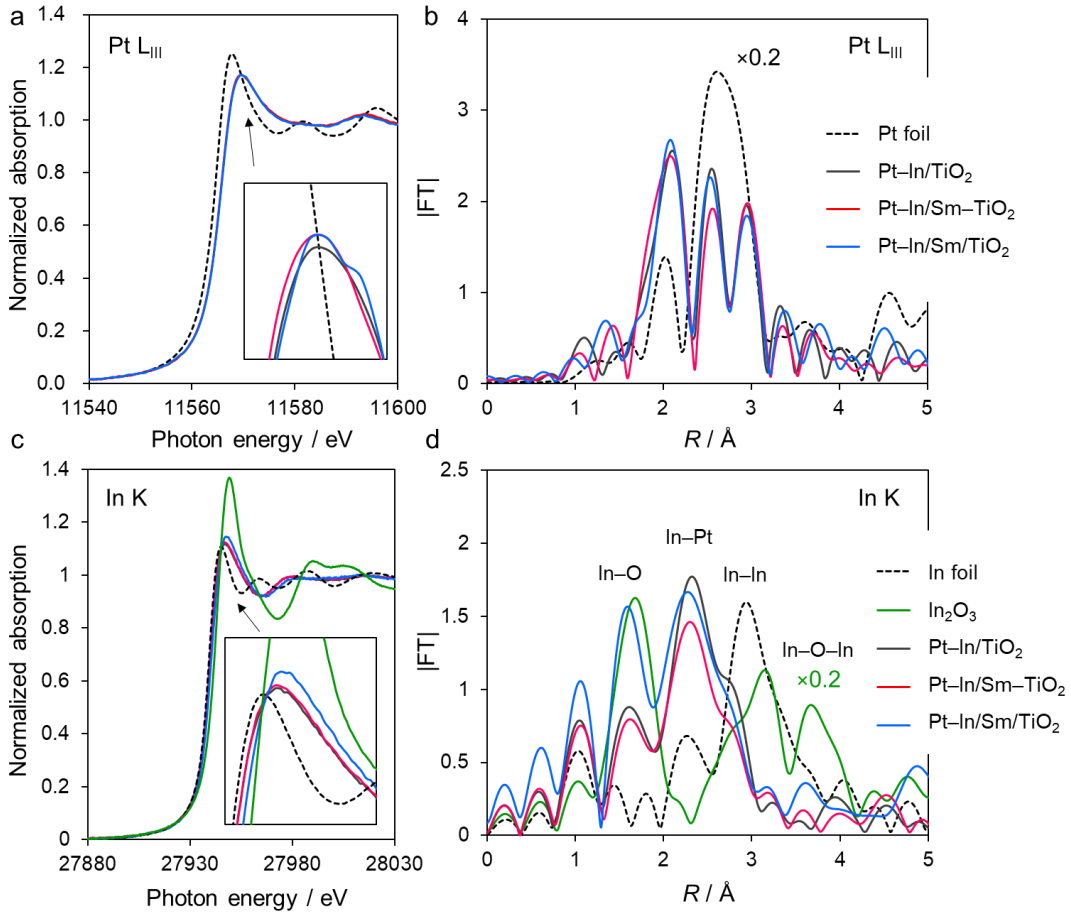

Figure 3.10. Pt LIII-edge (a) XANES and (b) FT-EXAFS spectra of Pt foil and Pt–In catalysts. In K-edge (c) XANES and (d) FT-EXAFS spectra of In foil, In_2O_3, and Pt–In catalysts. The peaks appeared in (b) for the Pt–In catalysts could not be assigned straightforwardly to any specific scatterings because of complex phase cancellation.

Table 3.2. Results of EXAFS curve-fitting for Pt foil and Pt–In catalysts.

sample	shell	S_o^2	CN	r (Å)	ΔE_o (eV)	σ^2 (Å^2)	R-factor
Pt foil	Pt–Pt	0.93	12 (fix)	2.76± 0.03	8.0± 0.9	0.005	0.002
Pt–In/TiO$_2$	Pt–In Pt–Pt	0.93 (fix)	3.0± 0.2 6.0± 0.4	2.70± 0.00 2.78± 0.01	2.4± 0.5	0.011 0.014	0.007
Pt–In/ Sm–TiO$_2$	Pt–In Pt–Pt	0.93 (fix)	3.1± 0.3 5.7± 1.0	2.70± 0.01 2.79± 0.01	2.4± 0.8	0.011 0.013	0.010
Pt–In/ Sm/TiO$_2$	Pt–In Pt–Pt	0.93 (fix)	2.7± 0.2 5.4± 0.4	2.69± 0.01 2.78± 0.01	2.4± 0.7	0.009 0.012	0.011

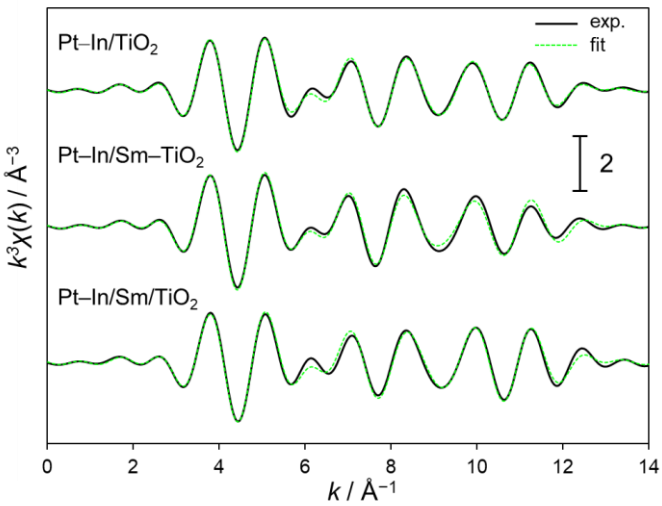

Figure 3.11. EXFAS curve fits for Pt foil and Pt–In catalysts.

3.3.2 Quantification of surface hydroxyl groups

Next, we conducted infrared-mass temperature-programmed desorption (IR–MS–TPD) analysis to correctly quantify the number of surface hydroxyl groups upon Sm doping to TiO_2. Figure 3.12a shows the FT-IR spectra of Pt–In/Sm–TiO_2 at elevated temperatures from 100 to 800°C under He flow. The peaks appearing at 3670 cm^{-1} and 1620 cm^{-1} are assigned to the O–H stretching vibrations of isolated surface hydroxyl groups[21] and the scissors bending mode of molecularly adsorbed water, respectively.[22] The O–H stretching vibration of hydrogen-bonded water was also observed as a broad band around 3300 cm^{-1}. This broad feature was little observed for undoped Pt–In/TiO_2 and Pt–In/Sm/TiO_2 (Figure 3.13), indicating that Sm-doping made the surface more polar due to an increase in the surface hydroxyl group.

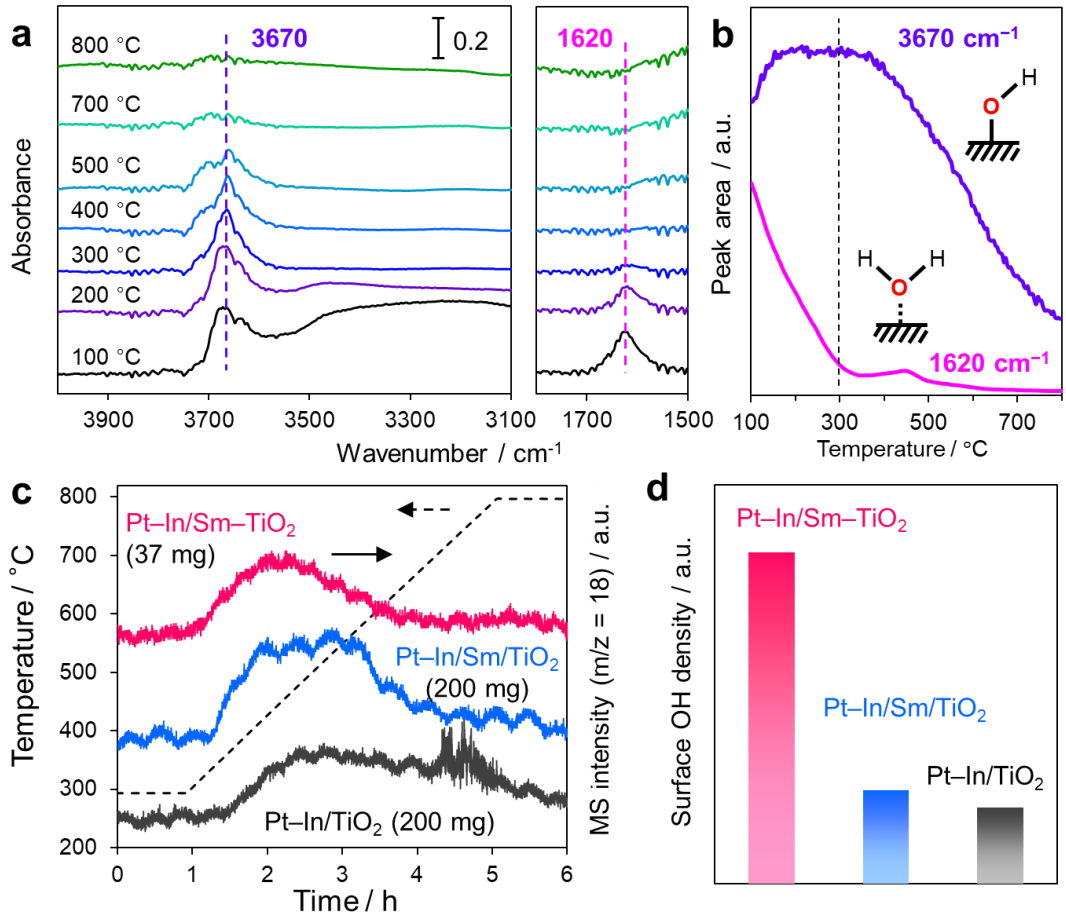

Figure 3.12. Estimation of surface hydroxyl groups by IR–MS–TPD analysis. (a) FT-IR spectra of Pt–In/Sm–TiO_2 upon heating under vacuum. (b) Temperature dependence of the peak area of those at 3670 cm^{-1} and 1620 cm^{-1}. (c) The MS−TPD spectra for the dehydration condensation of surface hydroxyl groups. Values in parentheses indicate the amount of catalyst used for the analysis. (d) The density of surface hydroxyl groups.

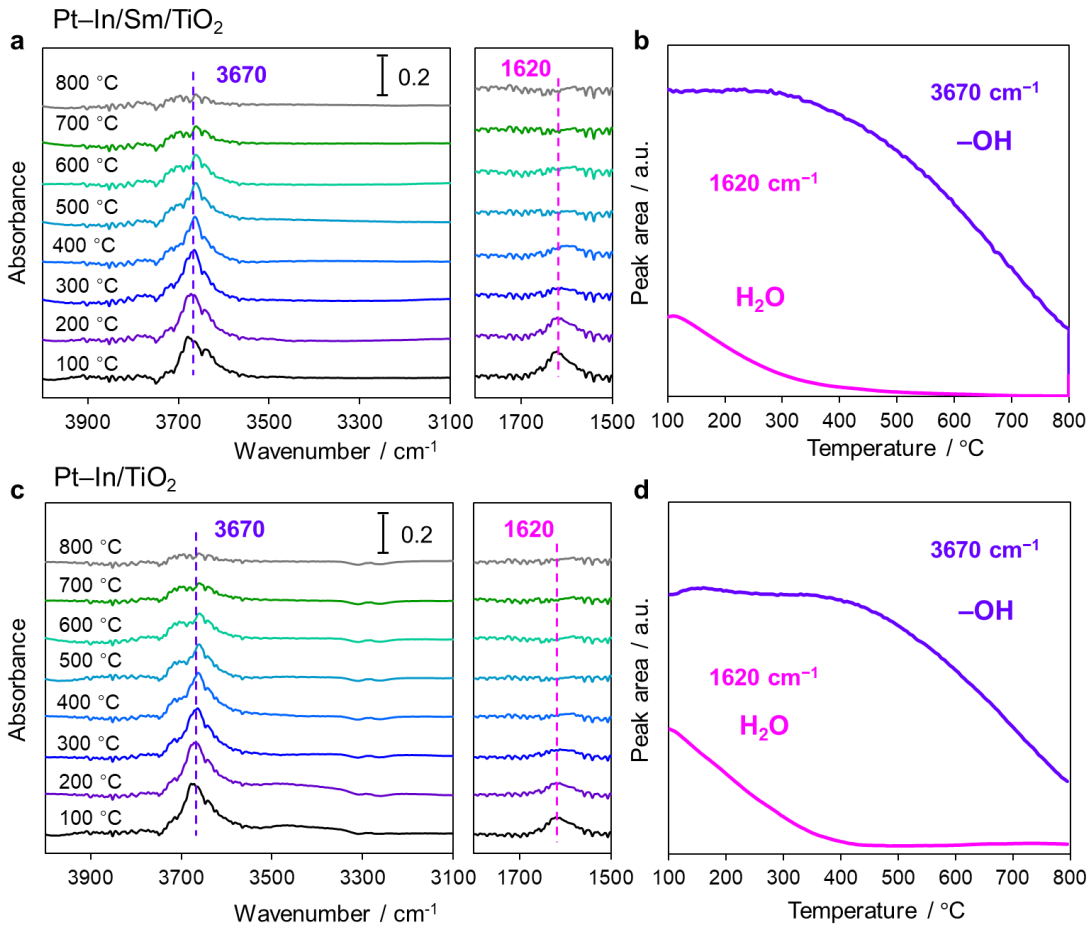

Figure 3.13. (a) FT-IR spectra of Pt–In/Sm/TiO_2 upon heating under He flow and (b) the corresponding temperature dependence of the peak area at 3670 cm^{-1} and 1620 cm^{-1}. (c) FT-IR spectra of Pt–In/TiO_2 upon heating under He flow and (d) the corresponding temperature dependence of the peak area at 3670 cm^{-1} and 1620 cm^{-1}.

Changes in peak area (absorbance) upon heating under He flow were plotted against temperature (Figure 3.13b), which correspond to the qualitative TPD profiles of surface hydroxyl groups and adsorbed water. At 300°C, water desorption completed, while dehydration condensation of surface hydroxyl groups did not start. Therefore, the number of surface hydroxyl groups can be separately quantified when the sample was preheated at 300°C, followed by MS–TPD.[23] Figure 3.13c shows the MS–TPD spectra of the prepared catalysts after dehydration. The amount of desorbed water was determined from the integrated peak area of the TPD spectra. The density of surface hydroxyl groups was estimated as the peak area in the MS–TPD per gram of catalyst, which is summarized in Figure 3.13d. Surface hydroxyl

density of Pt–In/Sm–TiO_2 was approximately 4.4 and 3.6 times higher than those of undoped Pt–In/TiO_2 and Pt–In/Sm/TiO_2, respectively. Thus, Sm doping drastically enriched surface hydroxyl groups on TiO_2. More importantly, the Sm-loaded sample showed only a little enrichment in surface hydroxyl density demonstrating that embedding Sm cations into the lattice of TiO_2 at near surface region is essential for enrichment. The slight increase in surface hydroxyl groups by Sm loading for Pt–In/Sm/TiO_2 might be due to the filling of small amount of cation vacancies originally presenting at the TiO_2 surface.

3.3.3 Catalytic performance in electroassisted PDH

The prepared catalysts were tested in PDH using a fixed-bed continuous flow reactor. Two stainless steel rods were placed as electrodes in contact with the top and bottom of the catalyst bed to impose a direct current on the catalyst (Figure 3.14a, see Figure 3.1 for detailed setup). Before the reaction, the catalyst was pretreated under flowing H_2 at 500°C to reduce the metal particles and TiO_2 supports. Notably, partial reduction of TiO_2 is necessary for moderate bulk conductivity to facilitate surface protonics. Figure 3.14b shows the propylene yield dependence on electric power supplied to the system. Propylene yield was very low (<1%) when no electricity was applied, which corresponds to the thermodynamic equilibrium limitation at 300°C (Figure 3.15). Depending on electric power, the propylene yield monotonously increased, which indicates that PDH occurs with the aid of electricity (see Figure 3.16 for changes in electric power and voltage depending on current). However, electricity dependence vaires widely among catalysts. For Pt–In-loaded catalysts, the catalytic performance order is as follows: Pt–In/Sm–TiO_2 > Pt–In/Sm/TiO_2 > Pt–In/TiO_2, which is consistent with that of surface hydroxyl density (Figure 3.13d). Thus, Sm doping on the TiO_2 surface drastically improved electroassisted PDH catalytic performance. Pt–In/Sm–TiO_2 gave sufficiently high propylene selectivity and carbon balance (>97% and >95%, respectively, Figures 3.14c and d) which can be attributed to the alloying effect by In.[15] Although the catalyst bed temperature slightly increased up to 360°C due to Joule heating (Figure 3.14d), the obtained propylene yields were far beyond thermal catalysis limitation (equilibrium yield at 360°C: 2.0%), suggesting the assistance of external free energy from electricity for the uphill reaction ($\Delta G_{360°C}$ = +41 $kJmol^{-1}$).[24]

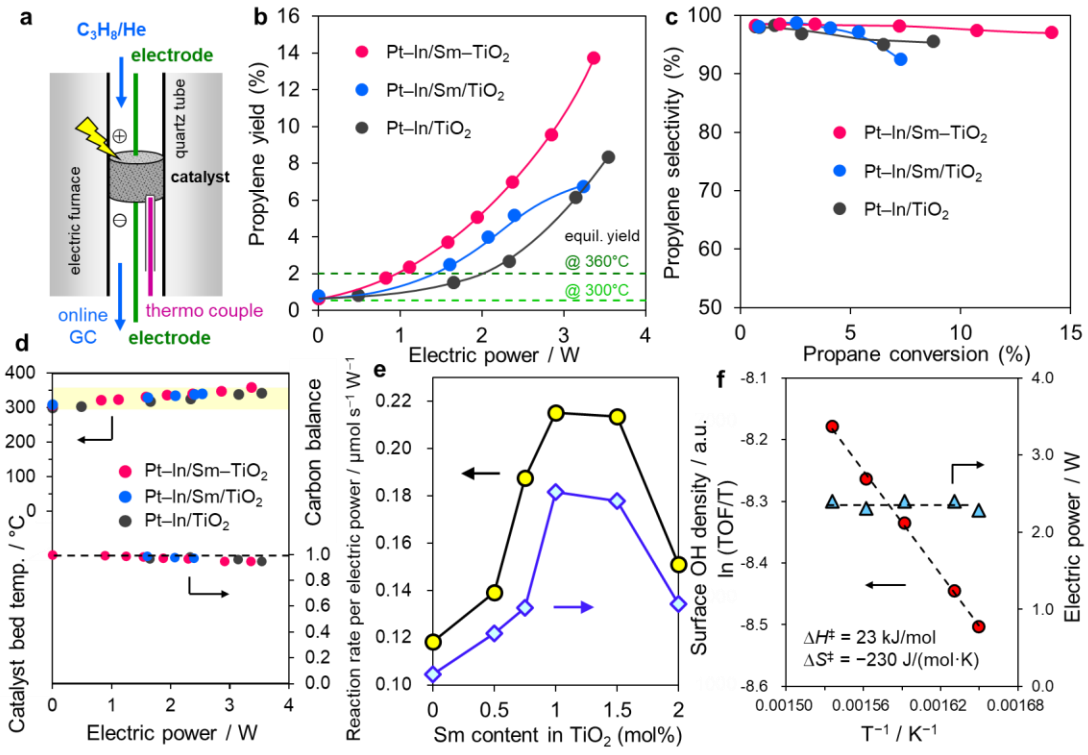

Figure 3.14. (a) Reactor setup. (b) Electroassisted PDH propylene yield dependence on electric power supplied to the catalytic system. Furnace temperature was fixed at 300°C. The dashed line represents the thermodynamic equilibrium propylene yield at 300 and 360°C. (c) Conversion-selectivity curves for electroassisted PDH. (d) Catalyst bed temperature and carbon balance during electroassisted PDH. (e) Changes in the catalytic activity and surface hydroxyl density of Pt–In/Sm–TiO_2 with the content of Sm dopant in TiO_2 varying from 0 to 2 mol%. (f) Eyring plot obtained from electroassisted PDH over Pt–In/Sm–TiO_2.

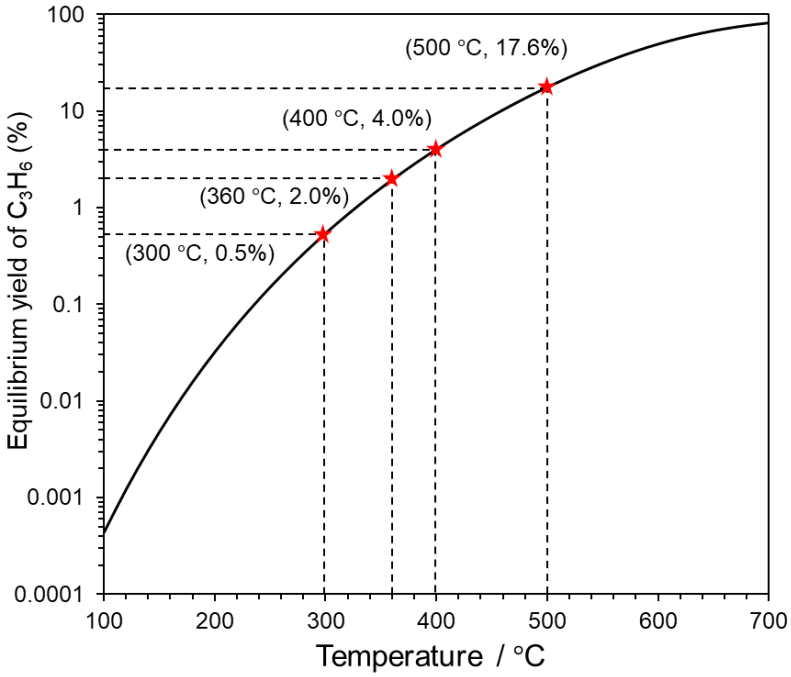

Figure 3.15. Temperature dependence of the equilibrium yield of propylene in thermal PDH (C_3H_8:He = 1:1). Calculation was done using HSC Chemistry 8 software.

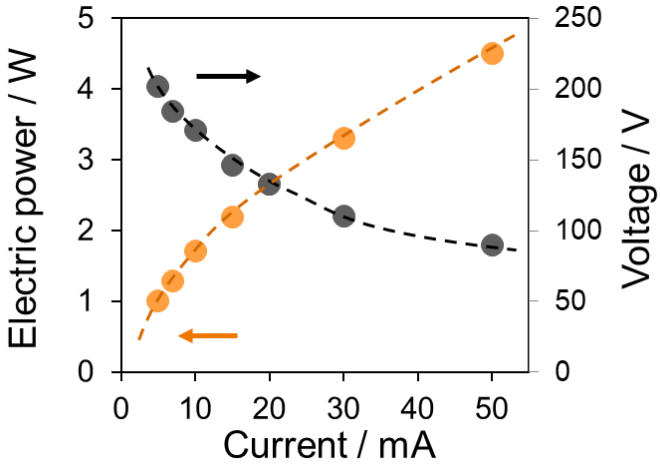

Figure 3.16. The relationship between the imposed current (fixed value) and the corresponding voltage or electric power in electroassisted PDH at 300°C over Pt–In/Sm–TiO_2. Although electric power monotonously increased with current, its slope became smaller at high current region due to lowering of voltage (resistance of TiO_2).

Propylene yield further increased to 19.3% when electric power was elevated to 5.35 W (Table 3.3); this was the highest yield obtained in this study. However, propylene yield and selectivity

slightly decreased for Pt–In/Sm/TiO_2 when electric power exceeded 2.5 W, which implies that Sm cations loaded on TiO_2 have negative effects not only on propane conversion but also on selective propylene formation. Therefore, Sm cations must be doped to the surface Ti sites but not be placed on the TiO_2 surface.

Table 3.3. Conditions for the highest yield of propylene obtained in this study.

catalyst	C_3H_8 conv. (%)	C_3H_6 sel. (%)	C_3H_6 yield (%)	carbon balance	Furnace temp. / °C
Pt–In/Sm–TiO_2 (Sm: 1 mol%)	19.7	97.7	19.3	0.9	300
	current / mA	voltage / V	electric power / W	catalyst bed temp. / °C	equil. yield @400°C (%)
	50	107	5.35	396	4.0

Then, to prove that surface hydroxyl density governs electroassisted PDH catalytic activity, a series of Pt–In/Sm–TiO_2 catalysts with different Sm contents (0.5, 0.75, 1, 1.5, and 2 mol%) were prepared and their performances compared. The XRD patterns of the Pt–In/Sm–TiO_2 catalysts showed that no diffraction other than anatase TiO_2 phase was observed, indicating that no Sm segregation occurred even for 2-mol% Sm doping (Figure 3.17). Figure 3.14e shows Sm content dependence of the density of surface hydroxyl groups (measured by MS–TPD, Figure 3.18). The surface hydroxyl density monotonously increased with Sm doping up to 1-mol%, demonstrating proton enrichment by charge compensation. However, the surface hydroxyl density began to decrease with an increase in Sm content. This is likely because doping a large amount of Sm induced TiO_2 structure deformation at the surface. Next, these catalysts were tested in electroassisted PDH, wherein the activity trend is plotted with the surface hydroxyl density as shown in Figure 3.14e. As a universal scale for catalytic activity in the electroassisted system, we applied propylene formation rates per electric power to the system. The activity trend agreed with the surface hydroxyl density with 1-mol% at the top, demonstrating that the number of surface hydroxyl groups determines the overall reaction rate of electroassisted PDH.

We also tested the stability of Pt–In/Sm–TiO_2 in electroassisted PDH at 300°C, where the specific activity changed little up to 2 hours (Figure 3.19).

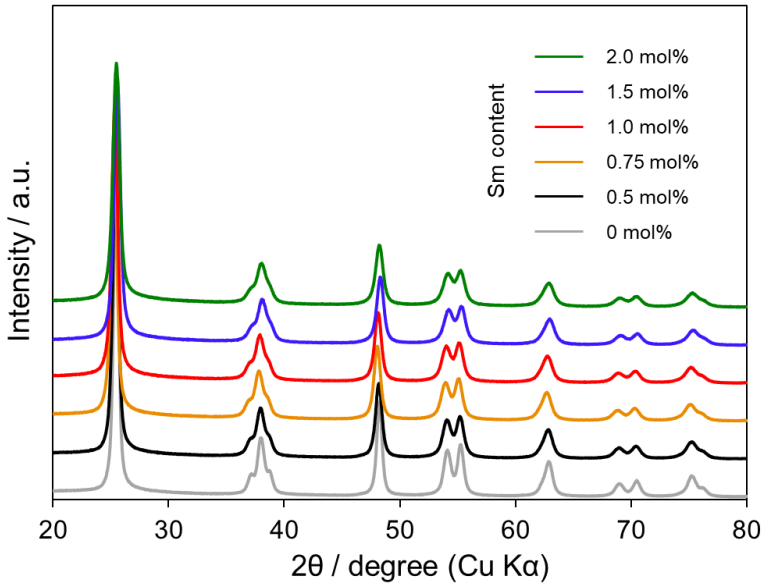

Figure 3.17. XRD patterns of Pt–In/TiO_2 (Sm: 0 mol%) and Pt–In/Sm–TiO_2 (Sm: 0.5–2.0 mol%).

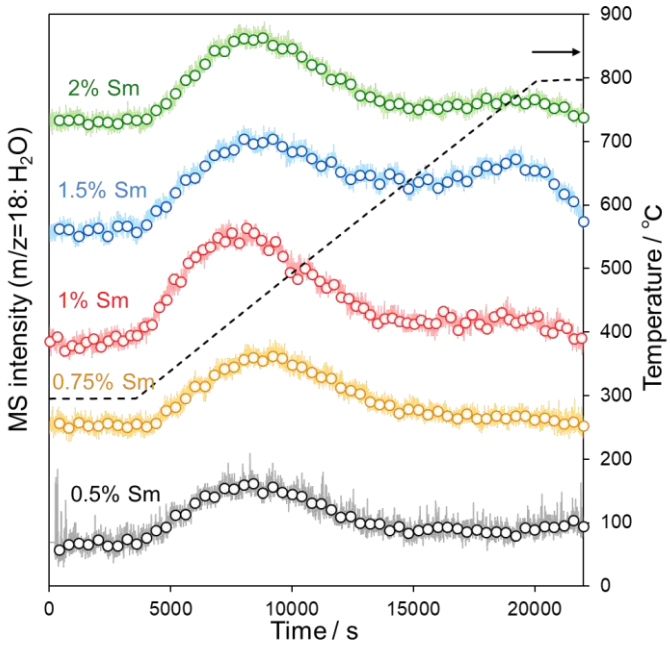

Figure 3.18. MS–TPD spectra for Pt–In/Sm–TiO_2 (Sm: 0.5–2.0 mol%, catalyst amount: 37.0 mg for all).

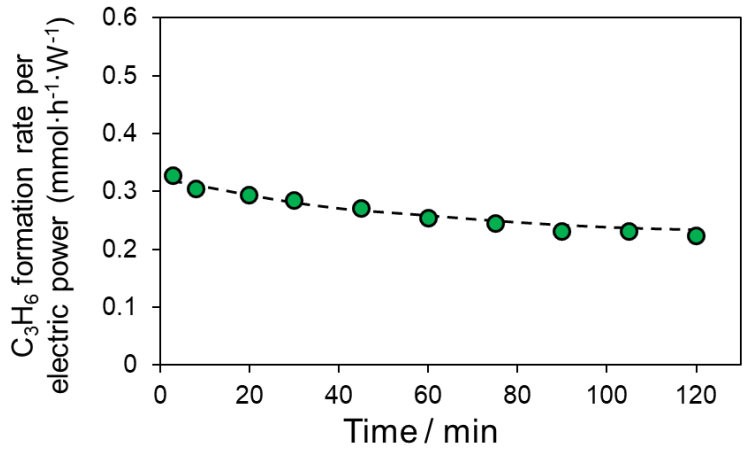

Figure 3.19. Stability test for electroassisted PDH at 300°C over Pt–In/Sm–TiO_2 (Sm: 1.0 mol%).

3.3.4. Mechanistic study

Finally, a mechanistic study was conducted to understand the electroassisted PDH catalytic system. Figure 3.14f shows the Eyring plots obtained from electroassisted PDH over Pt–In/Sm–TiO_2. The $\Delta H^{\ddagger}$ and $\Delta S^{\ddagger}$ values were consistent with those of Pt–In/TiO_2 ($\Delta H^{\ddagger}$ = 21 kJ mol^{-1}, $\Delta S^{\ddagger}$ = −219 kJ mol^{-1}) but much lower than the corresponding values for thermal catalysis ($\Delta H^{\ddagger}$ = 84 kJ mol^{-1}, $\Delta S^{\ddagger}$ = −130 kJ mol^{-1}) we recently reported.[15] This suggests that Sm doping itself did not influence the energetics of electroassisted PDH and consistent with that increasing the number of protons enhanced the overall reaction rate. The much lower $\Delta S^{\ddagger}$ indicates that the rate determining step (RDS) is the proton collision to propane (associative path) unlike C−H activation of propane (dissociative path) in thermal catalysis. A kinetic study was then performed to further understand the role of Sm. The reaction mechanism of electroassisted PDH through surface protonics can be described as follows:

$$H^+ \cdot \sigma_0 \rightleftharpoons H^+ \cdot \sigma_i \quad (1)$$

$$C_3H_8 + \sigma_m \rightleftharpoons C_3H_8 \cdot \sigma_m \quad (2)$$

$$C_3H_8 \cdot \sigma_m + H^+ \cdot \sigma_i \rightarrow C_3H_7{}^+ \cdot \sigma_m + H_2 + \sigma_i \quad (3)$$

$$C_3H_7{}^+ \cdot \sigma_m + \sigma_i \rightleftharpoons C_3H_6 \cdot \sigma_m + H^+ \cdot \sigma_i \quad (4)$$

$$C_3H_6 \cdot \sigma_m \rightleftharpoons C_3H_6 + \sigma_m \quad (5)$$

where, σ_0, σ_i, and σ_m indicate proton acceptor on the surface (excess), proton acceptor at the metal-support interface, and metallic adsorption site, respectively (1: proton hopping, 2: propane physisorption, 3: proton collision to propane, 4: propylene formation, 5: propylene desorption). The overall reaction rate can be derived by solving the rate equation of step 3 as the RDS under a quasi-stationary approximation and the site conservation condition as follows (see section 3.2.3 for details):

$$r = \frac{k_3 K_1 K_2 C_0 P_{C_3H_8} E}{1 - K_2 P_{C_3H_8} - K_5^{-1} P_{C_3H_6} - \frac{K_4^{-1} K_5^{-1} P_{C_3H_6}}{(K_1^{-1} C_0^{-1} - 1) E}} \qquad (6)$$

where, k_n, K_n, P_X, E, and C_0 are the rate equation of step n, equilibrium constant of step n, partial pressure of X, electric power, and surface proton density, respectively. Eq (6) indicates that the reaction order of $P_{C_3H_8}$, C_0, and E range between 0–1, 0–1, and 1–2, respectively. Their experimental reaction orders at 300°C were 0.22, 0.42, and 1.37 (Figure 3.20), respectively which are consistent finely with the predicted order ranges, thereby demonstrating the validity of this kinetic model. Interestingly, the reaction order of $P_{C_3H_8}$ was lower than that reporetd for Pt–In/TiO_2 (0.75), whereas E was very close (1.44).[15] This implies that the contribution of the $K_2 P_{C_3H_8}$ term in the denominator of Eq (6) became larger, namely, propane adsorption (step 2) was favored upon Sm doping. It has been reported that a coordinatively unsaturated metal cation site with a neighboring oxygen vacancy acts as an adsorption site for light alkanes.[1] Therefore, there is a possibility that Sm-doping generates some oxygen vacancies other than surface protons, the former of which act as an effective adsorption site of propane at metal-support interface. Thus, it is likely that Sm doping not only enriches surface proton density but also promotes propane adsorption, both of which accelerate the rate of proton collision on propane (i.e. RDS in electroassisted PDH).

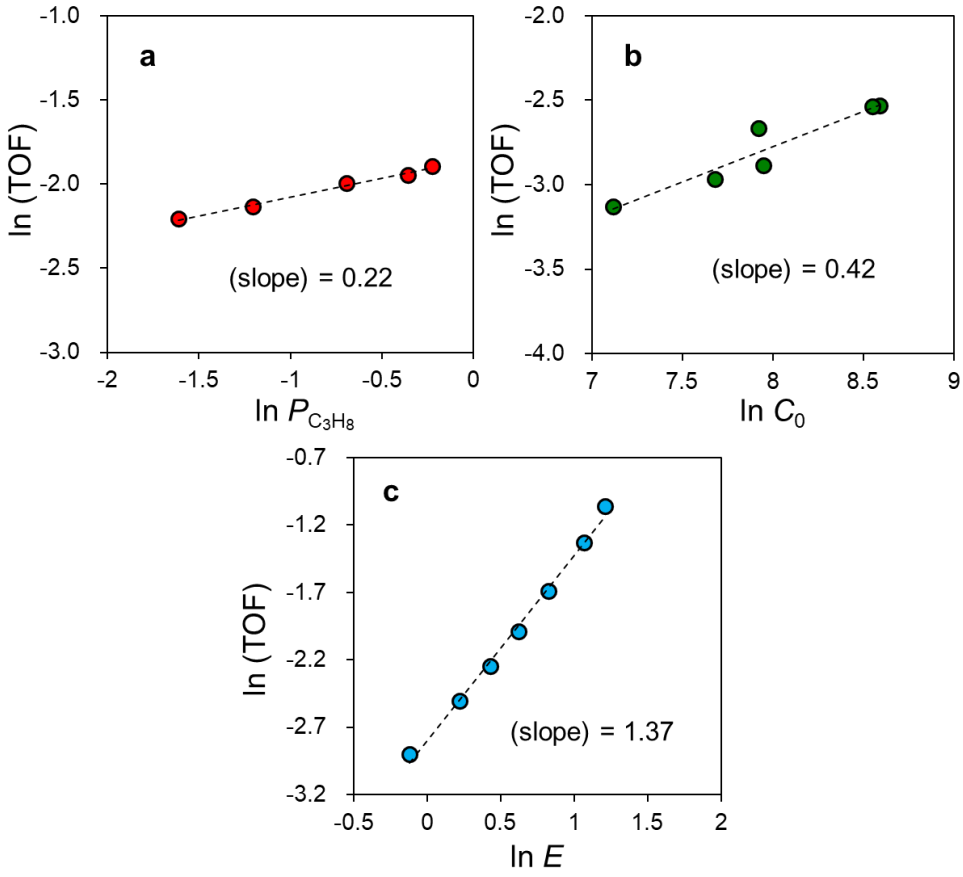

Figure 3.20. (a) Reaction orders of propane partial pressure (P_{C3H8}: E = 2.5 W, constant), (b) surface proton density (C_0: E = 1.9–2.1 W), and (c) electric power (E) in electroassisted PDH at 300°C over Pt–In/Sm–TiO_2 (Sm: 1 mol%). For (b), TOF was estimated as the reaction rate per the number of active site per electric power (s^{-1} W^{-1}) so that the electric power values slightly differed for each samples.

We also evaluated the energy efficiency of this catalytic system based on enthalpy gain from the endothermic reaction ($C_3H_8 \rightarrow C_3H_6 + H_2$: $\Delta H_{300°C}$ = +128.0 kJ mol^{-1}). For example, for the propylene yield of 13.7% by Pt–In/Sm–TiO_2 (at 3.36 W, Figure 3.14b), the enthalpy gain was estimated to be 0.12 J s^{-1} (W), which corresponds to 3.6% energy efficiency for the supplied electric power. In contrast, for undoped Pt–In/TiO_2, the corresponding energy efficiency was 1.7% (0.054 J s^{-1} for 6.2% yield at 3.14 W, Figure 3.14b). Thus, approximately 2.1-fold enhancement in energy efficiency was achieved by the Sm doping strategy. Since the energy loss may be largely due to the bulk conduction of TiO_2 and the resulting Joule heating of the

catalyst, it is reasonable to increase the fraction of surface proton conduction in the overall current by enrichment of surface hydroxyl groups for better efficiency.

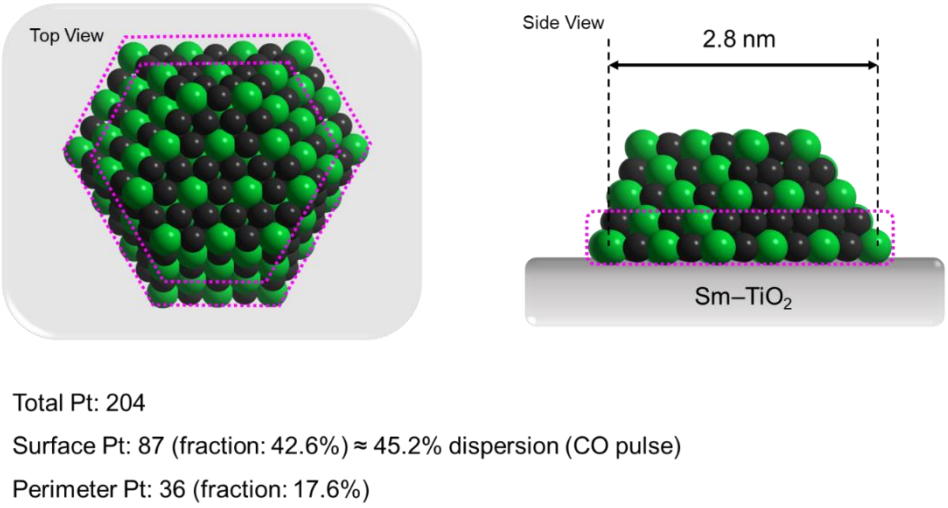

Figure 3.21. A half cuboctahedron model of an intermetallic Pt_3In nanoparticle with (111) and (100) terminations. The particle size was set to 2.8 nm to be consistent with the results of HAADF-STEM observation (2.7 nm). The predicted Pt dispersion of 42.6% is consisted with the experimental value measured by CO pulse chemisorption (45.2%). The fraction of perimeter Pt sites at metal-support interface, which are the active sites for surface protonics, was 17.6% and used for TOF calculation for electroassisted PDH.

3.4 Conclusions

In this study, we designed a novel catalyst for electroassisted low-temperature PDH based on surface protonics chemistry. Sm cations were doped into the surface Ti sites of TiO_2 using anatase TiO_2 as a core and Ti–Sm sol as a shell, which increased the density of surface protons (hydroxyl groups) by charge compensation. Nanoparticulate Pt–In with intermetallic Pt_3In phase was supported on the Sm-doped TiO_2 (Pt–In/Sm–TiO_2), which acted as a highly efficient catalyst for electroassisted PDH at 300°C. The catalytic activity in electroassisted PDH can be controlled by changing the surface hydroxyl density depending on the doping amount of Sm, where 1-mol% is the optimum doping amount. A propylene yield of 19.3% was obtained when an electric power of 5.35 W was applied, which is far beyond the thermodynamic equilibrium limitation. Although Sm doping of TiO_2 itself does not influence the reaction mechanism of electroassisted PDH based on surface protonics, it can drastically increase the overall reaction rate of propylene formation by promoting proton collisions on propane. This promotion is achieved not only by surface proton enrichment but also by the enhancement of propane adsorption by Sm. Thus, the results obtained in this study provide a highly efficient catalytic system for low-temperature alkane conversions and a general catalyst design concept for enhancing electroassisted catalysis based on surface protonics.

References

1. Chen, S.; Chang, X.; Sun, G.; Zhang, T.; Xu, Y.; Wang, Y.; Pei, C.; Gong, J., Propane dehydrogenation: catalyst development, new chemistry, and emerging technologies. *Chem Soc Rev* **2021,** *50*, 3315-3354.

2. Wang, G.; Zhu, X.; Li, C., Recent Progress in Commercial and Novel Catalysts for Catalytic Dehydrogenation of Light Alkanes. *Chem Rec* **2020,** *20*, 604-616.

3. Sattler, J. J.; Ruiz-Martinez, J.; Santillan-Jimenez, E.; Weckhuysen, B. M., Catalytic dehydrogenation of light alkanes on metals and metal oxides. *Chem Rev* **2014,** *114*, 10613-53.

4. Okada, S.; Manabe, R.; Inagaki, R.; Ogo, S.; Sekine, Y., Methane dissociative adsorption in catalytic steam reforming of methane over Pd/CeO_2 in an electric field. *Catalysis Today* **2018,** *307*, 272-276.

5. Manabe, R.; Okada, S.; Inagaki, R.; Oshima, K.; Ogo, S.; Sekine, Y., Surface Protonics Promotes Catalysis. *Sci Rep* **2016,** *6*, 38007.

6. Sato, A.; Ogo, S.; Kamata, K.; Takeno, Y.; Yabe, T.; Yamamoto, T.; Matsumura, S.; Hara, M.; Sekine, Y., Ambient-temperature oxidative coupling of methane in an electric field by a cerium phosphate nanorod catalyst. *Chem Commun (Camb)* **2019,** *55*, 4019-4022.

7. Ogo, S.; Nakatsubo, H.; Iwasaki, K.; Sato, A.; Murakami, K.; Yabe, T.; Ishikawa, A.; Nakai, H.; Sekine, Y., Electron-Hopping Brings Lattice Strain and High Catalytic Activity in the Low-Temperature Oxidative Coupling of Methane in an Electric Field. *The Journal of Physical Chemistry C* **2018,** *122*, 2089-2096.

8. Hisai, Y.; Murakami, K.; Kamite, Y.; Ma, Q.; Vollestad, E.; Manabe, R.; Matsuda, T.; Ogo, S.; Norby, T.; Sekine, Y., First observation of surface protonics on $SrZrO_3$ perovskite under a H_2 atmosphere. *Chem Commun (Camb)* **2020,** *56*, 2699-2702.

9. Manabe, R.; Nakatsubo, H.; Gondo, A.; Murakami, K.; Ogo, S.; Tsuneki, H.; Ikeda, M.; Ishikawa, A.; Nakai, H.; Sekine, Y., Electrocatalytic synthesis of ammonia by surface proton hopping. *Chem. Sci.* **2017,** *8*, 5434-5439.

10. Murakami, K.; Manabe, R.; Nakatsubo, H.; Yabe, T.; Ogo, S.; Sekine, Y., Elucidation of the role of electric field on low temperature ammonia synthesis using isotopes. *Catalysis Today* **2018,** *303*, 271-275.

11. Oshima, K.; Tanaka, K.; Yabe, T.; Kikuchi, E.; Sekine, Y., Oxidative coupling of methane using carbon dioxide in an electric field over La–ZrO_2 catalyst at low external temperature. *Fuel* **2013,** *107*, 879-881.

12. Xu, A.-W.; Gao, Y.; Liu, H.-Q., The Preparation, Characterization, and their Photocatalytic Activities of Rare-Earth-Doped TiO_2 Nanoparticles. *Journal of Catalysis* **2002,** *207*, 151-157.

13. Li, F. B.; Li, X. Z.; Ao, C. H.; Lee, S. C.; Hou, M. F., Enhanced photocatalytic degradation of VOCs using Ln^{3+}–TiO_2 catalysts for indoor air purification. *Chemosphere* **2005,** *59*, 787-800.

14. Graf, C.; Ohser-Wiedemann, R.; Kreisel, G., Preparation and characterization of doped metal-supported TiO_2-layers. *Journal of Photochemistry and Photobiology A: Chemistry* **2007,** *188*, 226-234.

15. Zhang, J.; Ma, R.; Ham, H.; Shimizu, K.-i.; Furukawa, S., Electroassisted Propane Dehydrogenation at Low Temperatures: Far beyond the Equilibrium Limitation. *JACS Au* **2021,** *1*, 1688-1693.

16. Xing, F.; Nakaya, Y.; Yasumura, S.; Shimizu, K.-i.; Furukawa, S., Ternary platinum–cobalt–indium nanoalloy on ceria as a highly efficient catalyst for the oxidative dehydrogenation of propane using CO_2. *Nature Catalysis* **2022,** *5*, 55-65.

17. Wu, Z.; Bukowski, B. C.; Li, Z.; Milligan, C.; Zhou, L.; Ma, T.; Wu, Y.; Ren, Y.; Ribeiro, F. H.; Delgass, W. N.; Greeley, J.; Zhang, G.; Miller, J. T., Changes in Catalytic and Adsorptive Properties of 2 nm Pt_3Mn Nanoparticles by Subsurface Atoms. *Journal of the American Chemical Society* **2018,** *140*, 14870-14877.

18. Wegener, E. C.; Wu, Z.; Tseng, H.-T.; Gallagher, J. R.; Ren, Y.; Diaz, R. E.; Ribeiro, F. H.; Miller, J. T., Structure and reactivity of Pt–In intermetallic alloy nanoparticles: Highly selective catalysts for ethane dehydrogenation. *Catalysis Today* **2018,** *299*, 146-153.

19. Sekine, Y.; Manabe, R., Reaction mechanism of low-temperature catalysis by surface protonics in an electric field. *Faraday Discuss* **2021,** *229*, 341-358.

20. Ankudinov, A. L.; Ravel, B.; Rehr, J. J.; Conradson, S. D., Real-space multiple-scattering calculation and interpretation of x-ray-absorption near-edge structure. *Physical Review B* **1998,** *58*, 7565-7576.

21. Jeantelot, G.; Ould-Chikh, S.; Sofack-Kreutzer, J.; Abou-Hamad, E.; Anjum, D. H.; Lopatin, S.; Harb, M.; Cavallo, L.; Basset, J.-M., Morphology control of anatase TiO_2 for well-defined surface chemistry. *Physical Chemistry Chemical Physics* **2018,** *20*, 14362-14373.

22. Finnie, K. S.; Cassidy, D. J.; Bartlett, J. R.; Woolfrey, J. L., IR Spectroscopy of Surface Water and Hydroxyl Species on Nanocrystalline TiO_2 Films. *Langmuir* **2001,** *17*, 816-820.

23. Ho, S.-W., Surface Hydroxyls and Chemisorbed Hydrogen on Titania and Titania Supported Cobalt. *Journal of the Chinese Chemical Society* **1996,** *43*, 155-163.

24. Gómez-Quero, S.; Tsoufis, T.; Rudolf, P.; Makkee, M.; Kapteijn, F.; Rothenberg, G., Kinetics of propane dehydrogenation over Pt–Sn/Al_2O_3. *Catalysis Science & Technology* **2013,** *3*, 962-971.

Chapter 4

Electroassisted oxidative coupling of methane using carbon dioxide at low temperature

4. Electroassisted Oxidative Coupling of Methane using Carbon Dioxide at Low Temperature

4.1 Introduction

Greenhouse gases elimination is an important subject for mankind to avoid global warming which is already an urgent disaster. Methane and carbon dioxide are greenhouse gases and also the main component of natural gas. Valorization of methane to more valuable chemicals and fuels is a promising technology and gained wide attention.[1] However, it requires a high temperature to activate methane molecules due to its strong C-H bond (434 kJ mol^{-1}). Oxidative coupling of methane (OCM) is promising owing to the directly production of higher value hydrocarbons especially ethane and ethylene which are important base chemicals in the global chemical industry. However, one of the drawbacks of OCM is the overoxidation of $CH_3\cdot$ radicals by oxygen resulting low C2 hydrocarbons selectivity.[2-4]

It is firstly found that the combination of CO_2 can promote OCM reaction by Aika and Nishiyama in 1988. And it was attributed to decrease of free energy by conversion CO_2 to CO at 800°C.[5] Moreover, unlike O_2, CO_2 is much milder and will not induce gas phase radical reactions. Therefore, CO_2 is chosen to replace O_2 in OCM (Equation (1 and 2)) to prevent the sequential reaction of C2 product in the gas phase.[2, 3, 6]

$$2CH_4 + CO_2 \leftrightarrow C_2H_6 + CO + H_2O \quad \Delta H^0_{298} = 106 \text{ kJ mol}^{-1} \qquad (6)$$

$$2CH_4 + 2CO_2 \leftrightarrow C_2H_4 + 2CO + 2H_2O \quad \Delta H^0_{298} = 284 \text{ kJ mol}^{-1} \qquad (7)$$

Besides of CH_4, CO_2 is also a stable due to its strong C–O bond strength (532 kJ mol^{-1}). Therefore, oxidative coupling of methane using carbon dioxide (CO_2–OCM) is not thermodynamically favorable even at temperature higher than 900°C.[5] In addition, the dry reforming of methane is a competitive reaction at such high temperature region and lower the hydrocarbons selectivity. To solve the contradiction of large activity and selectivity, various non-conventional catalytic systems are developed such as plasma,[7, 8] discharge,[9] and electric field[10-12] to achieve low-temperature CO_2–OCM. Among them, electroassisted catalysis based on surface protonics is a promising methodology to achieve low-temperature conversion of

robust reactant molecules such as CH_4,[13] CO_2,[12], and N_2.[14]

In addition, Pt based alloy catalysts are widely used in non-oxidative coupling of methane (NOCM) reactions.[15-17] It was reported that with the addition of second metal such as Bi, Pt becomes less active and complete dehydrogenation is prevented due to electronic effect and ensemble effect, thus achieve highly selective for C–C coupling reaction.[18]

Hence, this chapter reports that a combination of electroassisted catalytic system with Pt based alloy active sites as well as CeO_2 support aims at achieving CO_2–OCM at low-temperature. By using Pt_3Sn/CeO_2 as catalyst, C2 hydrocarbon yield of 4.06% was achieved even at 300°C of external temperature which is times higher than the thermal equilibrium yield. Notably, a certain amount of C_3 hydrocarbons is also produced demonstrating the promising utilization in the future. (Scheme 4.1)

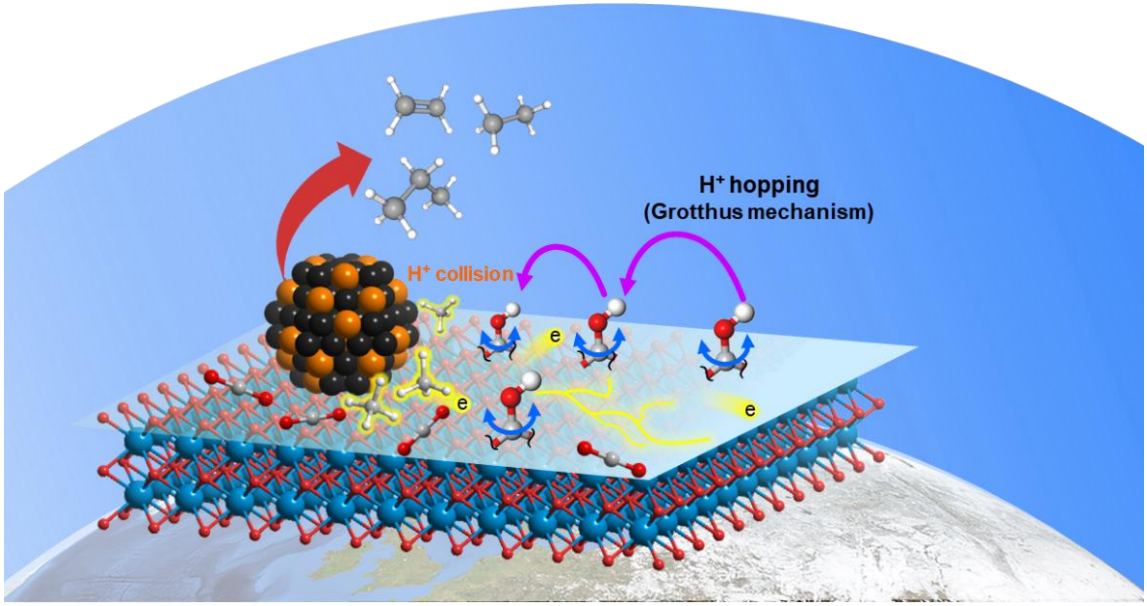

Scheme 4.1. The electroassisted CO_2–OCM which include H^+ hopping and H^+ collision processes.

4.2 Experimental section

4.2.1 Catalyst preparation

Pt/CeO_2, Pt_3Sn/CeO_2, Pt_3Bi/CeO_2, Pt_3Ga/CeO_2, Pt_3Ge/CeO_2, and Pt_3In/CeO_2 (Pt: 3wt%) were prepared by a conventional impregnation method using $Pt(NH_3)_2(NO_3)_2$ (Furuya Metal Co. Ltd., purchased as an aqueous solution with 4.96 wt% of Pt) and/or $(NH_4)_2SnCl_6$, $Bi(NO_3)_3{\cdot}5H_2O$, $Ga(NO_3)_3{\cdot}8H_2O$, $(NH_4)_2GeF_6$, $In(NO_3)_3{\cdot}8.8H_2O$ as metal precursors. The CeO_2 support (JRC–CEO–2, S_{BET} = 123.1 m^2g^{-1}) was added to a vigorously stirred aqueous solution (50 mL ion-exchanged water per gram of CeO_2) containing Pt and the corresponding second metal precursor (Pt: Sn = 3:1, Pt : Bi = 3:1, Pt : Ga = 3:1, Pt : Ge = 3:1, Pt : In = 3:1), followed by stirring for 3 hours at room temperatures. The mixture was dried under a reduced pressure at 50 °C using a rotary evaporator, followed by calcination under flowing air at 500°C for 1 h and reduction under flowing H_2 (50 $mL{\cdot}min^{-1}$) at 600 °C for 1 h.

4.2.2 Catalytic reaction

Electroassisted CO_2–OCM was carried out using a continuous flow fixed-bed quartz reactor with a 6 mm internal diameter. The detailed setup of the reactor is shown in Figure 4.1. The Pt or Pt-based bimetallic alloy supported by CeO_2 catalyst was placed on a piece of glass wool in the quartz tube reactor. Two stainless steel rods (φ 2 mm) were inserted into the reactor as electrodes and contacted with the top and bottom of the catalyst bed. A K-type thermocouple covered with a glass capillary tube (for insulation protection) was also contacted with the catalyst bed to measure the catalyst bed temperature separately from the furnace temperature. Prior to the catalytic reaction, the catalyst was pretreated under flowing H_2/He (5/10 $mL{\cdot}min^{-1}$) at 600°C for 0.5 h, followed by purging under flowing He (10 $mL{\cdot}min^{-1}$) at the reaction temperature. A constant direct current (5 mA) was imposed to the catalyst bed using a high-voltage DC power supply (Tektronix Keithley SMU 2657A). Activity tests were conducted under a reaction gas flow (CH_4: 2.8 $mL{\cdot}min^{-1}$, CO_2: 1 $mL{\cdot}min^{-1}$, He: 7.4 $mL{\cdot}min^{-1}$) at a specific temperature of 300°C. The product gas was analyzed using a thermal conductivity detection gas chromatograph (Shimadzu GC-8A, column ShinCarbon).

The conversions of methane and carbon dioxide, selectivity and yield of various products, consumption rates of methane and carbon dioxide per electric power, and carbon balance were

defined as follow:

$$Conversion\ CH_4: Conv._{CH4} = \frac{CH_{4,in} - CH_{4,out}}{CH_{4,in}}$$

$$Conversion\ CO_2: Conv._{CO2} = \frac{CO_{2,in} - CO_{2,out}}{CO_{2,in}}$$

$$Selectivity\ C_2H_4: S_{C_2H_4} = \frac{2C_2H_{4,\,out}}{CO* + 2(C_2H_{4,\,out} + C_2H_{6,\,out}) + 3(C_3H_{6,\,out} + C_3H_{8,\,out})}$$

$$Selectivity\ C_2H_6: S_{C_2H_6} = \frac{2C_2H_{6,\,out}}{CO* + 2(C_2H_{4,\,out} + C_2H_{6,\,out}) + 3(C_3H_{6,\,out} + C_3H_{8,\,out})}$$

$$Selectivity\ C_3H_6: S_{C_3H_6} = \frac{3C_3H_{6,\,out}}{CO* + 2(C_2H_{4,\,out} + C_2H_{6,\,out}) + 3(C_3H_{6,\,out} + C_3H_{8,\,out})}$$

$$Selectivity\ C_3H_8: S_{C_3H_8} = \frac{3C_3H_{8,\,out}}{CO* + 2(C_2H_{4,\,out} + C_2H_{6,\,out}) + 3(C_3H_{6,\,out} + C_3H_{8,\,out})}$$

$$Selectivity\ CO: S_{CO} = \frac{CO*}{CO* + 2(C_2H_{4,\,out} + C_2H_{6,\,out}) + 3(C_3H_{6,\,out} + C_3H_{8,\,out})}$$

$$CO* = CO_{out} - (CO_{2,in} - CO_{2,out})$$

$$Yield: Y = Conv. \times S$$

$$Consumption\ rate\ of\ CH_4\ per\ electric\ power: R_{CH_4} = \frac{CH_{4,\,in} - CH_{4,\,out}}{E_p}$$

$$Consumption\ rate\ of\ CO_2\ per\ electric\ power: R_{CO_2} = \frac{CO_{2,\,in} - CO_{2,\,out}}{E_p}$$

Where, CO* represents CO converted from CH_4 by dry reforming reaction; E_p represents the electric power.

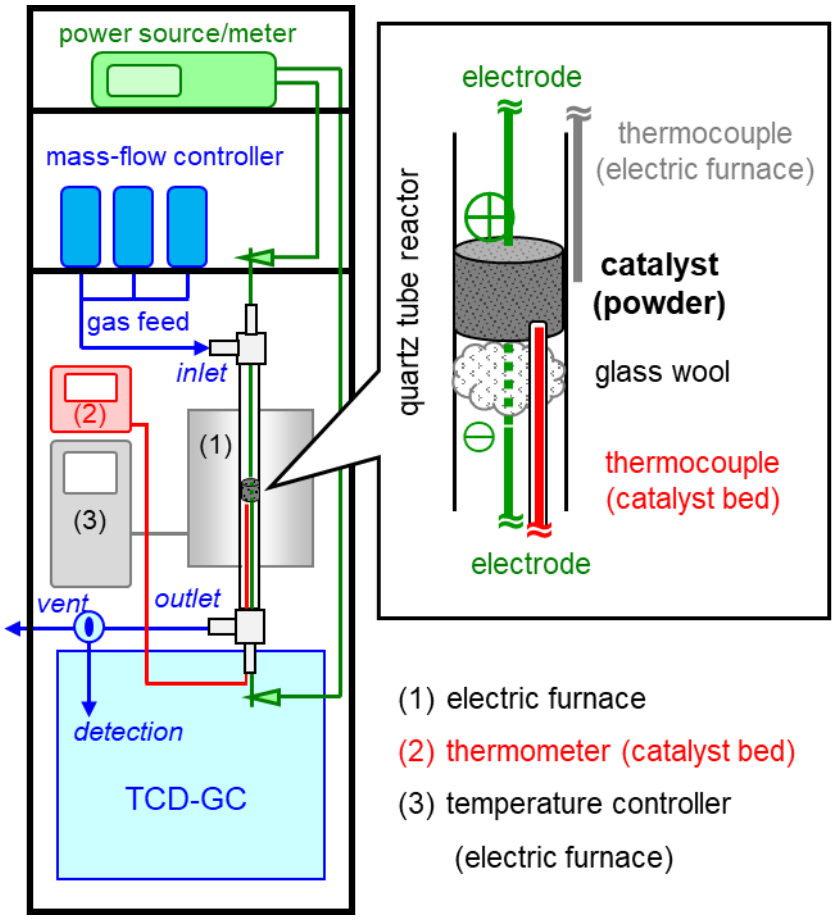

Figure 4.1. The detailed setup of the reactor for electroassisted CO_2–OCM. The thermocouple for the catalyst bed was covered with a capillary glass tube for insulation protection.

4.3 Results and discussion

The prepared catalysts were tested in electroassisted CO_2–OCM using a fixed-bed continuous flow reactor. Two stainless steel rods are electrodes were placed in contact with the top and bottom of the catalyst bed to impose a direct current to the catalyst (Figure 4.1) Before the reaction, the catalysts were pretreated with flow H_2 at 600°C, so that the metal nanoparticles and CeO_2 support were reduced to flow electricity.

We examined the catalytic activities of Pt and Pt-based binary alloy supported on CeO_2, as listed in Table 4.1. Under thermal condition, the conversions of methane and carbon dioxide are limited by thermodynamic equilibrium as shown in Figure 4.2. The 10% conversion of methane requires temperature higher than 600°C (Figure 4.2a). However, under such severe temperature, the produced C2 and C3 hydrocarbons are more reactive than methane and are further oxidized by CO_2 resulting the poor C2 and C3 yield (Figure 4.2b). On the other hand, when 5 mA of direct current was applied to catalysts, conversions of methane and carbon dioxide increased drastically (Table 4.1). The catalyst bed temperature did not increase significantly during energization (Table 4.1), indicating that Joule heating made a negligible contribution to catalysis. Thus, compared to the thermodynamic equilibrium yield (0.002%), the highest yield of C2 hydrocarbons (4.06%) was achieved over Pt_3Sn/CeO_2 catalyst (Table 4.1 and Figure 4.3) using 2.73 W of electric power even at low external temperature of 300°C. Moreover, the yield of C3 hydrocarbons (0.34%) was also remarkably increased by electricity compared with the thermodynamic equilibrium yield (virtually zero). The production of C3 hydrocarbons probably due to ethylene to propylene (ETP) reaction over the Brønsted acid sites on CeO_2 support.[19, 20] Therefore, the electric field played an essential role to achieve CO_2–OCM under such low temperature.

Table 4.1. Catalytic activities of Pt and Pt-based binary alloy supported on CeO_2 catalysts in the electric field: flow rate, CH_4: 2.8 mL·min^{-1}, CO_2: 1 mL·min^{-1}, He: 7.4 mL·min^{-1}; input current: 5 mA; furnace temperature: 300°C; catalyst weight: 100.0 mg.

Catalyst	Electric power / W	Catalyst bed temperature / °C	Conversions / %		Yield / %		Carbon balance
			CH_4	CO_2	C2	C3	
Pt/CeO_2	1.02	302	4.5	12.65	0.04	0	0.95
Pt_3Sn/CeO_2	2.73	334	21.94	33.51	4.06	0.34	0.91
Pt_3Bi/CeO_2	0.84	310	16.47	43.31	2.82	0.19	0.89
Pt_3Ga/CeO_2	1.24	323	6.35	28.99	0.48	0	0.94
Pt_3Ge/CeO_2	1.52	315	9.6	32.64	0.05	0	0.92
Pt_3In/CeO_2	1.02	304	2.35	13.78	0.07	0	0.96

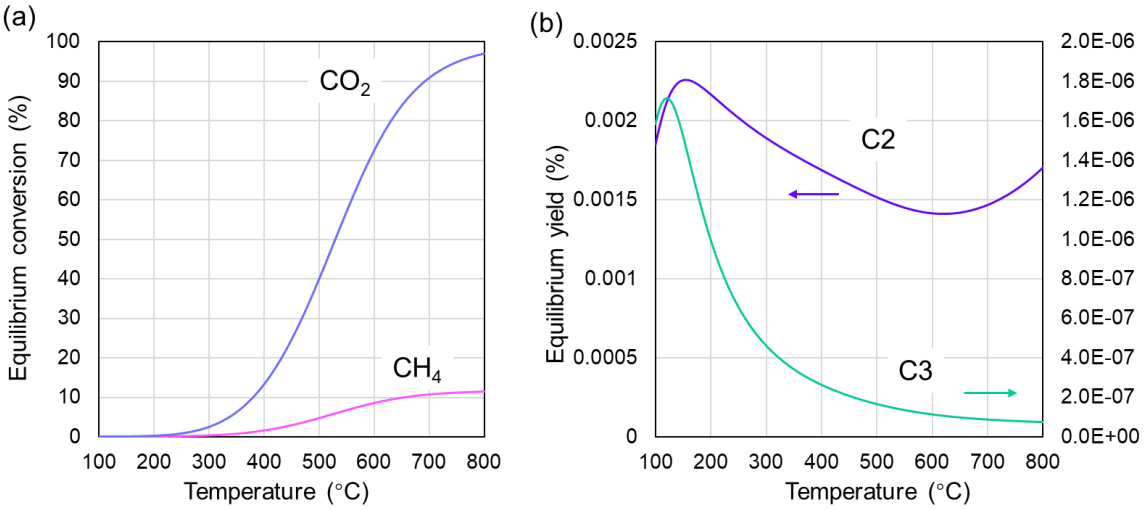

Figure 4.2. Temperature dependence of the (a) equilibrium conversions (CH_4 and CO_2) and (b) yields of product hydrocarbons (C2 and C3 hydrocarbons) in thermal CO_2–OCM (CH_4: CO_2: He = 2.8:1:7.4). Calculation was done using HSC Chemistry 8 software.

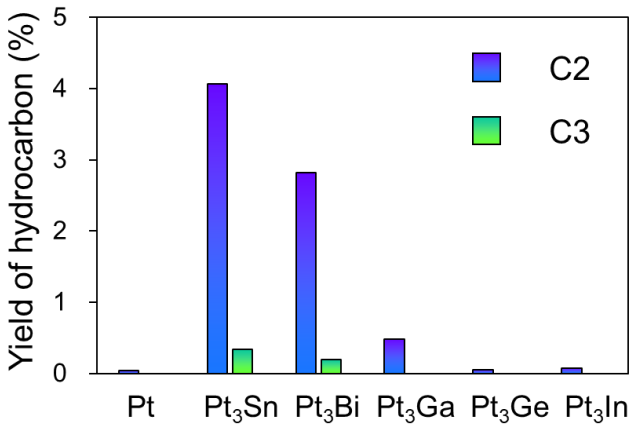

Figure 4.3. Yields of hydrocarbons over Pt and Pt-based binary alloy supported on CeO_2 catalysts in the electric field.

The values of electric power for these catalysts are in a narrow range (0.84–1.52 W) expect for Pt_3Sn/CeO_2 catalyst, probably due to the experimental error that the varying packing density causes changed electronic conductivity of catalyst bed. Therefore, we calculated the consumption rates per electric power of methane and carbon dioxide to evaluate the catalytic performance of catalysts to eliminate this experimental error.

In Figure 4.4b, the consumption rate per electric field of methane and carbon dioxide were plotted by pink line and bule line respectively, while product distributions are illustrated as bar charts. (Definitions of consumption rate per electric power, product selectivity in the section 4.2.2.) Interestingly, compared with Pt/CeO_2 catalyst, after alloying with Sn and Bi, the consumption rates per electric power of methane were drastically increased. In contrast the consumption rates per electric power of carbon dioxide remained intact for Pt/CeO_2 and Pt-based bimetallic catalyst. It implies that the activation of methane was affected by composition of Pt-bimetallic alloy which has negligible effect on the conversion of carbon dioxide.

It was reported that Pt was negatively charged upon alloying with Sn, Bi due to electronic effect.[21, 22] And under electric field, H^+ hopping is facilitated by the Grotthuss mechanism and a cationic transition state $[CH_3–H–H]^+$ was generated by H^+ collision to methane at metal-support interface sites.[23, 24] Simultaneously, CO_2 was activated by CeO_2 support to produce oxygen active species.[6, 25, 26] The transition state converted into methyl radical ($CH_3\cdot$) and H_2O with oxygen active species, the former combined each other to form ethane.[27] Therefore,

alloying of Pt with Sn or Bi promotes this process, probably because the negatively charged Pt stabilizes the cationic transition state.[23] Furthermore, alloying of Sn or Bi with Pt can inhibit further dehydrogenation to prevent production of syngas then increase the C2 hydrocarbons selectivity.[15, 16] Therefore, the high C2 hydrocarbons yield was achieved by synergistic effect of electric field and Pt-based bimetallic alloy catalyst.

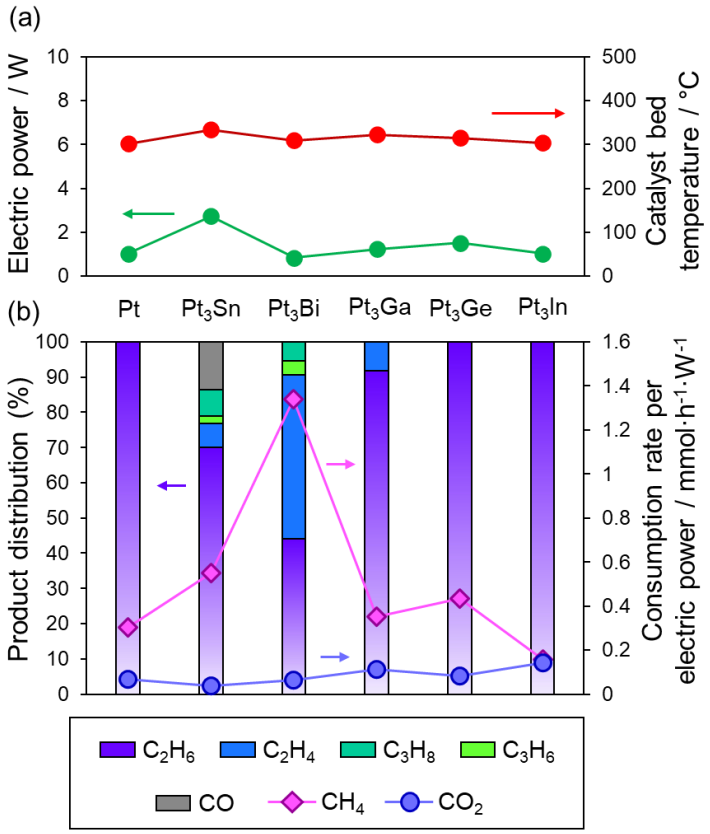

Figure 4.4. Catalytic activities of Pt and Pt-based binary alloy supported on CeO_2 catalysts in the electric field: (a) The electric power varies from 0.84 to 2.73 W due to the difference in resistance of catalyst bed. The catalyst bed temperature varies from 302 to 334°C which are slightly higher than furnace temperature due to Joule heating. (b) Production distribution and consumption rate per electric power of electroassisted CO_2–OCM over various catalysts.

4.4 Conclusion

In summary, the effective production of C2 and C3 hydrocarbons was achieved by electroassisted CO_2–OCM. With the aid of 2.73 W electric power, Pt_3Sn/CeO_2 catalyst afforded a 4.06% C2 hydrocarbons yield and 0.34% C3 hydrocarbons yield even at low external temperature of 300°C. With CeO_2 as support, electric field and Pt-based bimetallic alloy showed synergistic effect, which effectively enhanced both the catalytic activity and selectivity.

Reference

1. Olivos-Suarez, A. I.; Szécsényi, À.; Hensen, E. J. M.; Ruiz-Martinez, J.; Pidko, E. A.; Gascon, J., Strategies for the Direct Catalytic Valorization of Methane Using Heterogeneous Catalysis: Challenges and Opportunities. *ACS Catalysis* **2016,** *6*, 2965-2981.

2. Amariglio, A.; Paréja, P.; Amariglio, H., Does C–C Bonding Proceed during Exposure of Adequate Metal Surfaces to CH_4? Reply to "Comment by Z. Hlavathy, Z. Paál, and P. Tétényi". *Journal of Catalysis* **1997,** *166*, 121-123.

3. Asami, K.; Fujita, T.; Kusakabe, K.-i.; Nishiyama, Y.; Ohtsuka, Y., Conversion of methane with carbon dioxide into C2 hydrocarbons over metal oxides. *Applied Catalysis A: General* **1995,** *126*, 245-255.

4. Tanaka, K.; Sekine, Y.; Oshima, K.; Tanaka, Y.; Matsukata, M.; Kikuchi, E., Catalytic Oxidative Coupling of Methane Assisted by Electric Power over a Semiconductor Catalyst. *Chemistry Letters* **2012,** *41*, 351-353.

5. Aika, K.-i.; Nishiyama, T., Utilisation of CO_2 in the oxidative coupling of methane over PbO–MgO and PbO–CaO. *Journal of the Chemical Society, Chemical Communications* **1988,** *1*, 70-71.

6. Istadi; Amin, N. A. S., Synergistic effect of catalyst basicity and reducibility on performance of ternary CeO_2-based catalyst for CO_2 OCM to C2 hydrocarbons. *Journal of Molecular Catalysis A: Chemical* **2006,** *259*, 61-66.

7. Larkin, D. W.; Caldwell, T. A.; Lobban, L. L.; Mallinson, R. G., Oxygen Pathways and Carbon Dioxide Utilization in Methane Partial Oxidation in Ambient Temperature Electric Discharges. *Energy & Fuels* **1998,** *12*, 740-744.

8. Zhang, X.; Dai, B.; Zhu, A.; Gong, W.; Liu, C., The simultaneous activation of methane and carbon dioxide to C2 hydrocarbons under pulse corona plasma over La_2O_3/γ-Al_2O_3 catalyst. *Catalysis Today* **2002,** *72*, 223-227.

9. Eliasson, B.; Liu, C.-j.; Kogelschatz, U., Direct Conversion of Methane and Carbon Dioxide to Higher Hydrocarbons Using Catalytic Dielectric-Barrier Discharges with Zeolites. *Industrial & Engineering Chemistry Research* **2000,** *39*, 1221-1227.

10. Oshima, K.; Tanaka, K.; Yabe, T.; Kikuchi, E.; Sekine, Y., Oxidative coupling of

methane using carbon dioxide in an electric field over La–ZrO_2 catalyst at low external temperature. *Fuel* **2013,** *107*, 879-881.

11. Oshima, K.; Shinagawa, T.; Sekine, Y., Methane Conversion Assisted by Plasma or Electric Field. *Journal of the Japan Petroleum Institute* **2013,** *56*, 11-21.

12. Yabe, T.; Kamite, Y.; Sugiura, K.; Ogo, S.; Sekine, Y., Low-temperature oxidative coupling of methane in an electric field using carbon dioxide over Ca-doped $LaAlO_3$ perovskite oxide catalysts. *Journal of CO_2 Utilization* **2017,** *20*, 156-162.

13. Manabe, R.; Okada, S.; Inagaki, R.; Oshima, K.; Ogo, S.; Sekine, Y., Surface Protonics Promotes Catalysis. *Sci. Rep.* **2016,** *6*, 38007.

14. Manabe, R.; Nakatsubo, H.; Gondo, A.; Murakami, K.; Ogo, S.; Tsuneki, H.; Ikeda, M.; Ishikawa, A.; Nakai, H.; Sekine, Y., Electrocatalytic synthesis of ammonia by surface proton hopping. *Chem. Sci.* **2017,** *8*, 5434-5439.

15. Gerceker, D.; Motagamwala, A. H.; Rivera-Dones, K. R.; Miller, J. B.; Huber, G. W.; Mavrikakis, M.; Dumesic, J. A., Methane Conversion to Ethylene and Aromatics on PtSn Catalysts. *ACS Catalysis* **2017,** *7*, 2088-2100.

16. Xiao, Y.; Varma, A., Highly Selective Nonoxidative Coupling of Methane over Pt-Bi Bimetallic Catalysts. *ACS Catalysis* **2018,** *8*, 2735-2740.

17. Zhu Chen, J.; Wu, Z.; Zhang, X.; Choi, S.; Xiao, Y.; Varma, A.; Liu, W.; Zhang, G.; Miller, J. T., Identification of the structure of the Bi promoted Pt non-oxidative coupling of methane catalyst: a nanoscale Pt_3Bi intermetallic alloy. *Catalysis Science & Technology* **2019,** *9*, 1349-1356.

18. Bajec, D.; Kostyniuk, A.; Pohar, A.; Likozar, B., Micro-kinetics of non-oxidative methane coupling to ethylene over Pt/CeO_2 catalyst. *Chemical Engineering Journal* **2020,** *396*.

19. Lin, B.; Zhang, Q.; Wang, Y., Catalytic Conversion of Ethylene to Propylene and Butenes over H−ZSM-5. *Industrial & Engineering Chemistry Research* **2009,** *48*, 10788-10795.

20. Follmann, S.; Ernst, S., Influence of the pore architecture on the selective conversion of ethene to propene and butenes over medium pore zeolites. *New Journal of Chemistry* **2016,** *40*, 4414-4419.

21. Nakaya, Y.; Furukawa, S., Catalysis of Alloys: Classification, Principles, and Design for a Variety of Materials and Reactions. *Chemical Reviews* **2022,** *in press*.

22. Furukawa, S.; Komatsu, T., Intermetallic Compounds: Promising Inorganic Materials for Well-Structured and Electronically Modified Reaction Environments for Efficient Catalysis. *ACS Catalysis* **2016,** *7*, 735-765.

23. Zhang, J.; Ma, R.; Ham, H.; Shimizu, K.-i.; Furukawa, S., Electroassisted Propane Dehydrogenation at Low Temperatures: Far beyond the Equilibrium Limitation. *JACS Au* **2021,** *1*, 1688-1693.

24. Murakami, K.; Manabe, R.; Nakatsubo, H.; Yabe, T.; Ogo, S.; Sekine, Y., Elucidation of the role of electric field on low temperature ammonia synthesis using isotopes. *Catalysis Today* **2018,** *303*, 271-275.

25. Choudhary, V. R.; Mulla, S. A. R.; Uphade, B. S., Oxidative coupling of methane over alkaline earth oxides deposited on commercial support precoated with rare earth oxides. *Fuel* **1999,** *78*, 427-437.

26. Lv, X.; Cai, S.; Chen, J.; Yan, D.; Jiang, M.; Chen, J.; Jia, H., Tuning the degradation activity and pathways of chlorinated organic pollutants over CeO_2 catalyst with acid sites: synergistic effect of Lewis and Brønsted acid sites. *Catalysis Science & Technology* **2021,** *11*, 4581-4595.

27. Schwach, P.; Pan, X.; Bao, X., Direct Conversion of Methane to Value-Added Chemicals over Heterogeneous Catalysts: Challenges and Prospects. *Chem. Rev.* **2017,** *117*, 8497-8520.

Chapter 5

Dry reforming of benzene as a model tar compound assisted with electric field

5. Dry Reforming of Benzene as a Model Tar Compound assisted with Electric Field

5.1 Introduction

Biomass is gaining more and more attention as a source of power, fuel, and other chemical products due to its renewability, compared with fossil fuel. When biomass is heated at temperatures above 500°C with a gasifying agent, the produced gas that contains a mixture of hydrogen, carbon monoxide, carbon dioxide, water, nitrogen, and other byproducts was transformed. It can be used to produce hydrocarbons, methanol, and various value-added chemicals, as well as directly used as power source in gas engines, turbines, furnaces et al.[1] However, large amounts of organic impurities, generally referred to as tars are also produced during biomass gasification which include a significant fraction of aromatics.[2] Therefore, it is very important to remove the problematic tars at the downstream of the gasifier. The various method can be physical or chemical. Especially, by using chemical method, the conversion of tars into syngas can increase the value of biomass utilization.[3] The chemical method to decompose tars include steam reforming, dry reforming, thermal cracking and water-gas shift reaction. Among them, dry reforming is a promising method to achieve complete elimination of tars and simultaneously utilization of carbon dioxide which is a greenhouse gas.[4] Benzene is selected as a model molecule in various tar components due to its thermal stability and relatively high weight percentage.[2] As shown in Equation (1), 1 mol of benzene can reduce 6 mol of carbon dioxide and produce carbon monoxide.

$$C_6H_6 + 6CO_2 \leftrightarrow 12CO + 3H_2 \quad \Delta H^0_{298} = 948 \text{ kJ mol}^{-1} \qquad (1)$$

Ni-based catalysts are widely used in dry reforming reactions due to its high C–H bond activation ability and relatively low price.[5, 6] However, due to its strong endothermicity, dry reforming of benzene (DRB) requires temperatures of higher than 700°C.[4] And under such severe temperature, Ni-based catalysts face critical drawbacks of carbon deposition and nickel sintering.[5] In this context, developing a novel catalytic system that can activate robust benzene molecules at low temperature is highly challenging but attractive. One of the possible and

pioneering approach is the electroassisted catalysis based on surface protonics methodology.[7-9] By imposing of an electric field to a catalyst, proton hopping via surface hydroxyl groups known as Grotthuss mechanism can be facilitated,[10] enabling strong proton collision with reactant molecules. Robust molecules, such as nitrogen, methane, carbon dioxide, can be activated by this methodology even at a low temperature region, resulting product yield far beyond the thermodynamic equilibrium limitation.[11, 12] This methodology is also valid for activation of benzene, but there is another problem: the complete dehydrogenation will lead to coke formation. Therefore, the delicate catalyst design is required to eliminate coke via CO_2 adsorption and activation.

In this chapter, we developed a novel catalytic system for electroassisted DRB. The CO yield was drastically improved by imposing direct current on catalyst bed. The alloying of Ni with Co and Ge synergistically promoted the consumption rate of benzene and CO_2. And by imposing 2.7 W of electric power, 28% of CO yield was achieved over $Ni_{1.5}Co_{1.5}Ge/CeO_2$ catalyst at a low external temperature (200°C) while the thermodynamic equilibrium yield is only 7.7%. Although this study remains under-research, the electroassisted DRB is a promising methodology for elimination of tar residues.

5.2 Experimental section

5.2.1 Catalysts preparation

Ni/CeO_2, $NiCo/CeO_2$, Ni_3Ge/CeO_2, and $Ni_{1.5}Co_{1.5}Ge/CeO_2$ catalysts (Ni: 3 wt%) were prepared by a conventional impregnation method using $Ni(NO_3)_2{\cdot}6H_2O$ (Kanto Chemical, 98.0%), $Co(NO_3)_2{\cdot}6H_2O$ (Fujifilm Wako, 98.0%) and $(NH_4)_2GeF_6$ (Furuya Metal Co. Ltd.) as metal precursors. The CeO_2 support (JRC–CEO–2, SBET= 123.1 m^2g^{-1}) was added to a vigorously stirred aqueous solution (50 mL H_2O per gram of CeO_2) containing Ni and the corresponding second and/or third metal precursor(s) (Ni:Co = 1:1, Ni:Ge = 3:1, Ni:Co:Ge = 1.5:1.5:1), followed by stirring for 3 h at room temperature. The mixture was dried under a reduced pressure at 50°C using a rotary evaporator, followed by calcination under flowing air at 500°C for 1 hour and reduction under flowing H_2 (50 mL min^{-1}) at 700°C for 2 hours.

5.2.2 Characterization

The XAFS spectra of the catalysts and reference compounds were recorded at the BL01B1 beamline in Spring-8, JASRI in fluorescence mode at room temperature. First, the catalyst was pressed into a pellet (diameter: 10 mm) and reduced under flowing H_2 at 700 °C for 0.5 h. Then, the reduced sample was then transferred into an Ar glove box (O_2: < 0.001 ppm) without exposing to air and sealed in a plastic bag (Barrier Nylon) with an ISO A500–HS oxygen absorber (Fe powder). The measurements for foil samples were done in air. The obtained XAFS spectra were analyzed using Athena software. The k^3-weighted EXAFS oscillation was Fourier-transformed in the k range of 3−12 $Å^{-1}$ for all samples.

5.2.3 Catalytic reaction

Thermal and electro-assisted DRB was carried out using a continuous flow fixed-bed quartz reactor with 6 mm internal diameter. The detailed setup of the reactor is shown in Figure 5.1. The catalyst was placed on a pies of glass wool in the quartz tube reactor. Two stainless steel rods (φ: 2mm) were inserted into the reactor as electrodes and contacted with the top and bottom of the catalyst bed. A K-type thermocouple covered with a glass capillary tube (for insulation protection) was also contacted with the catalyst bed to bed to measure the catalyst bed temperature separately from the furnace temperature. Benzene (FUJIFILM Wako Pure Chemical Corp., Super Dehydrated) was injected using a syringe pump (IC3100, KD Scientific

Inc.) into a gas mixer and carried by Ar (Ar-1: 10 mL·min^{-1}) into the reactor. The gas lines from gas mixer to outlet of experimental section were heated up to 100°C by wrapped heating ribbon to inhibit the condensation of benzene.

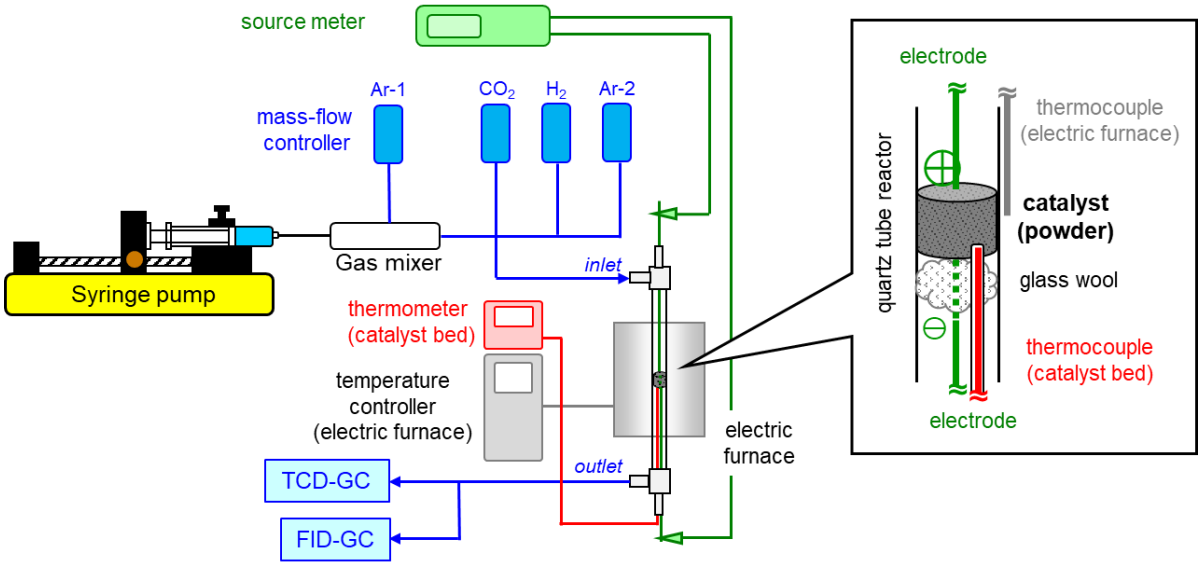

Figure 5.1. The detailed setup of the reactor for electroassisted DRB. The thermocouple for the catalyst bed was covered with a capillary glass tube for insulation protection. Thermal PDH was also performed using this reactor without imposing direct current.

Prior to the catalytic reaction, the catalyst was pretreated under flowing H_2/Ar (10/10 mL·min^{-1}) at 700°C for 0.5 h, followed by purging under flowing Ar (10 mL·min^{-1}) at the reaction temperature. A constant direct current (5–30 mA) was imposed to the catalyst bed using a high voltage DC power supply (Tektronix Keithley SMU 2657A). Activity tests were conducted under a reaction gas flow (CO_2: 13.7 10 mL·min^{-1} and Ar-2: 10 mL·min^{-1}) and 0.5 mL·h^{-1} of liquid benzene carried by 10 mL·min^{-1} of Ar. The temperature of electric furnace was set as 200°C for electroassisted DRB. A thermal conductivity detection gas chromatograph (Shimadzu GC-8A, column: ShinCarbon) was used to analyze CO_2, CO, and H_2. And a flame ionization detector gas chromatograph (Shimadzu GC-2014s, column: Porapak-Q).

The conversions of C_6H_6 and CO_2, selectivity of CO, yield of CO, consumption rates of CO_2 and benzene per electric power, and carbon balance were defined as follows:

$$\text{C}_6\text{H}_6 \text{ conversion: } X_{\text{C}_6\text{H}_6}\,(\%) = \frac{[\text{C}_6\text{H}_6]_{\text{in}} - [\text{C}_6\text{H}_6]_{\text{out}}}{[\text{C}_6\text{H}_6]_{\text{in}}} \times 100$$

$$\text{CO}_2 \text{ conversion: } \text{X}_{\text{CO}_2}\,(\%) = \frac{[\text{CO}_2]_{\text{in}} - [\text{CO}_2]_{\text{out}}}{[\text{CO}_2]_{\text{in}}} \times 100$$

$$\text{CO selectivity: } \text{S}_{\text{CO}}\,(\%) = \frac{[\text{CO}]_{\text{out}} \times 100 - ([\text{CO}_2]_{\text{in}} - [\text{CO}_2]_{\text{out}})}{6 \times ([\text{C}_6\text{H}_6]_{\text{in}} - [\text{C}_6\text{H}_6]_{\text{out}}) + ([\text{CO}_2]_{\text{in}} - [\text{CO}_2]_{\text{out}})}$$

$$\text{CO yield: } \text{Y}_{\text{CO}}\,(\%) = \frac{\text{X}_{\text{C}_6\text{H}_6} \cdot \text{S}_{\text{CO}}}{100}$$

$$\text{Consumption rate of } \text{C}_6\text{H}_6 \text{ per electric power: } \text{R}_{\text{C}_6\text{H}_6} = \frac{[\text{C}_6\text{H}_6]_{\text{in}} - [\text{C}_6\text{H}_6]_{\text{out}}}{\text{E}_{\text{p}}}$$

$$\text{Consumption rate of } \text{CO}_2 \text{ per electric power: } \text{R}_{\text{C}_6\text{H}_6} = \frac{[\text{CO}_2]_{\text{in}} - [\text{CO}_2]_{\text{out}}}{\text{E}_{\text{p}}}$$

$$\text{Carbon balance: } C_b(\%) = \frac{6 \times [\text{C}_6\text{H}_6]_{\text{out}} + [\text{CO}_2]_{\text{out}} + [\text{CO}]_{\text{out}}}{6 \times [\text{C}_6\text{H}_6]_{\text{in}} + [\text{CO}_2]_{\text{in}}}$$

5.3 Results and discussions

5.3.1 Structure characterization

The catalysts were prepared by a conventional impregnation method using CeO_2 as a catalyst support capable of surface protonics (Ni: 3wt % for all catalysts). The XAFS analysis was performed to obtain structural information of Ni-based catalysts. The X-ray absorption near-edge structure (XANES) spectra (Figure 5.2a & Figure 5.3a, b) showed that the Ni, Co and Ge were in a metallic state. The absence of oxidative peak in Fourier-transforms of EXAFS spectra (Figure 5.4) of Ni, Co, and Ge also proved it. The Ni K-edge extended X-ray absorption fine structure (EXAFS) spectra revealed that the Ni_3Ge and $Ni_{1.5}Co_{1.5}Ge$ is randomly alloyed rather than formation of intermetallic structure due to their similar oscillations with Ni foil.

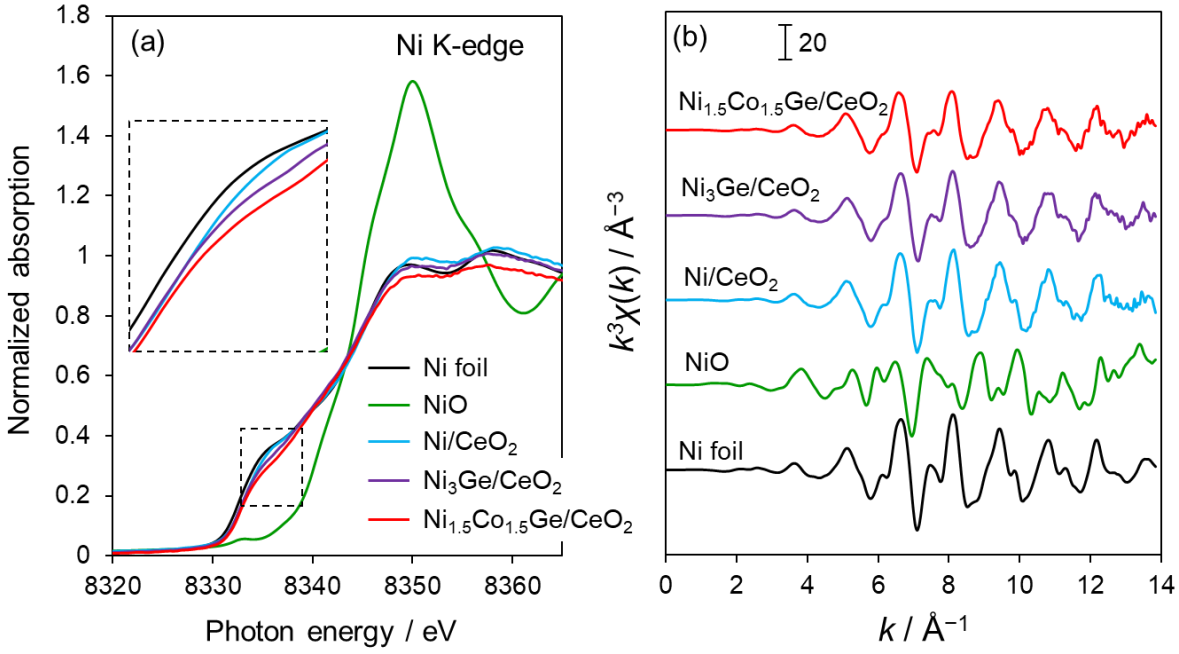

Figure 5.2. (a) Ni K-edge X-ray absorption near edge structure (XANES) spectra of Ni and Ni-based alloys loaded on CeO_2 catalysts and reference compounds. (b) Ni K-edge extended X-ray absorption fine structure (EXAFS) spectra of the Ni and Ni-based alloys loaded on CeO_2 catalysts and reference compounds.

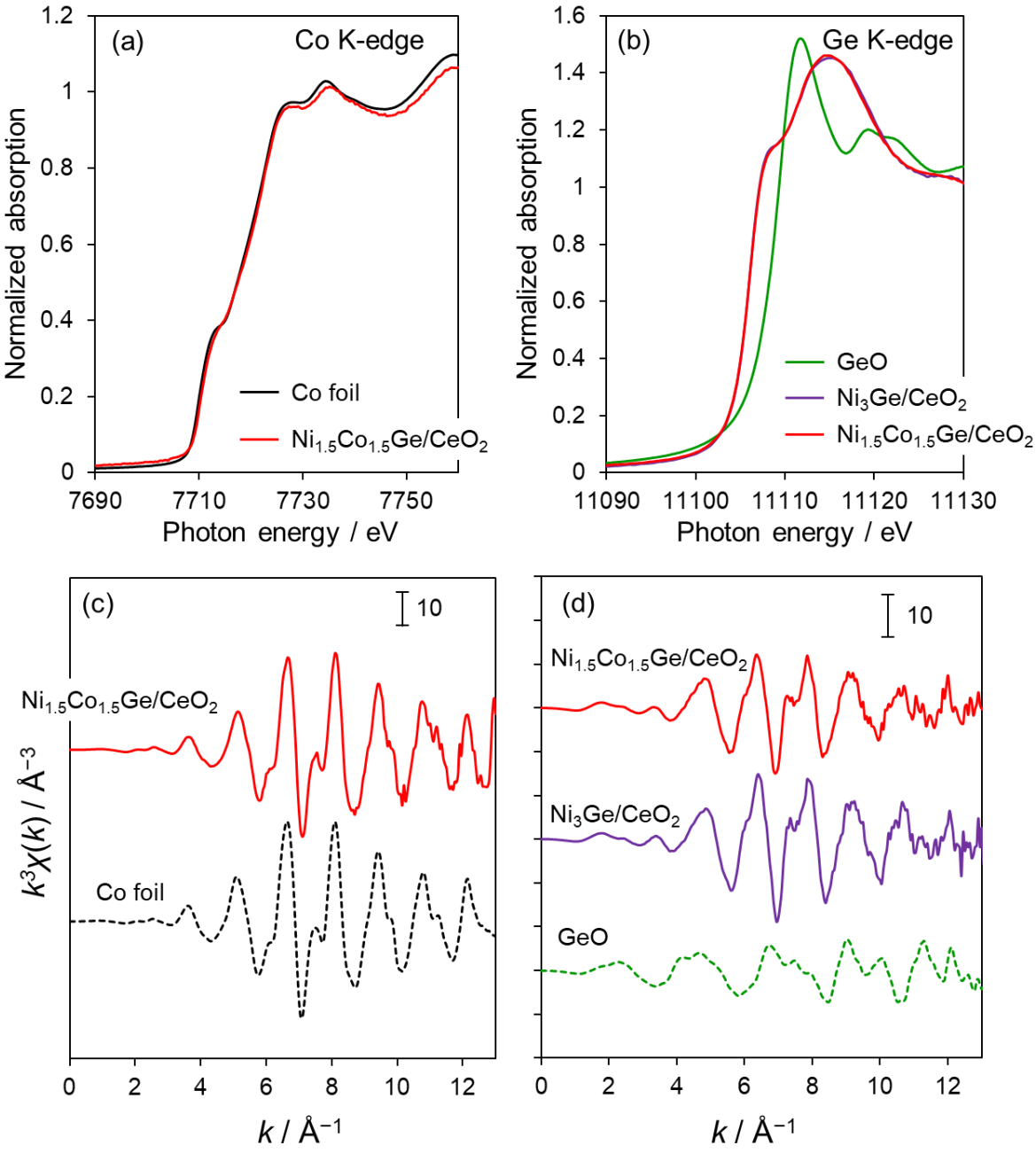

Figure 5.3. (a) Co, (b) Ge K-edge X-ray absorption near edge structure (XANES) spectra of $Ni_{1.5}Co_{1.5}Ge/CeO_2$ and Ni_3Ge/CeO_2 catalysts and reference compounds. (c) Co, (d) Ge K-edge extended X-ray absorption fine structure (EXAFS) spectra of $Ni_{1.5}Co_{1.5}Ge/CeO_2$ and Ni_3Ge/CeO_2 catalysts and reference compounds.

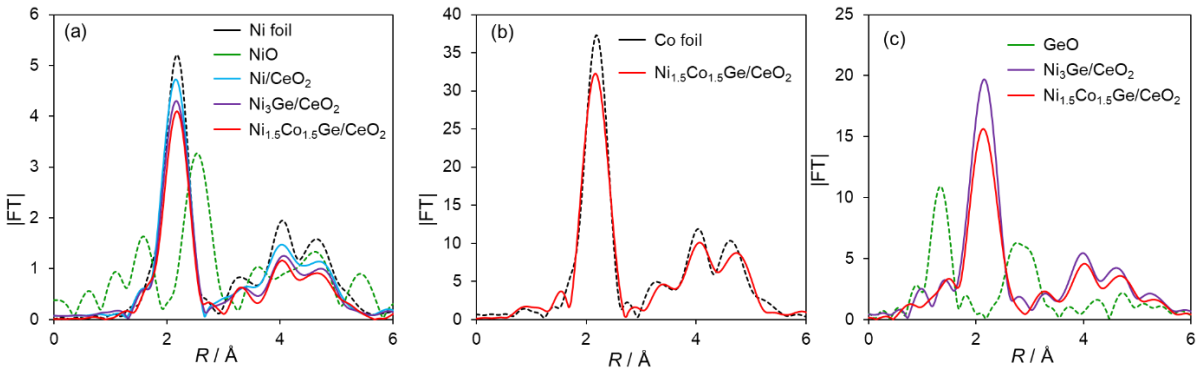

Figure 5.4. Fourier-transforms of EXAFS in (a) Ni, (b) Co and (c) Ge K-edge of Ni and Ni-based alloys loaded on CeO_2 catalysts and reference compounds.

5.3.2 Electroassited catalytic DRB performance

Next, we tested the electroassisted catalytic DRB performance of $Ni_{1.5}Co_{1.5}Ge/CeO_2$ catalyst using a fixed-bed continuous flow reactor and compared it with the control catalysts (Ni/CeO_2, $NiCo/CeO_2$, and Ni_3Ge/CeO_2). As shown in Figure 5.1, two stainless steel rods as electrodes were placed in contact with the top and bottom of the catalyst bed to impose a direct current to the catalyst. Before the reaction, the catalyst was pretreated with flowing H_2 at 700°C, so that the nanoparticles and CeO_2 were reduced which is necessary to pass an electric current to the catalyst bed. Figure 5.5 represents the dependence of the CO yield on the electric power supplied to the system. The propylene yield increased monotonously with an increase in the supplied power, showing that electric field significantly boosted the reaction (carbon balances were 0.8–1.0; Figure 5.6a). Furthermore, the CO yield over $Ni_{1.5}Co_{1.5}Ge/CeO_2$ catalyst was remarkably higher than other catalysts, while the catalyst bed temperatures did not show significant difference among these catalysts (Figure 5.7b). It indicates that alloying of Ni with Co and Ge significantly improved that electroassisted DRB catalytic performance.

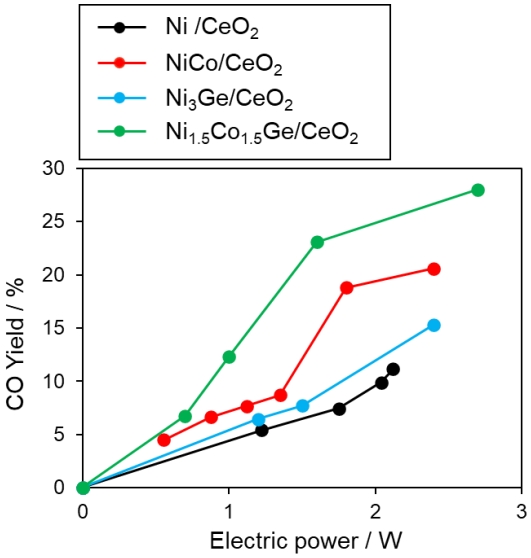

Figure 5.5. Dependence of CO yield on the electric power supplied to the catalytic system. The furnace was set to 200°C. Benzene and carbon dioxide were introduced into the reactor with Ar in stoichiometric ratio (CO_2/C_6H_6 = 6, according to Equation (1)). Input current: 3–30 mA; catalyst weight: 100.0 mg.

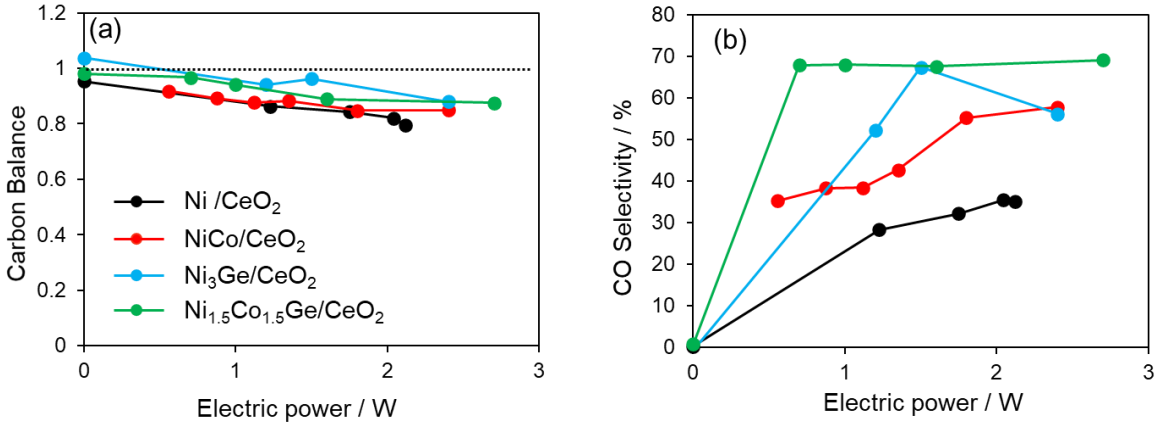

Figure 5.6. (a) Carbon balances and (b) CO selectivity for the electroassisted DRB. Each data point corresponding to that in Figure 5.5.

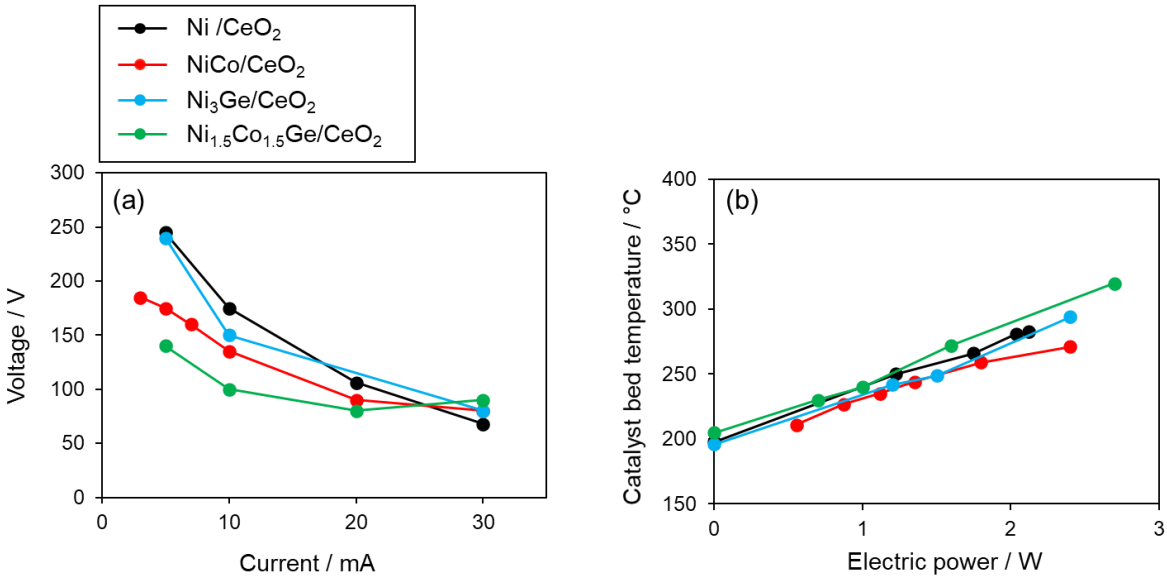

Figure 5.7. The relationship between (a) current and voltage; (b) electric power and catalyst bed temperature over Ni and Ni-based alloy catalysts at 200℃ of furnace temperature.

As a universal scale for catalytic activity in the electroassisted system, we applied consumption rate of benzene and CO_2 per electric power to the system, as shown in Figure 5.8b. Under the similar external conditions (electric power and catalyst bed temperature in Figure 5.8a), the $NiCo/CeO_2$ catalyst showed much higher consumption rates of benzene and CO_2 than Ni/CeO_2. However, the alloying of Ge showed less improvement of consumption rates for Ni/CeO_2 catalyst. Furthermore, the highest consumption rates of benzene and CO_2 were achieved over $Ni_{1.5}Co_{1.5}Ge/CeO_2$ catalyst. Therefore, the synergistic effect of Co and Ge played essential role in the electroassisted DRB catalytic system. Finally, CO yield of 28% was achieved over $Ni_{1.5}Co_{1.5}Ge/CeO_2$ catalyst by implying 2.7 W of electric power at 320℃, far beyond the thermodynamic equilibrium CO yield at the same temperature (7.7%; Figure 5.9).

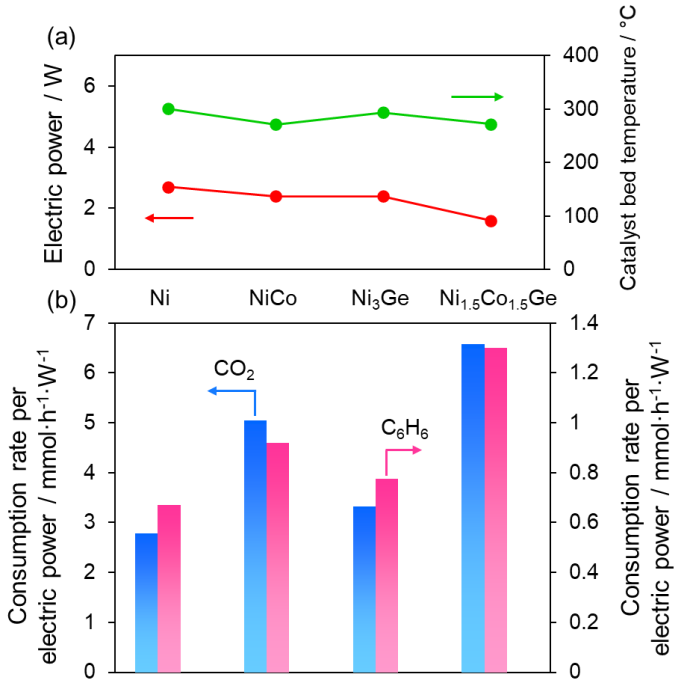

Figure 5.8. (a) Electric powers and catalyst bed temperatures; (b) consumption rates of benzene (blue bar) and CO_2 (red bar) per electric power over Ni and Ni-based alloy catalysts.

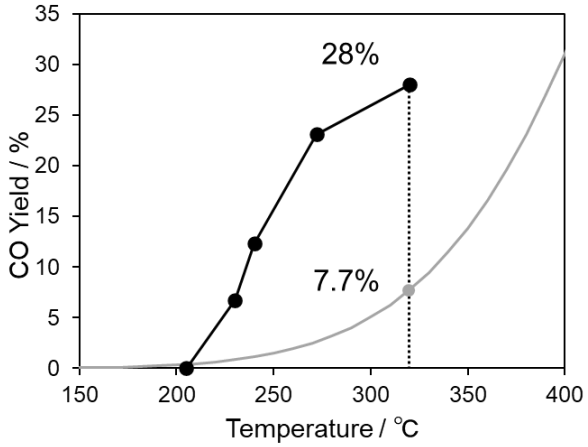

Figure 5.9. The CO yield over $Ni_{1.5}Co_{1.5}Ge/CeO_2$ catalyst under electric field and the thermodynamic equilibrium CO yield.

Up to now, this study is still under-research. The next research will mainly focus on the reaction mechanism under electric field. Various characterizations are necessary to explain the role of Co and Ge in the reaction mechanism.

5.4 Conclusion

In summary, a novel type of catalytic system was developed for elimination of tars at low temperatures. Over $Ni_{1.5}Co_{1.5}Ge/CeO_2$ catalyst, dry reforming of benzene was drastically facilitated by electric field. With the aid of 2.7 W of electric power, 28% of CO yield was achieved at a low external temperature (200°C) while the thermodynamic equilibrium yield is only 7.7%. Alloying of Ni with Co and Ge synergistically promoted the consumption of benzene and CO_2. Overall, this work shows a promising methodology for low temperature conversion of tars.

References

1. Gusta, E.; Dalai, A. K.; Uddin, M. A.; Sasaoka, E., Catalytic Decomposition of Biomass Tars with Dolomites. *Energy & Fuels* **2009,** *23*, 2264-2272.

2. Coll, R.; Salvadó, J.; Farriol, X.; Montané, D., Steam reforming model compounds of biomass gasification tars: conversion at different operating conditions and tendency towards coke formation. *Fuel Processing Technology* **2001,** *74*, 19-31.

3. Torres, W.; Pansare, S. S.; Goodwin, J. G., Hot Gas Removal of Tars, Ammonia, and Hydrogen Sulfide from Biomass Gasification Gas. *Catalysis Reviews* **2007,** *49*, 407-456.

4. Simell, P. A.; Hakala, N. A. K.; Haario, H. E.; Krause, A. O. I., Catalytic Decomposition of Gasification Gas Tar with Benzene as the Model Compound. *Industrial & Engineering Chemistry Research* **1997,** *36*, 42-51.

5. Aziz, M. A. A.; Jalil, A. A.; Wongsakulphasatch, S.; Vo, D. V. N., Understanding the role of surface basic sites of catalysts in CO_2 activation in dry reforming of methane: a short review. *Catalysis Science & Technology* **2020,** *10*, 35-45.

6. Wu, J.; Gao, J.; Lian, S.; Li, J.; Sun, K.; Zhao, S.; Kim, Y. D.; Ren, Y.; Zhang, M.; Liu, Q.; Liu, Z.; Peng, Z., Engineering the Oxygen Vacancies Enables Ni single-atom Catalyst For Stable and Efficient C-H Activation. *Applied Catalysis B: Environmental* **2022**, 121516.

7. Manabe, R.; Okada, S.; Inagaki, R.; Oshima, K.; Ogo, S.; Sekine, Y., Surface Protonics Promotes Catalysis. *Sci. Rep.* **2016,** *6*, 38007.

8. Manabe, R.; Nakatsubo, H.; Gondo, A.; Murakami, K.; Ogo, S.; Tsuneki, H.; Ikeda, M.; Ishikawa, A.; Nakai, H.; Sekine, Y., Electrocatalytic synthesis of ammonia by surface proton hopping. *Chem. Sci.* **2017,** *8*, 5434-5439.

9. Zhang, J.; Ma, R.; Ham, H.; Shimizu, K.-i.; Furukawa, S., Electroassisted Propane Dehydrogenation at Low Temperatures: Far beyond the Equilibrium Limitation. *JACS Au* **2021,** *1*, 1688-1693.

10. Agmon, N., The grotthuss mechanism. *Chemical Physics Letters* **1995,** *244*, 456-462.

11. Yabe, T.; Kamite, Y.; Sugiura, K.; Ogo, S.; Sekine, Y., Low-temperature oxidative coupling of methane in an electric field using carbon dioxide over Ca-doped $LaAlO_3$ perovskite

oxide catalysts. *Journal of CO_2 Utilization* **2017,** *20*, 156-162.

12. Sekine, Y.; Manabe, R., Reaction mechanism of low-temperature catalysis by surface protonics in an electric field. *Faraday Discuss.* **2021,** *229*, 341-358.

Chapter 6

General Conclusions

6. General conclusions

In this research, I focused on electroassisted catalytic system based on surface protonics for low-temperature conversion of robust reactant molecules. Imposing of direct current on catalyst bed remarkably increased the product yield in various reactions, such as propane dehydrogenation, oxidative coupling of methane using carbon dioxide, and dry reforming of benzene. Besides, the modification of surface protonics methodology and active sites was performed to promote the electroassisted catalytic performance. The present study provides a novel catalytic system for low-temperature reactions.

Chapter 2 concludes that a novel type of catalytic system was developed for PDH by a combination of a surface protonics methodology and active site modification based on intermetallics. With the aid of 3.2 W electric power, Pt–In/TiO_2 afforded a 10.2% propylene yield at 250°C for the first time, where the thermodynamic equilibrium yield was only 0.15%. Alloying of Pt with In drastically modified the electronic state of Pt, which enhanced both the catalytic activity and selectivity. Overall, this study opens a new horizon for the catalysis of PDH.

Chapter 3 concludes that Sm cations were doped into the surface Ti sites of TiO_2 using anatase TiO_2 as a core and Ti–Sm sol as a shell, which increased the density of surface protons (hydroxyl groups) by charge compensation. Nanoparticulate Pt–In with intermetallic Pt_3In phase was supported on the Sm-doped TiO_2 (Pt–In/Sm–TiO_2), which acted as a highly efficient catalyst for electroassisted PDH at 300°C. The catalytic activity in electroassisted PDH can be controlled by changing the surface hydroxyl density depending on the doping amount of Sm, where 1-mol% is the optimum doping amount. A propylene yield of 19.3% was obtained when an electric power of 5.35 W was applied, which is far beyond the thermodynamic equilibrium limitation. Although Sm doping of TiO_2 itself does not influence the reaction mechanism of electroassisted PDH based on surface protonics, it can drastically increase the overall reaction rate of propylene formation by promoting proton collisions on propane. This promotion is achieved not only by surface proton enrichment but also by the enhancement of propane adsorption by Sm. Thus, the results obtained in this study provide a highly efficient catalytic

system for low-temperature alkane conversions and a general catalyst design concept for enhancing electroassisted catalysis based on surface protonics.

Chapter 4 concludes that the effective production of C2 and C3 hydrocarbons was achieved by electroassisted CO_2–OCM. With the aid of 2.73 W electric power, Pt_3Sn/CeO_2 catalyst afforded a 4.06% C2 hydrocarbons yield and 0.34% C3 hydrocarbons yield even at low external temperature of 300°C. With CeO_2 as support, electric field and Pt-based bimetallic alloy showed synergistic effect, which effectively enhanced both the catalytic activity and selectivity.

Chapter 5 concludes that a novel type of catalytic system was developed for elimination of tars at low temperatures. Over $Ni_{1.5}Co_{1.5}Ge/CeO_2$ catalyst, dry reforming of benzene was drastically facilitated by electric field. With the aid of 2.7 W of electric power, 28% of CO yield was achieved at a low external temperature (200°C) while the thermodynamic equilibrium yield is only 7.7%. Alloying of Ni with Co and Ge synergistically promoted the consumption of benzene and CO_2. Overall, this work shows a promising methodology for low temperature conversion of tars.

In summary, the imposed direct current on catalyst bed facilitates activation of robust reactant molecules based on surface protonics methodology. I designed appropriate catalysts to maximize the performance of surface protonics, which can be divided into two methods: (a) increasing the total amount of surface protons by doping trivalent cation such as Sm^{3+} into TiO_2 surface due to charge compensation; (b) facilitating the proton collision process by modification of active sites. Finally, we can drastically enhance the electroassisted catalysis of surface protonics by combining these two promotional effects.

Acknowledgement

Time flies, it's been about three years since I was accepted as a doctoral candidate in Graduate school of Chemical Science and Engineering (CSE), Hokkaido University. In three years, I have received countless help from professors, friends, and my family. Especially when I first came to Japan, many of my friends came forward to help me with various procedures.

Firstly, I am very appreciative of my supervisor Professor Shinya Furukawa. He taught me both the basic knowledge and the results analysis. I learnt so much from Prof. Furukawa, not only about academic knowledge, but also precise scientific attitude. I would like to express my gratitude to Professor Furukawa. I would also like to thank all members in our group: Ke, Feilong, Ham-san, Jiamin, Nakaya, Hayashida…I would never forget the good memories and friendships with everyone.

I would also like express my appreciation to Professor Ken-ichi Shimizu, Professor Takashi Toyao for their invaluable suggestions and advice. I also thank staffs in our laboratory, thanks for your help and caring.

The last but not least, I would like to thank my family. They offered me full support and solicitude. Thank you!

Zhang Jianshuo

张 建烁